Editors' Suggestion

Taming nonequilibrium thermal fluctuations in subthreshold CMOS circuits

Nahuel Freitas,[*,†] Geremia Massarelli, Jeremy Rothschild, Dylan Keane, Ethan Dawe, Sewook Hwang, Akhil Garlapati,[†] and Trevor McCourt[†,‡]
Extropic Corporation, Cambridge, Massachusetts, USA

(Received 4 July 2025; revised 16 January 2026; accepted 12 February 2026; published 18 March 2026)

As CMOS technology scales down, thermal fluctuations increasingly impact circuit behavior, posing challenges to conventional circuit design. However, the inherent stochasticity introduced by thermal noise is now being explored as a potential resource in the emerging field of probabilistic computing. This work presents a fully CMOS experimental platform that enables direct control over its intrinsic thermal fluctuations. These devices function as programmable multivariate Gaussian samplers, offering a hardware primitive for energy-efficient stochastic computing and serving as an experimental platform for studies in electronic noise and stochastic thermodynamics.

DOI: 10.1103/5l2z-3f1h

The aggressive miniaturization of CMOS technology is a double-edged sword; as a transistor circuit is scaled down in size, it becomes faster and more energy-efficient [1], but it also becomes noisier [2]. As device dimensions and supply voltages continue to be pushed to their thermodynamic limits, the noise that is intrinsic to transistors will begin to upset traditional deterministic computer architectures [3,4].

Recent proposals suggest that this apparent roadblock imposed by noise may be circumvented by building intentionally stochastic *probabilistic circuits* (p circuits) into a computing system [5–11]. P circuits harness the noise present in all devices to generate samples from computationally useful probability distributions.

Compared to purely deterministic approaches, probabilistic computer architectures can be more energy efficient when running specific algorithms that rely heavily on random sampling. Random sampling is expensive on a deterministic computer: one must employ complex circuitry involving thousands of transistors that generate pseudorandom numbers [12]. These large circuits consume similar amounts of energy to those implementing computationally richer operations, such as addition.

For a p circuit to be practically useful in computing, it must be predictable, programmable, and performant. Predictability means that the stochastic dynamics of the p circuit obey some simple physical model that can be used to engineer it. A p circuit is programmable if the distribution it samples from can be tuned at runtime. The performance of a p circuit is measured by its correlation time, energy consumption, and physical size, which jointly quantify the space-time-energy cost of using the circuit for random sampling.

Current implementations of p circuits fall short in at least one of these key areas. P circuits built using magnetic tunnel junctions are a promising long-term direction as they obey well-characterized stochastic dynamics [13] and are straightforwardly programmed [14–16]. While these devices are, in principle, compatible with CMOS processes [17], work on integration is still underway [18,19], which limits near-term performance [20,21]. To avoid these integration issues, practitioners have also considered p-circuit architectures involving only transistors [22,23]. However, current approaches generally rely on extremely sensitive phenomena, such as the randomness of bistable latches at power up [24,25], or are based on crude treatments of noise [22], making programmability and prediction difficult.

Circuits of transistors operating in the deep subthreshold regime are a natural candidate for building practical p circuits. Charge transport in these circuits is predominately thermally activated, leading to shot-noise dynamics [26]. Recently, shot-noise models have been generalized from the single-transistor level to networks of transistors via a technique based on Markov jump processes (MJPs) [27], suggesting that the stochastic dynamics of subthreshold circuits may be rigorously predicted. Subthreshold networks are also straightforwardly programmable via control

[*]Contact author: nfreitas@extropic.ai
[†]These authors contributed equally to this work.
[‡]Contact author: trevor@extropic.ai

voltages. Additionally, small transistors leak more current, increasing the performance of subthreshold circuits [28].

This paper experimentally demonstrates that practical p circuits can be built using subthreshold transistors. Specifically, we introduce and characterize a family of circuits that sample from voltage-programmable multivariate Gaussian distributions. These circuits enable the control of correlations between multiple degrees of freedom and represent a powerful primitive that can be used either as a standalone p circuit or as part of a larger circuit performing a non-Gaussian sampling operation (p bits being the most direct and prominent example [11]). Our work paves the way for near-term, large-scale computers that leverage p circuits; we have already applied the principles outlined here in designing a probabilistic computing system that runs diffusionlike models [29].

In addition to the potential of our work for probabilistic computing, it also substantially advances our physical understanding of shot noise in subthreshold transistors by validating the MJP model presented in Ref. [27]. While a large body of work studies shot noise at the single-transistor level [26,30,31], studies of noise physics in larger circuits are limited and often application-specific [32]. Our work tests a simple and generic noise model for subthreshold transistor networks against experimental data, allowing the model to be confidently used in future engineering pursuits.

The remainder of this paper will detail our Gaussian sampling circuits, which we refer to as nonequilibrium, adjustable temperature resistor networks (NEAT-RNs). We will first introduce NEAT-RNs and explain (as suggested by their name) how voltage controls can be used to program their steady-state voltage distribution. Then, we will demonstrate that the MJP model of Ref. [27] accurately predicts experimental measurements of the behavior of a simple 2D NEAT-RN. Next, we will demonstrate that the programmability of NEAT-RNs can be significantly enhanced by introducing additional degrees of freedom that mediate interaction. Finally, we will discuss the speed and energy efficiency of NEAT-RNs and demonstrate that they are sufficiently performant to be useful as part of a modern probabilistic computing system.

NEAT-RNs are composed of multiple CMOS inverters with independent gate control, where mutual capacitances couple the outputs of different inverters. The simplest nontrivial example in the family is shown in Fig. 1(a). The experiments discussed in the following involve the measurement of the statistical properties of the signals $v = (v_1, v_2)$ for different operating voltages [see Fig. 1(c) for examples of time series]. Most of the variability in those signals is explained by two sources of noise: (i) thermal fluctuations associated to the transport of charge through individual transistors, and (ii) low-frequency fluctuations in the overall conductivity of each transistor. While the first contribution is of fundamental nature, as it has a purely thermodynamic origin [26,27], the second one is usually understood to arise due to material defects that act as fluctuating charge traps [33–37]. The obtained data is compared to an analytical model that is able to incorporate both sources of noise. However, in what follows we restrict the discussion to the analytical description of the thermal fluctuations only, which are anyway the dominant ones as they contribute around 70% of the total signal power in the frequency range given by the measurement duration and sampling rate (see Appendix D).

After linearization around an operating point, NEAT-RNs become equivalent to a noisy RC network [38–40], where the effective conductance and temperature of each resistor can be controlled at will [see Fig. 1(b)]. When the effective temperatures are equal, the system attains an equilibrium steady-state probability distribution $P(v)$ that is entirely determined by the capacitances, which cannot be controlled in nanoscopic circuits. However, if the effective temperatures differ, the system attains a nonequilibrium steady-state distribution that becomes dependent on the effective temperatures and conductances. In this way, the steady-state distribution can be controlled by manipulating the voltages V^i_{dd}, and $V^i_{n/p}$ [see Figs. 1(f) and 1(g)].

Specifically, combining the MJP formalism of Ref. [27] with the Enz-Krummenacher-Vittoz (EKV) model for subthreshold transistors [41], the steady-state fluctuations of a NEAT-RN can be found to be approximately Gaussian,

$$P(v) \propto \exp -\frac{1}{2}\left(v - v^*\right)^T \Sigma^{-1}\left(v - v^*\right). \tag{1}$$

Here, v is a vector of voltages for each node in the circuit, v^* is the dc level of each voltage, and Σ is the steady-state covariance matrix. Σ is given by the solution to the Lyapunov equation,

$$G\,\Sigma\,C + C\,\Sigma\,G = 2k_b\,G^{1/2}\,\mathcal{T}\,G^{1/2}, \tag{2}$$

where G is a diagonal matrix of effective linear conductances associated with each inverter, $\mathcal{T}$ is a diagonal matrix of effective temperatures, and C is the circuit's Maxwell capacitance matrix. The matrix elements of $\mathcal{T}$ and G can be written explicitly in terms of the circuit's control voltages; see Appendixes B and C.

In the limit that each inverter is balanced such that $v^*_i = V^i_{\mathrm{dd}}/2$ and the subthreshold slope parameter of each transistor approaches 1 (see Appendix C), the expressions for the matrix elements of G and $\mathcal{T}$ take an intuitive form,

$$G_{ii} = 2\frac{I^p_0}{V_T}\exp\left(\left(V^i_{\mathrm{dd}}/2 - V^i_p\right)/V_T\right), \tag{3}$$

$$\mathcal{T}_{ii} = T\frac{1+\exp\left(V^i_{\mathrm{dd}}/2V_T\right)}{2}. \tag{4}$$

Here, I^p_0 is the EKV model current parameter for each transistor. T is the physical temperature of the system

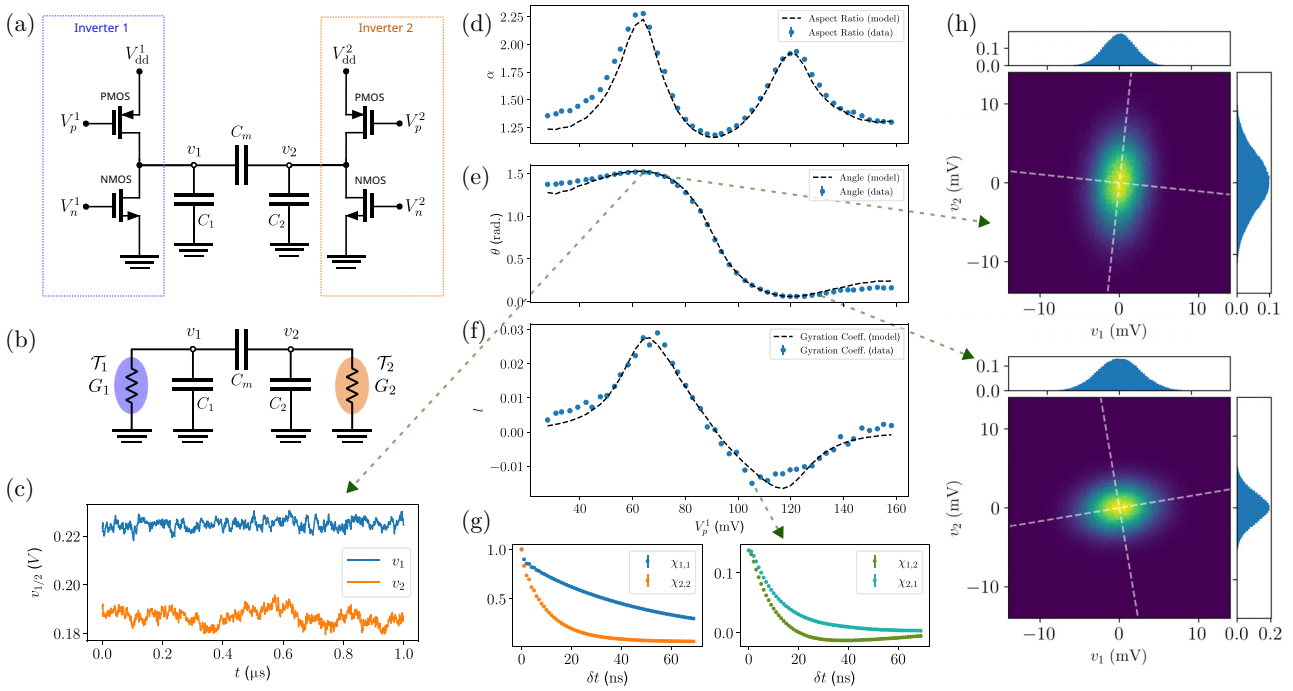

FIG. 1. Predictable and programmable Gaussian sampling with a NEAT-RN. (a) A simple NEAT-RN: two independently controlled, capacitively coupled CMOS inverters. (b) The fluctuations around the dc operating point of a NEAT-RN are equivalent to those of a linear *RC* circuit with controllable effective conductances and temperatures. (c) Snapshot of the measured time series of voltages v_1 and v_2, for the operating point indicated by the arrow. For different points along the voltage sweep mentioned in the text. (d) Aspect ratio of the covariance matrix of signals v_1 and v_2, (e) angle of the main principal component of the same matrix, and (f) normalized gyration coefficient l (integration time $t_I = 200$ ns). (g) Example of the delayed autocorrelation (left) and cross-correlation (right) functions. (h) Example centered histograms of the signals v_1 and v_2 for two operating points. Dashed lines indicate the principal axes. In all cases we fixed the powering voltages $V^1_{\rm dd} = 137 \pm 1$ mV, $V^2_{\rm dd} = 142 \pm 1$ mV and NMOS gate voltages $V^1_n = V^2_n = 76 \pm 1$ mV, while PMOS gate voltages satisfy $V^1_p + V^2_p = 200 \pm 1$ mV.

and $V_T = k_b T/q_e$ the associated thermal voltage (q_e is the electron charge). We chose to eliminate the control voltage V^i_n from this expression using the balance constraint. This decision was arbitrary, and the expressions could be written just as easily with V^i_p eliminated.

This limiting case makes it clear that NEAT-RNs are highly programmable; the effective conductance of each branch can be set by varying the gate control voltage with respect to $V_{\rm dd}$, and the effective temperature can be elevated with respect to the actual ambient temperature by increasing $V^i_{\rm dd}$ above ground. The potential values that G_{ii} and $\mathcal{T}_{ii}$ can take are limited by the onset of moderate inversion, at which point the shot-noise modeling assumption used to derive Eq. (2) becomes invalid. As long as the devices are in subthreshold, $\mathcal{T}$ and G can be independently controlled to program the p circuit with a wide range of covariance matrices.

To empirically establish the predictability and programmability of our p circuit, we fabricated the circuit shown in Fig. 1(a) using an advanced TSMC FinFET [42–44] process and fit Eq. (2) to its steady-state voltage distribution. Specifically, we fixed all voltages except for the PMOS control voltages, which were swept such that $V^1_p + V^2_p = 200 \pm 1$ mV. Voltage time series were measured at each operating point, from which a covariance matrix was estimated (the specifics of the fitting procedure are outlined in Appendix E).

We characterized the measured covariance matrix via its spectrum. Specifically, we computed the eigenvalues λ_k and eigenvectors q_k, satisfying $\Sigma q_k = \lambda_k q_k$ with $\lambda_0 \geq \lambda_1$. From the eigenvalues and eigenvectors of Σ, we define the aspect ratio of the eigenvalues α and the angle of the principal component θ,

$$\alpha \equiv \sqrt{\lambda_0/\lambda_1}, \qquad \theta \equiv \arctan((q_0)_1/(q_0)_2). \tag{5}$$

Examples of the observed steady-state distribution are shown in Figs. 1(f) and 1(g).

Figures 1(c) and 1(d) compare the observed dependence of α and θ on V^1_p to the best fit of Eq. (2). These results indicate that the fluctuations in the signals v_1 and v_2 can be reliably controlled by changing the operating voltages $V^{1/2}_{n/p}$. Additionally, we observe that the simple modeling based on Eq. (2) effectively captures the main features of the data. Thus, the produced signals are both controllable and predictable.

To establish that the MJP model can predict the dynamic properties of a NEAT-RN, not just the steady-state distribution, we measure the circulation of the voltage state and compare it to the prediction of the model. This circulation can be quantified via the coefficient $L(\delta t) \equiv \langle v \times \delta v \rangle$, where $\delta v = v(t+\delta t) - v(t)$ is the displacement in time δt. At steady-state conditions, it is possible to rewrite L as

$$L(\delta t) = \mathbb{X}_{1,2}(\delta t) - \mathbb{X}_{2,1}(\delta t), \tag{6}$$

where $\mathbb{X}_{j,k}(\delta t) \equiv \langle v_j(t) v_k(t+\delta t) \rangle - \langle v_j(t) \rangle \langle v_k(t+\delta t) \rangle$ is a delayed correlation, which can be obtained from time series. The previous expression is known as the cross-correlation asymmetry and is a measure of time-reversal symmetry breaking [45–47]. For example, in Fig. 1(g) we show the normalized delayed correlations $\chi_{j,k} \equiv \mathbb{X}_{j,k}/\sqrt{\mathrm{var}(v_j)\mathrm{var}(v_k)}$ for a particular operating point. We observe that the delayed correlations are indeed asymmetric, indicating a breakdown of time-reversal invariance due to the nonequilibrium conditions.

By analyzing the stochastic differential equation that describes the dynamics of a NEAT-RN, it is possible to derive the following expression for time averages of delayed correlations (see Appendix F):

$$\begin{aligned} \bar{\mathbb{X}}_{j,k} &= \frac{1}{t_I} \int_0^{t_I} d\tau \, \mathbb{X}_{j,k}(\tau) \\ &= \frac{1}{t_I} \left[\Sigma \left(\mathbb{1} - e^{-t_I G C^{-1}} \right) C G^{-1} \right]_{j,k}. \end{aligned} \tag{7}$$

Figure 1(e) shows the normalized circulation coefficient $l = (\bar{\mathbb{X}}_{1,2} - \bar{\mathbb{X}}_{2,1})/\sqrt{\mathrm{var}(v_1)\mathrm{var}(v_2)}$ for an integration time of $t = 200$ ns and the comparison with the model best fit. As before, the agreement shows that the statistical properties of the signals can be reliably controlled and predicted.

Additionally, these results show that the device in Fig. 1(a) can be considered an electronic implementation of a Brownian gyrator, an elementary heat engine [48], using CMOS circuits. Previous implementations of Brownian gyrators have varied the environmental temperature directly by heating or cooling the circuit [49], which is more cumbersome than our electronic implementation.

NEAT-RNs with additional nodes allow for richer programmability than the minimal example considered thus far. In such circuits, one can split the nodes into visible and latent nodes. Then, the correlations among visible nodes can be shaped by their common interaction with latent ones, which naturally enhances the range of achievable distributions.

To experimentally establish this enhanced programmability, we built a 3-degrees-of-freedom (DOF) NEAT-RN that utilizes a latent inverter to cover a larger range of two-dimensional (2D) distributions, as shown in Fig. 2(a). The

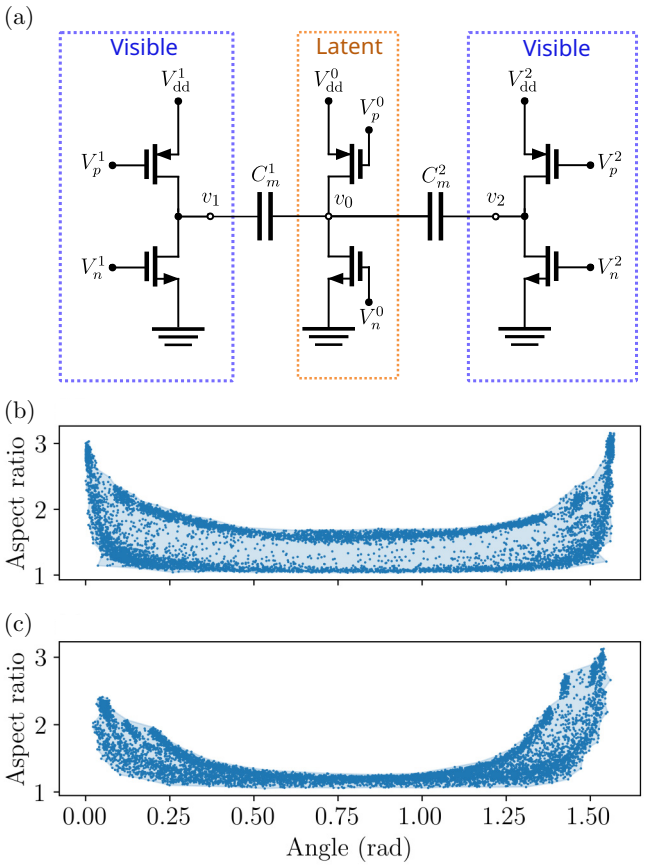

FIG. 2. Increasing the programmability of a NEAT-RN using latent variables. (a) Extending the circuit in Fig. 1(a) by adding an extra degree of freedom. The self-capacitance of each free node is omitted. (b) Observed points in the plane angle-aspect ratio for 8000 iterations of the control space exploration procedure, with $V_{dd}^{1/2} \simeq 5.5 V_T$ and $V_{dd}^0 \simeq 7 V_T$. (c) Results of an analogous protocol applied to the circuit in Fig. 1(a).

additional DOF mediates the coupling between the two outputs, allowing for richer control of their correlation.

We studied the programmability of our NEAT-RNs by exploring their control spaces for extreme covariance matrices. Specifically, for fixed powering voltages $V_{dd}^{0/1/2}$, we generated gate voltages $V_{n/p}^i$ (in the range $[0, 1.75\ \mathrm{V}]$) via a sampling procedure designed to find configurations with extreme aspect ratios. The results are shown in Fig. 2.

By comparing Figs. 2(b) and 2(c), we can see that our 3-DOF NEAT-RN is much more programmable than the 2-DOF version. For any given value of θ, the 3-DOF circuit allows α to be controlled within a much larger range than the 2-DOF circuit. In fact, for values of θ near $\pi/4$, α can barely be controlled for the 2-DOF circuit, whereas the 3-DOF circuit still features full programmability.

For a circuit to be an efficient entropy source in a probabilistic computer, it must generate fluctuations large enough to affect downstream devices. For thermally driven electrical systems, this means the noise generator must

produce voltage fluctuations comparable to V_T. This interaction voltage scale applies to a broad class of physical phenomena, including semiconductors and electrochemical reactions [50].

However, realizable passive circuits generate weak fluctuations and are not efficient in practical applications. Specifically, in a one-dimensional (1D) *RC* circuit,

$$\frac{\mathrm{var}(V)^{RC}}{V_T^2} = \frac{C_T}{C}, \tag{8}$$

where $C_T = q_e^2/k_bT$ is the thermodynamic capacitance scale, which is approximately 6 aF at room temperature. Circuits fabricated using the latest transistor processes like the one used here feature capacitances much larger than this, $C \gtrsim 300$ aF.

As such, the noise amplification provided by NEAT-RNs is crucial to their utility in room-temperature systems. For the 1D case of our NEAT-RN operating at the balance point of Eqs. (3) and (4), the variance of the voltage fluctuations is enlarged compared to a passive *RC* circuit,

$$\mathrm{var}(V) = \frac{1+\exp\left(V_{\mathrm{dd}}/2V_T\right)}{2}\,\mathrm{var}(V)^{RC} \tag{9}$$

the amplification factor depends exponentially on V_{dd} and is around 10 for $V_{\mathrm{dd}} \approx 6V_T$.

Because this amplification is intrinsic to the inverter and no complex external circuitry is used, it is achieved efficiently. Specifically, we define the energy consumed by the circuit per random sample as $E = P\tau$, where τ is the correlation timescale of the output signal, and P is the dc power consumption $P = V_{\mathrm{dd}}I^*$ given the dc current I^*. At the balance point, τ is

$$\tau = \frac{C}{G}, \tag{10}$$

where G is given by Eq. (3). The energy per sample follows,

$$E = \frac{V_{\mathrm{dd}}C^2}{q_e}\,\mathrm{var}(V)\tanh\left(\frac{V_{\mathrm{dd}}}{4V_T}\right), \tag{11}$$

where $\mathrm{var}(V)$ is as in Eq. (9).

Equations (9) and (10) elucidate a practically useful property of our system: the timescale and variance of the noise produced by our circuit are independently controllable. τ can be made arbitrarily large or small (within practical limits) by appropriately manipulating the gate control voltages with respect to V_{dd}. In contrast, the variance depends only on the powering voltage. From Eq. (11), we can see that the energy consumed per sample does not depend on τ and scales linearly with the desired variance (in the limit $V_{\mathrm{dd}} \gg V_T$).

The parameters found from the previous fitting can be used along with Eqs. (10) and (11) to find that NEAT-RNs could be used as a performant entropy source in a probabilistic computing system. Namely, taking $C \approx 1000$ aF, $I_0^p \approx 1$ nA, and $\Delta V = 5.5V_T$, we find that $E \approx 15$ aJ. In the same scenario, the practical minimum value of τ will be achieved when $V_p = 0$, at which point $\tau \approx 1$ ns.

Overall, we have shown that predictable, programmable, and performant p circuits can be built using networks of subthreshold transistors. These subthreshold networks can now be easily integrated with other circuitry to build probabilistic computers using advanced transistor processes. We have already proposed one such architecture in Ref. [29] and hope to report on its implementation in a future contribution.

Moreover, our results motivate a deeper exploration into *probabilistic integrated circuit design*. This burgeoning subfield of analog design is mostly unexplored, offering a rich landscape for new, useful circuit topologies and scientific discoveries. These discoveries could include other theoretical developments, building on the work in Ref. [27], or further experimental work to validate these theories.

ACKNOWLEDGMENTS

T.M. would like to thank Isaac Chuang for his invaluable advice on experimental design and the writing of the manuscript.

DATA AVAILABILITY

The data that support the findings of this article are openly available [51].

APPENDIX A: FABRICATION, CONTROL, AND MEASUREMENT OF THE DEVICES

The experiments conducted in this work utilized a test chip specifically designed to characterize noisy subthreshold circuits in detail. Our chip featured 8-bit DACs with a dynamic range of $[0, 0.175\ \mathrm{V}]$ that were used for manipulating control voltages. The output signals of each experiment were measured using high-bandwidth and high-input-impedance amplifiers, which were also implemented on the same die. This amplification chain allowed the analog signals to be routed off chip for measurement using a 1-GHz oscilloscope.

APPENDIX B: SHOT-NOISE MODELS AND THEIR DIFFUSIVE LIMIT

We consider the stochastic description of nonlinear electronic circuits developed in Ref. [27], where each conduction device in the circuit exhibits shot noise. The state of the circuit is described by the net number of elementary charges in the free nodes (i.e., the nodes that are not

regulated by voltage sources), given by a vector $n \in \mathbb{N}^d$, where d is the number of free nodes. Pairs of free nodes can be connected via conduction devices (diodes, tunnel junctions, transistors, etc.) that are identified by an integer index $\rho > 0$. If a conduction device is connected between two free nodes, then elementary charges can jump between them in both directions. For each device ρ, we assign a transition rate $\lambda_{+\rho}(n)$ to forward conduction events $n \to n + \Delta_\rho$, and a transition rate $\lambda_{-\rho}(n)$ to backward conduction events $n \to n + \Delta_{-\rho}$, with $\Delta_\rho = -\Delta_{-\rho}$. The forward direction is arbitrary, and the vectors Δ_ρ encode the change in the state n corresponding to each jump or transition.

For any state n, the voltages of the free nodes can be computed as $v = q_e C^{-1} n + v_r$, where C is the Maxwell capacitance matrix of the free nodes, q_e is the charge of the elementary charges, and v_r is a constant vector that depends on the regulated voltages. Let $P_t(v)$ be the probability to observe voltages v at time t. Given the previous description, $P_t(v)$ evolves according to the master equation:

$$\partial_t P_t(v) = \sum_\rho \lambda_\rho(v - q_e C^{-1}\Delta_\rho) P_t(v - q_e C^{-1}\Delta_\rho) - \sum_\rho \lambda_\rho(v) P_t(v), \tag{B1}$$

where we abuse notation by considering the rates $\lambda_\rho(v)$ to be now functions of the voltages v. A diffusive approximation of this Markov jump process can be obtained by a second-order truncation of the Kramers-Moyal expansion of Eq. (B1), which corresponds to the limit of large capacitances $||C|| \gg C_T$. In that case, Eq. (B1) reduces to a Fokker-Planck equation, which implies that the dynamics of the system can be approximately described by an Itô stochastic differential equation (SDE) of the form:

$$C \cdot dv = \mu(v)dt + \sqrt{2K(v)} \cdot dW, \tag{B2}$$

where W is a vector of independent Wiener processes. This approximation is uncontrolled and fails to capture large fluctuations [52,53], but properly describes the first and second moments of $P_t(v)$ in the limit of large capacitances [54]. The drift vector $\mu(v)$ and diffusion matrix $K(v)$ can be obtained from the transition rates $\lambda_\rho(v)$. In turn, the two transition rates $\lambda_{\pm\rho}(v)$ associated to the conduction device ρ can be related to its phenomenological IV curve $I_\rho(\Delta v)$ via the thermodynamic consistency relations [27]:

$$\begin{aligned} \lambda_\rho(v) - \lambda_{-\rho}(v) &= I_\rho(\Delta v_\rho)/q_e \\ \lambda_\rho(v) + \lambda_{-\rho}(v) &= \coth\left(\Delta v_\rho / 2V_T\right) I_\rho(\Delta v_\rho)/q_e. \end{aligned} \tag{B3}$$

Using Eq. (B3), it is possible to obtain the following expressions for the drift vector and diffusion matrix:

$$\begin{aligned} \mu(v) &\equiv \sum_\rho I_\rho(\Delta v_\rho)\Delta_\rho, \\ K(v) &\equiv \frac{q_e}{2} \sum_\rho I_\rho(\Delta v_\rho) \coth\left(\Delta v_\rho / 2V_T\right) \Delta_\rho \cdot \Delta_\rho^T, \end{aligned} \tag{B4}$$

where Δv_ρ is the voltage drop across device ρ in state v.

For circuits with deterministic fixed-point attractors v^*, for which $\mu(v^*) = 0$, the stochastic dynamics in Eq. (B2) can be linearized to

$$C \cdot dv = -G \cdot (v - v^*)\, dt + \sqrt{2k_b G\mathcal{T}} \cdot dW, \tag{B5}$$

where we have defined the effective conductance matrix G with elements $G_{jk} \equiv -\partial_{v_k}\mu_j(v^*)$ and the effective temperature matrix $\mathcal{T} \equiv G^{-1}K(v^*)/k_b$. The steady-state distribution of the previous dynamics is given by Eqs. (1) and (2) in the main text.

Finally, we note that for a one-dimensional case the linearized dynamics of Eq. (B5) has the following steady-state autocorrelation function:

$$\mathbb{X}(\delta t) = \frac{k_b \mathcal{T}}{C} e^{-(G/C)|\delta t|}, \tag{B6}$$

which leads to the following Lorentzian one-sided power spectral density (PSD):

$$P(f) = \frac{P_0}{1 + (f/f_0)^2)}, \tag{B7}$$

with $P_0 = 4k_b\mathcal{T}/G$ and $f_0 = G/(2\pi C)$.

APPENDIX C: EKV-BASED MODEL OF AN INVERTER

We now consider a single inverter [the left or right pair of transistors in Fig. 1(a)]. According to the extension of the EKV model including DIBL effects as presented in Ref. [55], the current through the NMOS transistor is given by

$$I_n = I_0^n \log^2\left(1 + e^{(V_{gb} - V_{\rm th}^n)/2n_n} e^{-V_{sb}/2} e^{\gamma_n V_{ds}/2}\right) - I_0^n \log^2\left(1 + e^{(V_{gb} - V_{\rm th}^n)/2n_n} e^{-V_{db}/2} e^{-\gamma_n V_{ds}/2}\right), \tag{C1}$$

where I_0^n, $V_{\rm th}^n$, n_n, and γ_n are model parameters and the voltages $V_{gb} = V_n$, $V_{sb} = 0$, $V_{db} = V_{ds} = v$ are here expressed in units of the thermal voltage V_T. The same expression gives the current I_p through the PMOS transistor, this time in terms of parameters I_0^p, $V_{\rm th}^p$, n_p, and γ_p, by just replacing $I_p \to -I_n$ and using the voltages $V_{gb} = -(V_p - V_{\rm dd})$, $V_{sb} = 0$, $V_{db} = V_{ds} = -(v - V_{\rm dd})$.

It is useful to take a number of approximations in order to make analytical progress. In particular, we consider the subthreshold regime where $e^{(V_{gb}-V_T)/2n_{n/p}} \ll 1$, and neglect DIBL effects (i.e., we set $\gamma_n = \gamma_p = 0$). Then, the currents I_n and I_p reduce to the following functions of the output node voltage v:

$$\begin{aligned} I_p(v) &= \underbrace{I_0^p e^{-(V_p - V_{dd})/n_p}}_{c_p}(1 - e^{v - V_{dd}}), \\ I_n(v) &= \underbrace{I_0^n e^{V_n/n_n}}_{c_n}(1 - e^{-v}), \end{aligned} \tag{C2}$$

where we have now incorporated factors $e^{-V_{th}^{n/p}/n_{n/p}}$ into the respective constants $I_0^{n/p}$. The deterministic output voltage v^* satisfies $I_p(v^*) = I_n(v^*)$, which under the above approximations leads to the expression:

$$e^{v^*} = \frac{e^{V_{dd}}}{2}\left[\left(1 - \frac{c_n}{c_p}\right) + \sqrt{\left(1 - \frac{c_n}{c_p}\right)^2 + 4\frac{c_n}{c_p}e^{-V_{dd}}}\right]. \tag{C3}$$

Using this, we obtain that the effective conductance is given by

$$G = V_T^{-1}\sqrt{(c_p - c_n)^2 + 4c_p c_n e^{-V_{dd}}}. \tag{C4}$$

Also, the effective temperature is given by

$$k_b\mathcal{T} = \frac{q_e I^*}{2G}\left[\coth\left((V_{dd} - v^*)/2\right) + \coth\left(v^*/2\right)\right], \tag{C5}$$

where $I^* \equiv (c_p + c_n - V_T G)/2$ is the stationary current. The balanced conditions considered in the main text are achieved when $c_n = c_p$. The expressions in the main text also assume that the subthreshold slopes are 1 for all transistors (i.e., $n_{n/p} = 1$ for all inverters).

APPENDIX D: SPECTRAL ANALYSIS

Figure 3(a) shows the PSD of the signal v_1, obtained numerically from the time series, at different operating voltages. The dashed black lines over each PSD show the result of fitting them with the following model:

$$P(f) = \frac{P_0}{1 + (f/f_0)^2} + \frac{L}{f^\alpha} + B. \tag{D1}$$

The first term corresponds to the Lorentzian spectrum, which is expected from the theory in the previous sections. The second term aims to capture the pink noise dominating at low frequencies, while the last term accounts for a flat spectral contribution possibly associated to extrinsic noise sources (for example, the amplification stage).

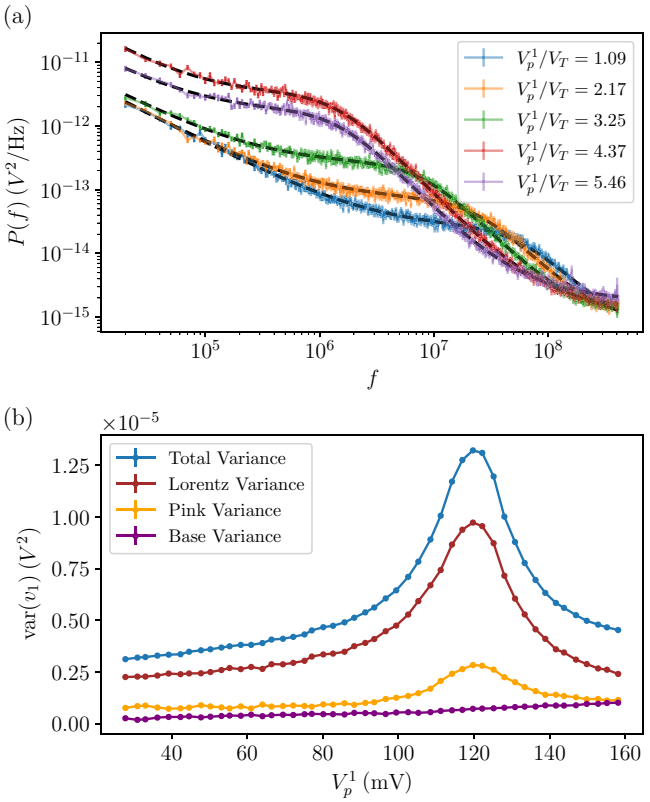

FIG. 3. (a) Power spectral density of the signal v_1 for different values of the control voltage V_p^1. (b) Total variance of the signal v_1, as well as its different spectral contributions, as a function of V_p^1. Same settings as in Fig. 1.

This decomposition allows to split the total power or variance of the signal into different contributions, as shown in Fig. 3(b). Finally, we note that the effective temperature can be computed from the parameters P_0 and f_0 as $k_b\mathcal{T} = Cf_0P_0\pi/2$, where C is the total output capacitance of the inverter in question [for example, for the left inverter it is $C = C_1 + 1/(1/C_2 + 1/C_m)$, in terms of the self-capacitances $C_{1/2}$ and the mutual capacitance C_m].

APPENDIX E: DATA ANALYSIS AND MODEL FIT

The comparison of the experimental data with the theoretical model proceeds in three stages: (i) determination of intrinsic parameters for each individual inverter, (ii) effective modeling of $1/f$ noise sources, and (iii) determination of global capacitance matrix based on observed correlations. The raw time series and the code used for the analysis can be found in Ref. [51].

In the first stage, for each inverter we simultaneously fit the average output voltage $\langle v\rangle$, the frequency f_0, and the effective temperature $k_b\mathcal{T}$ based on Eqs. (B4), (B5), and (C1). The results are shown in Fig. 4. Panels (a) and (b) show that the dynamics of the system is well captured by the model based on Eq. (C1), while panel (c)

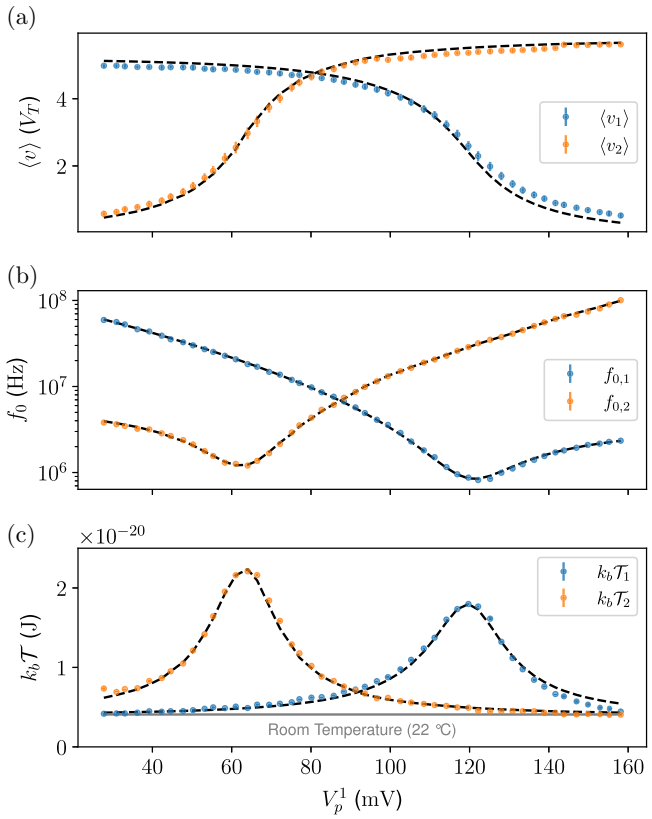

FIG. 4. For each individual inverter, (a) average voltage output, (b) frequency f_0, and (c) effective temperature $\mathcal{T}$ as obtained from the spectrum [see Eq. (B7)]. The dashed lines indicate the theoretical results from Eqs. (B4), (B5), and (C1) after fitting the three quantities simultaneously. Same settings as in Fig. 1.

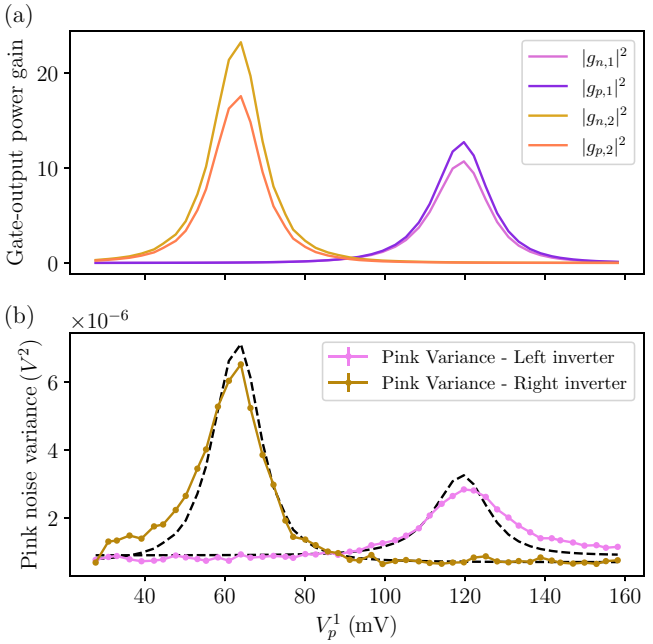

FIG. 5. (a) Power gains $|g_{n/p}|^2$ for each inverter, computed from the model with the parameters obtained from the fit in Fig. 4. (b) Total variance of the pink noise for each inverter. Dashed lines correspond to the best fits according to the model in Eq. (E1). Same settings as in Fig. 1.

shows that the shot-noise modeling assumption leading to $K(v)$ in Eq. (B4) is able to describe the intrinsic thermal fluctuations for the operating voltages employed.

In the second stage we aim to describe the variability of the low-frequency pink-noise variance [see Fig. 3(b)], which is the second largest contribution to the total variance in the signal. Low-frequency noise in MOS transistors is usually modeled as stochastic fluctuations in the threshold voltage V_{th}, caused by the presence of fluctuating charge traps in the gate oxide, which collectively give rise to a $1/f$ -like spectrum [33–37]. A small-signal analysis of the dc model of each inverter based on Eq. (C1) offers a simple approach to understand how fluctuations in V_{th} are mapped to the measured output. For this, we just need to consider the gains $g_{n/p} = |\partial v^*/\partial V_{\text{th}}^{n/p}|$, indicating how the deterministic output voltage v^* changes with small perturbations of each of the two threshold voltages. These gains can be easily computed from the model using the parameters fitted in the previous stage [see Fig. 5(a)]. Then, if $S_{n/p}$ is the total power of the fluctuations of the threshold voltage $V_{\text{th}}^{n/p}$ in the frequency range corresponding to the total observation window and sampling rate, the total power of low-frequency fluctuations in the output signal in the same frequency range is given by

$$S_{1/f} = g_n^2 S_n + g_p^2 S_p + S_0, \tag{E1}$$

where S_0 accounts for external sources of low-frequency noise, and it was assumed that the three sources of noise involved are independent. Figure 5 compares the total variance due to low-frequency noise as a function of the operating point, as well as the result from the fit using the model in Eq. (E1). We see that, despite its simplicity, this approach allows most of the variability to be explained.

In the last stage we compare the covariance matrix obtained by solving Eq. (2) in the main text with the experimentally observed covariance matrix for different operating points, which allows estimation of the self and mutual capacitances of the inverter outputs. This is done as follows. We compute the conductance G and the effective temperature $\mathcal{T}$ for each inverter at each operating point, using the model parameters obtained in the first stage. Then, given a capacitance matrix C constructed from proposed values of C_1, C_2, and C_m, we solve the Lyapunov equation in Eq. (2) to obtain an expected covariance matrix Σ. This covariance matrix is compared to the one estimated from the experimental data, which has the Lorentzian component of the variances as the diagonal elements and the observed correlation $\mathbb{X}_{1,2}(\delta t = 0)$ as the

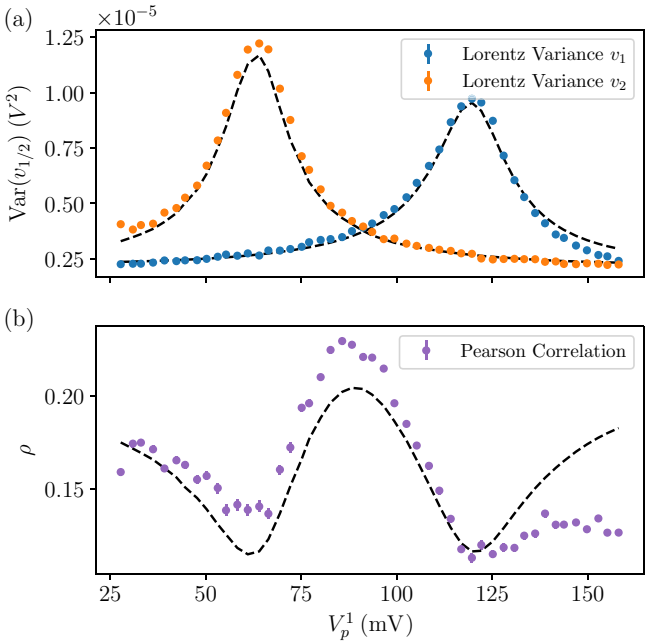

FIG. 6. (a) Lorentz variance and (b) Pearson correlation coefficient of the signals $v_{1/2}$ as a function of the operating point. Same settings as in Fig. 1.

nondiagonal elements. The results from this procedure are shown in Fig. 6.

Finally, Figs. 1(d) and 1(e) in the main text show the aspect ratio and angle of the covariance matrix of the raw time series (that is, including all noise contributions). The dashed lines in the same plots were computed from the fitted model by considering a covariance matrix $\Sigma_T = \Sigma_L + \Sigma_{1/f}$, where Σ_L is obtained by solving the Lyapunov equation in Eq. (2) and $\Sigma_{1/f}$ is a diagonal matrix with elements $S_{1/f,1}$ and $S_{1/f,2}$ computed according to Eq. (E1).

APPENDIX F: GYRATION COEFFICIENT

We now sketch the derivation of Eq. (7) for the delayed correlations. We first note that, at steady-state conditions, the delayed correlations $\mathbb{X}_{j,k}(\delta t)$ can be written as

$$\begin{aligned}\mathbb{X}_{j,k}(\delta t) &= \int dv \int dv'(v'_k - v^*_k)(v_j - v^*_j)P(v',t+\delta t|v,t)P(v) \\ &= \int dv\,(v_j - v^*_j)\left[e^{-\delta t\, C^{-1}G}\cdot(v-v^*)\right]_k P(v) \\ &= \left[e^{-\delta t C^{-1}G}\,\Sigma\right]_{k,j} = \left[\Sigma\, e^{-\delta t G C^{-1}}\right]_{j,k}, \end{aligned} \tag{F1}$$

where we have used that, for the linear process in Eq. (B5), the conditional probability $P(v',t+\delta t|v,t)$ is a Gaussian distribution with an exponentially relaxing mean value $\langle v'\rangle = v^* + e^{-\delta t\, C^{-1}G}\cdot(v-v^*)$, and that the stationary distribution $P(v)$ is given by Eq. (1). Equation (7) follows by just using that $\int_0^{t_I} d\tau e^{-\tau A} = A^{-1}(\mathbb{1} - e^{-t_I A})$ for any invertible matrix A.

[1] R. Dennard, F. Gaensslen, H.-N. Yu, V. Rideout, E. Bassous, and A. LeBlanc, Design of ion-implanted MOSFET's with very small physical dimensions, IEEE J. Solid-State Circuits **9**, 256 (1974).

[2] H. Nyquist, Thermal agitation of electric charge in conductors, Phys. Rev. **32**, 110 (1928).

[3] L. B. Kish, End of Moore's law: Thermal (noise) death of integration in micro and nano electronics, Phys. Lett. A **305**, 144 (2002).

[4] E. Rezaei, M. Donato, W. R. Patterson, A. Zaslavsky, and R. I. Bahar, Fundamental thermal limits on data retention in low-voltage CMOS latches and SRAM, IEEE Trans. Device Mater. Rel. **20**, 488 (2020).

[5] B. R. Zink, Y. Lv, and J.-P. Wang, Review of magnetic tunnel junctions for stochastic computing, IEEE J. Explor. Solid-State Comput. Devices Circuits **8**, 173 (2022).

[6] S. Chowdhury, A. Grimaldi, N. A. Aadit, S. Niazi, M. Mohseni, S. Kanai, H. Ohno, S. Fukami, L. Theogarajan, G. Finocchio *et al.*, A full-stack view of probabilistic computing with p-bits: Devices, architectures, and algorithms, IEEE J. Explor. Solid-State Comput. Devices Circuits **9**, 1 (2023).

[7] J. Kim, J.-K. Han, H.-Y. Maeng, J. Han, J. W. Jeon, Y. H. Jang, K. S. Woo, Y.-K. Choi, and C. S. Hwang, Fully CMOS-based p-bits with a bistable resistor for probabilistic computing, Adv. Funct. Mater. **34**, 2307935 (2024).

[8] I. Ahmed, P.-W. Chiu, W. Moy, and C. H. Kim, A probabilistic compute fabric based on coupled ring oscillators for solving combinatorial optimization problems, IEEE J. Solid-State Circuits **56**, 2870 (2021).

[9] W. Lee, H. Kim, H. Jung, Y. Choi, J. Jeon, and C. Kim, Correlation free large-scale probabilistic computing using a true-random chaotic oscillator p-bit, Sci. Rep. **15**, 1 (2025).

[10] J. Kim, S. S. Woo, and R. Sarpeshkar, Fast and precise emulation of stochastic biochemical reaction networks with amplified thermal noise in silicon chips, IEEE Trans. Biomed. Circuits Syst. **12**, 379 (2018).

[11] W. A. Borders, A. Z. Pervaiz, S. Fukami, K. Y. Camsari, H. Ohno, and S. Datta, Integer factorization using stochastic magnetic tunnel junctions, Nature **573**, 390 (2019).

[12] N. S. Singh, K. Kobayashi, Q. Cao, K. Selcuk, T. Hu, S. Niazi, N. A. Aadit, S. Kanai, H. Ohno, S. Fukami *et al.*, CMOS plus stochastic nanomagnets enabling heterogeneous computers for probabilistic inference and learning, Nat. Commun. **15**, 2685 (2024).

[13] R. Faria, K. Y. Camsari, and S. Datta, Low-barrier nanomagnets as p-bits for spin logic, IEEE Magn. Lett. **8**, 1 (2017).

[14] K. Y. Camsari, R. Faria, B. M. Sutton, and S. Datta, Stochastic p-bits for invertible logic, Phys. Rev. X **7**, 031014 (2017).

[15] K. Y. Camsari, S. Salahuddin, and S. Datta, Implementing p-bits with embedded MTJ, IEEE Electron. Device Lett. **38**, 1767 (2017).

[16] Y. Shao, C. Duffee, E. Raimondo, N. Davila, V. Lopez-Dominguez, J. A. Katine, G. Finocchio, and P. K. Amiri, Probabilistic computing with voltage-controlled dynamics in magnetic tunnel junctions, Nanotechnology **34**, 495203 (2023).

[17] D. Vodenicarevic, N. Locatelli, A. Mizrahi, J. S. Friedman, A. F. Vincent, M. Romera, A. Fukushima, K. Yakushiji, H. Kubota, S. Yuasa *et al.*, Low-energy truly random number generation with superparamagnetic tunnel junctions for unconventional computing, Phys. Rev. Appl. **8**, 054045 (2017).

[18] K. Yang, Q. Dong, Z. Wang, Y.-C. Shih, Y.-D. Chih, J. Chang, D. Blaauw, and D. Svlvester, in *2018 IEEE Symposium on VLSI Circuits* (IEEE, Honolulu, HI, USA, 2018), pp. 171–172.

[19] D. Edelstein, M. Rizzolo, D. Sil, A. Dutta, J. DeBrosse, M. Wordeman, A. Arceo, I. Chu, J. Demarest, E. R. Edwards *et al.*, in *2020 IEEE International Electron Devices Meeting (IEDM)* (IEEE, San Francisco, CA, USA, 2020), pp. 11.5.1–11.5.4.

[20] J. Daniel, Z. Sun, X. Zhang, Y. Tan, N. Dilley, Z. Chen, and J. Appenzeller, Experimental demonstration of an on-chip p-bit core based on stochastic magnetic tunnel junctions and 2D MoS_2 transistors, Nat. Commun. **15**, 4098 (2024).

[21] J. Kaiser, W. A. Borders, K. Y. Camsari, S. Fukami, H. Ohno, and S. Datta, Hardware-aware in situ learning based on stochastic magnetic tunnel junctions, Phys. Rev. Appl. **17**, 014016 (2022).

[22] P. Korkmaz, B. E. Akgul, K. V. Palem, and L. N. Chakrapani, Advocating noise as an agent for ultra-low energy computing: Probabilistic complementary metal–oxide–semiconductor devices and their characteristics, Jpn. J. Appl. Phys. **45**, 3307 (2006).

[23] K. Palem and A. Lingamneni, Ten years of building broken chips: The physics and engineering of inexact computing, ACM Trans. Embed. Comput. Syst. (TECS) **12**, 1 (2013).

[24] J. Holleman, S. Bridges, B. P. Otis, and C. Diorio, 3 μW CMOS true random number generator with adaptive floating-gate offset cancellation, IEEE J. Solid-State Circuits **43**, 1324 (2008).

[25] J. Bae, J. Koo, C. Shim, and B. Kim, in *2024 IEEE International Solid-State Circuits Conference (ISSCC)* (IEEE, San Francisco, CA, USA, 2024), Vol. 67, pp. 284–286.

[26] R. Sarpeshkar, T. Delbruck, and C. A. Mead, White noise in MOS transistors and resistors, IEEE Circuits Devices Mag. **9**, 23 (1993).

[27] N. Freitas, J.-C. Delvenne, and M. Esposito, Stochastic thermodynamics of nonlinear electronic circuits: A realistic framework for computing around kT, Phys. Rev. X **11**, 031064 (2021).

[28] E. Morifuji, T. Yoshida, M. Kanda, S. Matsuda, S. Yamada, and F. Matsuoka, Supply and threshold-voltage trends for scaled logic and SRAM MOSFETs, IEEE Trans. Electron. Devices **53**, 1427 (2006).

[29] A. Jelinčič, O. Lockwood, A. Garlapati, G. Verdon, and T. McCourt, An efficient probabilistic hardware architecture for diffusion-like models, arXiv arXiv:2510.23972, Submitted to npj Unconventional Computing.

[30] G. Reimbold and P. Gentil, White noise of MOS transistors operating in weak inversion, IEEE Trans. Electron Devices **29**, 1722 (1982).

[31] S. Tedja, H. H. Williams, J. Van der Spiegel, F. M. Newcomer, and R. Van Berg, Noise spectral density measurements of a radiation hardened CMOS process in the weak and moderate inversion, IEEE Trans. Nucl. Sci. **39**, 804 (1992).

[32] H. Tian, B. A. Fowler, and A. El Gamal, in *Sensors, Cameras, and Systems for Scientific/Industrial Applications* (SPIE, San Jose, CA, United States, 1999), Vol. 3649, pp. 177–185.

[33] A. G. Mahmutoglu, A. Demir, and J. Roychowdhury, in *2013 IEEE/ACM International Conference on Computer-Aided Design (ICCAD)* (IEEE, San Jose, CA, United States, 2013), pp. 500–507.

[34] B. Stampfer, A. Grill, and M. Waltl, in *Noise in Nanoscale Semiconductor Devices* (Springer, 2020), pp. 229–257.

[35] H. Tian and A. El Gamal, Analysis of $1/f$ noise in switched MOSFET circuits, IEEE Trans. Circuits Syst. II: Analog Digit. Signal Process. **48**, 151 (2001).

[36] C. Jakobson, I. Bloom, and Y. Nemirovsky, $1/f$ noise in CMOS transistors for analog applications from subthreshold to saturation, Solid State Electron. **42**, 1807 (1998).

[37] M. Kirton and M. Uren, Noise in solid-state microstructures: A new perspective on individual defects, interface states and low-frequency ($1/f$) noise, Adv. Phys. **38**, 367 (1989).

[38] S. Ciliberto, A. Imparato, A. Naert, and M. Tanase, Statistical properties of the energy exchanged between two heat baths coupled by thermal fluctuations, J. Stat. Mech. **2013**, P12014 (2013).

[39] M. Baiesi, S. Ciliberto, G. Falasco, and C. Yolcu, Thermal response of nonequilibrium RC circuits, Phys. Rev. E **94**, 022144 (2016).

[40] N. Freitas, J.-C. Delvenne, and M. Esposito, Stochastic and quantum thermodynamics of driven RLC networks, Phys. Rev. X **10**, 031005 (2020).

[41] C. C. Enz and E. A. Vittoz, *Charge-Based MOS Transistor Modeling* (John Wiley & Sons, Ltd, 2006).

[42] T. Sekigawa and Y. Hayashi, Calculated threshold-voltage characteristics of an XMOS transistor having an additional bottom gate, Solid-State Electron. **27**, 827 (1984).

[43] S.-Y. Wu, C.-H. Chang, M. Chiang, C. Lin, J. Liaw, J. Cheng, J. Yeh, H. Chen, S. Chang, K. Lai *et al.*, in *2022 International Electron Devices Meeting (IEDM)* (IEEE, San Francisco, CA, USA, 2022) pp. 27.5.1–27.5.4.

[44] J. Liu, S. Mukhopadhyay, A. Kundu, S. Chen, H. Wang, D. Huang, J. Lee, M. Wang, R. Lu, S. Lin, Y. Chen, H. Shang, P. Wang, H. Lin, G. Yeap, and J. He, in *2020 IEEE International Electron Devices Meeting (IEDM)* (IEEE, San Francisco, CA, USA, 2020), pp. 9.2.1–9.2.4.

[45] N. Ohga, S. Ito, and A. Kolchinsky, Thermodynamic bound on the asymmetry of cross-correlations, Phys. Rev. Lett. **131**, 077101 (2023).

[46] S. Liang and S. Pigolotti, Thermodynamic bounds on time-reversal asymmetry, Phys. Rev. E **108**, L062101 (2023).

[47] J. Gu, Thermodynamic bounds on the asymmetry of cross-correlations with dynamical activity and entropy production, Phys. Rev. E **109**, L042101 (2024).

[48] R. Filliger and P. Reimann, Brownian gyrator: A minimal heat engine on the nanoscale, Phys. Rev. Lett. **99**, 230602 (2007).

[49] K.-H. Chiang, C.-L. Lee, P.-Y. Lai, and Y.-F. Chen, Electrical autonomous Brownian gyrator, Phys. Rev. E **96**, 032123 (2017).

[50] S. Arrhenius, Über die Dissociationswärme und den Einfluss der Temperatur auf den Dissociationsgrad der Elektrolyte, Z. Phys. Chem. **4**, 96 (1889).

[51] Extropic Corp., Dataset for "Taming non-equilibrium thermal fluctuations in subthreshold CMOS circuits", Zenodo (2026), https://doi.org/10.5281/zenodo.18636981

[52] P. Hanggi, H. Grabert, P. Talkner, and H. Thomas, Bistable systems: Master equation versus Fokker-Planck modeling, Phys. Rev. A **29**, 371 (1984).

[53] D. Roberts, T. McCourt, G. Massarelli, J. Rothschild, and N. Freitas, Improved diffusive approximation of Markov jump processes close to equilibrium, Phys. Rev. Res. **8**, 013161 (2026).

[54] A. Gopal, M. Esposito, and N. Freitas, Large deviations theory for noisy nonlinear electronics: CMOS inverter as a case study, Phys. Rev. B **106**, 155303 (2022).

[55] A. Low and P. Hasler, in *42nd Midwest Symposium on Circuits and Systems (Cat. No. 99CH36356)* (IEEE, Las Cruces, NM, USA, 1999), Vol. 1, pp. 141–144.

驯服非平衡热涨落 (Taming Nonequilibrium Thermal Fluctuations...)

> 本文档为论文《Taming Nonequilibrium Thermal Fluctuations in Subthreshold CMOS Circuits》的逐页对照翻译版。

驾驭亚阈值 CMOS 电路中的非平衡热涨落

作者:
Nahuel Freitas[*,†], Geremia Massarelli , Jeremy Rothschild , Dylan Keane , Ethan Dawe, Sewook Hwang , Akhil Garlapati[*,†], and Trevor McCourt[*,‡]

Extropic Corporation, Cambridge, Massachusetts, USA (美国马萨诸塞州剑桥 Extropic 公司)

(收稿：2025年7月4日；修回：2026年1月16日；录用：2026年2月12日；发表：2026年3月18日)

一、 摘要

随着 CMOS 技术比例的缩小，热涨落越来越多地影响电路行为，对传统的电路设计提出了挑战。然而，在 **概率计算** 这一新兴领域，热噪声引入的固有随机性目前正在作为一种潜在的资源被探索。本工作展示了一个完全基于 CMOS 的实验平台，实现了对其内部热涨落的直接控制。这些装置起到了 **可编程的多变量高斯采样器** 的作用，为高能效的随机计算提供了一个硬件原语，并展示作为关于电子噪声和随机热力学的研究实验平台。

DOI: 10.1103/5l2z-3f1h

正文开始

【左栏】 (Left Column)

二、 正文背景与引言

CMOS 技术的激进微型化是一把双刃剑：随着晶体管电路在尺寸上的缩小，它变得更快且更节能 [1]，但也会变得噪声更大 [2]。随着器件尺寸和电源电压继续被推向其热力学极限，晶体管固有的噪声将开始扰乱传统的确定性计算机架构 [3,4]。

最近有一些提议提出，这种由噪声带来的显而易见的障碍可以通过在计算系统中构建有意设计的 **随机概率电路 (*p* 电路)** 来绕过 [5-11]。*P* 电路利用所有器件中存在的噪声来生成满足对计算有用的概率分布下的样本。

与纯粹的确定性方法相比，当运行严重依赖随机采样的特定算法时，概率计算机架构可以更具能效。随机采样在确定性计算机上是昂贵的：必须在计算机中采用包含数千个用于生成伪随机数的晶体管的复杂电路 [12]。这些大型电路耗费的能量，与那些实现类似加法这样计算内容更丰富的操作的电路消耗的能量不相上下。

【右栏】 (Right Column)

为了使 *p* 电路在计算中具实际实用价值，它必须是 **可预测的、可编程的并且是高性能的**。可预测性意味着 *p* 电路的随机动力学遵循某些可用于对其进行工程设计的简单物理模型。如果可以运行时调节它进行采样的分布，那么 *p* 电路就是具可编程性的。一个 *p* 电路的性能是由相关时间（correlation time）、能耗和物理尺寸来衡量的，这些共同量化了使用该电路进行随机采样的空间、时间和能量成本。

当前对 *p* 电路的实现，在这些关键领域至少有一项有所欠缺。利用磁隧道结构建的 *p* 电路是一个极佳的前景，具有充分描述的随机动力学模型 [13]，且易于编程 [14-16]。尽管这些器件在原则上与 CMOS 工艺兼容 [17]，但是关于集成的研究仍在进行中 [18,19]，这限制了短期的性能 [20,21]。为了避免这些集成问题，开发者也考虑过仅包含晶体管的 *p* 电路架构 [22,23]。然而，目前的方法通常依赖极其敏感的现象，诸如双稳态锁存器在加电时的随机性 [24,25]，或者是基于对噪声的粗略处理 [22]，使得编程和预测变得困难。

在深度亚阈值状态下运行的晶体管电路是构建实际 *p* 电路的自然候选者。在这些电路中，电荷传输主要是受热激活的，导向散粒噪声动力学 [26]。最近，散粒噪声模型已通过基于马尔可夫跳跃过程 (MJPs) 的技术从单晶体管水平推广到晶体管网络 [27]，表明亚阈值电路的随机动力学可以被严格预

测。通过控制，亚阈值网络也易于编程... *(注：页面结束，接下页)*

页脚脚注 (Footnotes):

- * 联络作者：nfreitas@extropic.ai
- † 这些作者对本工作贡献均等
- ‡ 联络作者：trevor@extropic.ai

【左栏】 (Left Column)

此外，小型晶体管会泄露更多的电流，从而提升亚阈值电路的性能 [28]。

三、 NEAT-RN 电路架构与稳态电压控制

本文通过实验证明，使用亚阈值晶体管可以构建实用的 p **电路**。具体而言，我们介绍并表征了一类可以通过电压编程的、从多变量高斯分布中进行采样的电路。这些电路实现了在多个自由度之间控制相关性的能力，并且作为一种强大的原语（primitive），既可以单独用作为 p 电路，也可以作为在更大电路中执行非高斯采样操作的一部分（其中最具代表性且最直接的就是 p 比特 [11]）。我们的工作为利用 p 电路的近期、大规模计算机铺平了道路；我们已经将这里列出的原理应用到了一个运行类扩散模型（diffusionlike models）的概率计算系统的设计中 [29]。

除了我们的工作在概率计算方面的潜力外，通过验证文献 [27] 中提出的 MJP 模型，它也极大地推进了我们在物理层面上对亚阈值晶体管中散粒噪声（shot noise）的理解。虽然有很多研究单晶体管水平散粒噪声的工作 [26,30,31]，但在大型电路中研究噪声物理规律的工作仍然很有限，且通常是针对特定应用的 [32]。我们的工作通过实验数据，测试了一个简单且通用的亚阈值晶体管网络噪声模型，使得该模型可以在未来的工程实践中放心地使用。

本文的剩余部分将详细介绍我们的高斯采样电路，我们将其称为 **非平衡、可调温度电阻网络（NEAT-RNs）**。我们将首先介绍 NEAT-RNs，并解释（正如其名字所暗示的）如何使用电压控制来对其稳态电压分布进行编程。然后，我们将展示文献 [27] 中的 MJP 模型可以准确预测对一个简单的 2D NEAT-RN 的行为的实验测量结果。接下来，我们将表明，通过引入介导相互作用的额外自由度，可以显著增强 NEAT-RNs 的可编程性。最后，我们将讨论 NEAT-RNs 的速率和能效，并证明它们足以为现代概率计算系统的一部分提供所需的性能。

NEAT-RNs 由多个具有独立栅极控制的 CMOS 反相器组成，其中互电容耦合了不同反相器的输出。这一类中最简单的非平凡示例如 **图 1(a)** 所示。下文讨论的实验涉及到测量不同工作电压下信号 $v = (v_1, v_2)$ 的统计特性（关于时间序列的示例，请参见 **图 1(c)**）。这些信号的大部分变率可由两个噪声源来解释：(i) 与电荷通过单独晶体管传输相关的热涨落；以及 (ii) 每个晶体管整体电导率的低频涨落。虽然第一项贡献具有基础物理学本质，因为它具有…… *(接右栏)*

【右栏】 (Right Column)

……纯粹的热力学起源 [26,27]，第二项通常被认为是由材料缺陷引起的，这些缺陷起到波动电荷陷阱的作用 [33-37]。将这些获得的数据与一个能够整合两种噪声源的解析模型进行对比。然而，在接下来的内容中，我们仅将讨论局限在对 **热涨落** 的解析描述上，因为热涨落是占主导地位的，在由测量时长和采样率给定的频率范围内，它们贡献了总信号功率的约 70%（参见附录 D）。

在一个工作点附近线性化之后，NEAT-RNs 变得等效于一个含有噪声的 RC 网络 [38-40]，其中每个电阻的有效电导和有效温度都可以随意控制 [参见 **图 1(b)**]。当有效温度相等时，系统达到一个 **平衡稳态概率分布** $P(v)$，该分布完全由电容决定，而电容在纳米级电路中是无法控制的。然而，如果有效温度不同，系统将达到一个 **非平衡稳态分布**，该分布开始取决于有效温度和电导。通过这种方式，可以通过操纵电压 V_{dd}^i 和 $V_{\mathrm{n/p}}^i$ 来控制稳态分布 [参见 **图 1(f) 和 1(g)**]。

具体而言，将文献 [27] 的 MJP 形式与亚阈值晶体管的 Enz-Krummenacher-Vittoz (EKV) 模型 [41] 相结合，可以发现 NEAT-RN 的稳态涨落近似呈现高斯（Gaussian）分布：

$$P(v) \propto \exp\left(-\frac{1}{2}(v - v^*)^T \Sigma^{-1} (v - v^*)\right). \quad (1)$$

此处，v 是电路中每个节点的电压向量，v^* 是每个电压的直流（dc）电平，而 Σ 是稳态协方差矩阵。Σ 由 **李雅普诺夫方程（Lyapunov equation）** 的解给出：

$$G\Sigma C + C\Sigma G = 2k_b G^{1/2} T G^{1/2}, \quad (2)$$

其中 G 是与每个反相器关联的有效线性电导的对角矩阵，T 是有效温度的对角矩阵，而 C 是电路的麦克斯韦电容矩阵。T 和 G 的矩阵元素可以显式地用电路的控制电压来写出；参见附录 B 和 C。

在每个反相器皆处于平衡状态从而满足 $v_i^* = V_{\rm dd}/2$，且每个晶体管的亚阈值斜率参数接近 1 的极限下（参见附录 B），G 和 T 的矩阵表达式呈现为直观的形式：

$$G_{ii} = 2\frac{I_0^p}{V_T}\exp\left((V_{\rm dd}/2 - V_p^i)/V_T\right), \quad (3)$$

$$T_{ii} = T\frac{1+\exp\left(V_{\rm dd}/2V_T\right)}{2}. \quad (4)$$

此处，I_0^p 是每个晶体管的 EKV 模型电流参数。T 是系统的物理温度。

> **插图/图注：RN 的可预测且可编程的高斯采样。**

- **(a)** 一个简单的 NEAT-RN：两个独立控制、电容耦合的 CMOS 反相器。
- **(b)** NEAT-RN 在直流（dc）工作点附近的涨落等效于一个具有可控有效电导和温度的线性 RC 电路的涨落。
- **(c)** 箭头指示的工作点处测得的电压 v_1 和 v_2 的时间序列快照。
- 对于正文中提到的沿电压扫描路径的不同点：
  - **(d)** 信号 v_1 和 v_2 的协方差矩阵的特征值长宽比（Aspect ratio α）。
  - **(e)** 该矩阵的主成分夹角（θ）。
  - 以及 **(f)** 归一化回转系数（gyration coefficient） I（积分时间 $t_I = 200\ \mathrm{ns}$）。
- **(g)** 延迟自相关（左）和互相关（右）函数的示例。
- **(h)** 两个工作点下信号 v_1 和 v_2 的中心化直方图示例。虚线表示主轴。

在所有情况下，我们固定电源电压 $V_{\rm dd}^1 = 137 \pm 1\ \mathrm{mV}$，$V_{\rm dd}^2 = 142 \pm 1\ \mathrm{mV}$，NMOS 栅极电压 $V_{\rm n}^1 = V_{\rm n}^2 = 76 \pm 1\ \mathrm{mV}$。PMOS 栅极电压满足 $V_{\rm p}^1 + V_{\rm p}^2 = 200 \pm 1\ \mathrm{mV}$。

**

正文文本

【左栏】 (Left Column)

……并且 $V_T = k_b T/q_e$ 为相关的热电压（q_e 为电子电荷）。我们选择利用平衡约束从该表达式中消除控制电压 $V_{\rm n}^i$。该决定是任意的，表达式本可以同样轻易地以消除 $V_{\rm p}^i$ 的形式写出。

这种极限情况清楚地表明，**NEAT-RNs 具有极高的可编程性**：各支路的有效电导可以通过改变相对于 $V_{\rm dd}$ 的栅极控制电压来设定，而通过将 $V_{\rm dd}$ 提高到地电位以上，可以将有效温度相对于实际环境温度提高。G_{ii} 和 T_{ii} 能取得的潜在值受到**中等反型**（moderate inversion）发生的限制，一旦到达该点，用于推导方程 (2) 的散粒噪声模型假设就失效了。只要器件处于亚阈值（subthreshold）状态，就有可能独立控制 $\mathcal{T}$ 和 G，从而用广泛的协方差矩阵对 p 电路进行编程。

为了在经验上确立我们的 p 电路的可预测性和可编程性，我们使用先进的 **TSMC FinFET** [42-44] 工艺制造了图 1(a) 所示的电路，并将方程 (2) 拟合到其稳态电压分布上。具体而言，除了 PMOS 控制电压以外，我们固定了所有电压，并对 PMOS 控制电压进行扫描（sweep）以满足…… *(接右栏)*

【右栏】 (Right Column)

……满足 $V_{\rm p}^1 + V_{\rm p}^2 = 200 \pm 1\ \mathrm{mV}$。在每个工作点处测量了电压的时间序列，并据此估算出一个协方差矩阵（拟合过程的具体细节在附录 E 中概述）。

我们通过该矩阵的谱（spectrum）来表征所测量的协方差矩阵。具体而言，我们计算了特征值 λ_k 和特征向量 q_k，满足 $\Sigma q_k = \lambda_k q_k$ 且 $\lambda_0 \geq \lambda_1$。从 Σ 的特征值和特征向量出发，我们定义了特征值长宽比 α 和主成分夹角 θ：

$$\alpha \equiv \sqrt{\lambda_0/\lambda_1}, \quad \theta \equiv \arctan((q_0)_1/(q_0)_2). \quad (5)$$

观察到的稳态分布示例在图 1(h) 中展示（*注：原文写的是 1(f) 和 1(g)，应与插图结合看*）。

图 1(c) 和 1(d) 比较了 α 和 θ 对 $V_{\rm p}^1$ 的观测依赖关系与方程 (2) 的最佳拟合。这些结果表明，通过改变工作电压 $V_{\rm n/p}^{1/2}$ 可以可靠地控制信号 v_1 和 v_2 的涨落。此外，我们观察到基于方程 (2) 的简单建模能有效地捕捉数据的主要特征。因此，产生的信号既是可控的也是可预测的。

【左栏】 (Left Column)

四、 随机动力学模型验证与环流系数

为了确立 MJP 模型能够预测 NEAT-RN 的动力学特性（而不仅仅是稳态分布），我们测量了电压状态的 **环流 (circulation)**，并将其与模型的预测进行对比。这种环流可以通过系数 $L(\delta t) \equiv \langle v \times \delta v \rangle$ 来量化，其中 $\delta v = v(t+\delta t) - v(t)$ 是时间 δt 内的位移。在稳态条件下，可以将 L 重写为：

$$L(\delta t) = \mathbb{X}_{1,2}(\delta t) - \mathbb{X}_{2,1}(\delta t), \quad (6)$$

其中 $\mathbb{X}_{j,k}(\delta t) \equiv \langle v_j(t) v_k(t+\delta t) \rangle - \langle v_j(t) \rangle \langle v_k(t+\delta t) \rangle$ 是延迟相关（delayed correlation），可以从时间序列中获取。先前的表达式被称为 **互相关不对称性**，是时间反演对称性破缺（time-reversal symmetry breaking）的一种衡量 [45-47]。例如，在大约图 1(g) 中，展示了特定工作点下归一化的延迟相关 $\chi_{j,k} \equiv \mathbb{X}_{j,k} / \sqrt{\mathrm{var}(v_j)\mathrm{var}(v_k)}$。观察到延迟相关确实是不对称的，这表明由于非平衡条件，时间反演不变性（time-reversal invariance）遭到了破坏。

通过分析描述 NEAT-RN 动力学的随机微分方程，可以推导出延迟相关的时间平均值的以下表达式（参见附录 F）：

$$\bar{\mathbb{X}}_{j,k} = \frac{1}{t_I} \int_0^{t_I} dt\, \mathbb{X}_{j,k}(\tau)$$

$$= \frac{1}{t_I} \left[\Sigma \left(1 - e^{-t_I G C^{-1}} \right) C G^{-1} \right]_{j,k}. \quad (7)$$

图 1(e) 展示了积分时间为 $t = 200\ \mathrm{ns}$ 时的归一化 **环流系数**（原文称 circulation, 亦作 gyration） $l = (\bar{\mathbb{X}}_{1,2} - \bar{\mathbb{X}}_{2,1}) / \sqrt{\mathrm{var}(v_1)\mathrm{var}(v_2)}$，以及与模型最佳拟合的对比。与之前一样，这种一致性表明信号的统计特性可以得到可靠的控制和预测。

此外，这些结果表明，图 1(a) 中的装置可以被看作是使用 CMOS 电路对 **布朗回转器 (Brownian gyrator)**（一种基本的微观热机 [48]）的电子学实现。先前布朗回转器的实现主要通过加热或冷却电路来直接改变环境温度 [49]，这比我们的电子学实现要繁琐得多。

NEAT-RNs 节点拓展: 包含额外节点的 NEAT-RNs 允许比目前考虑的极小示例具有更丰富的可编程性。在这样的电路中，可以将节点分为 **可见节点 (visible nodes)** 和 **潜节点 (latent nodes)**。然后，可见节点之间的相关性可以通过它们与潜节点的共同相互作用来构建，这极其自然地扩大了可实现分布的范围。

为了在实验上确立这种增强的可编程性，我们构建了一个使用潜反相器的 **3 自由度 (3-DOF)** NEAT-RN，以覆盖更广泛的二维 (2D) 分布，如图 2(a) 所示。 *(接右栏)*

【右栏】 (Right Column)

> **插图/图注：RN 的可编程性。**

- **(a)** 通过增加一个额外的自由度来扩展图 1(a) 中的电路。省略了每个自由节点的自电容。
- **(b)** 在控制空间探索（control space exploration）过程运行 8000 次迭代后，在 [夹角-长宽比] 平面上观察到的点，其中电源电压 $V_{\mathrm{dd}}^{1/2} \approx 5.5 V_T$，$V_{\mathrm{dd}}^{0} \approx 7 V_T$。
- **(c)** 应用于图 1(a) 中电路的类似协议的结果。

**

正文文本

……增加的自由度（DOF）介导了两个输出之间的耦合，从而允许对它们的相关性进行更丰富的控制。

我们通过探索控制空间中极端的协方差矩阵，研究了 NEAT-RNs 的可编程性。具体而言，在一组固定的电源电压 $V_{\mathrm{dd}}^{0/1/2}$ 条件下，我们通过一项旨在寻找具有极端长宽比（extreme aspect ratios）的配置的采样过程，生成了栅极电压 $V_{\mathrm{n/p}}^{i}$（范围在 $[0, 1.75\ \mathrm{V}]$ 之间）。结果如图 2 所示。

通过比较图 2(b) 和 2(c)，我们可以看到我们的 **3-DOF NEAT-RN 明显比 2-DOF 版本更具可编程性**。对于任何给定的 θ 值，3-DOF 电路允许将 α 控制在一个比 2-DOF 电路大得多的范围内。事实上，对于 θ 接近 $\pi/4$ 的值，2-DOF 电路的 α 几乎无法被控制，而 3-DOF 电路仍能提供完全的可编程性。

五、 稳态噪声放大与能效分析

为了使电路在概率计算机中充当高效的熵源（entropy source），它必须产生足以影响下游器件的涨落。对于利用热驱动的电子系统，这意味着噪声发生器必须……

【左栏】 (Left Column)

……产生与 V_T 相当的电压涨落。这种相互作用电压标度（interaction voltage scale）适用于广泛的一类物理现象，包括半导体和电化学反应 [50]。

然而，可实现的无源电路产生极其微弱的涨落，且在实际应用中并不高效。具体而言，在一维（1D）RC 电路中：

$$\frac{\mathrm{var}(V)^{RC}}{V_T^2} = \frac{C_T}{C}, \quad (8)$$

其中 $C_T = q_e^2/k_bT$ 是热力学电容标度，在室温下约为 6 aF（1 aF = 10^{-18} 法拉）。使用最新的晶体管工艺（如本文所用的工艺）制造的电路，其电容比这要大得多，$C \gtrsim 300$ aF。

因此，NEAT-RNs 提供的**噪声放大效果**，对于其在室温系统中的实用价值至关重要。对于运行在方程 (3) 和 (4) 平衡点处我们的 NEAT-RN 的 1D 情况而言，与无源 RC 电路相比，电压涨落的方差有所放大：

$$\mathrm{var}(V) = \frac{1+\exp\left(V_{\mathrm{dd}}/2V_T\right)}{2}\mathrm{var}(V)^{RC} \quad (9)$$

放大因子以指数形式取决于 V_{dd}，对于 $V_{\mathrm{dd}} \approx 6V_T$，放大倍数约为 10。

由于这种放大效应是反相器固有的，且没有使用复杂的外部电路，因此它是以高效的方式实现的。具体而言，我们将每个随机样本消耗的能量定义为 $E = P\tau$，其中 τ 是输出信号的相关时间尺度（correlation timescale），而 P 是由直流电流 I^* 给定的直流功耗 $P = V_{\mathrm{dd}}I^*$。在平衡点处，τ 是：

$$\tau = \frac{C}{G}, \quad (10)$$

其中 G 由方程 (3) 给出。每个样本的能量随之呈现为：

$$E = \frac{V_{\mathrm{dd}}C^2}{q_e}\mathrm{var}(V)\tanh\left(\frac{V_{\mathrm{dd}}}{4V_T}\right), \quad (11)$$

其中 $\mathrm{var}(V)$ 如方程 (9) 所示。

方程 (9) 和 (10) 阐明了我们系统的一个极具实用价值的特性：我们的电路产生的噪声的**时间尺度和方差是独立可控的**。通过在相对于 V_{dd} 处适当操纵栅极控制电压，可以使 τ 变得任意大或任意小（在实际限度内）。相比之下，方差仅取决于电源电压。从方程 (11) 中，我们可以看到，**每个样本消耗的能量并不取决于** τ，并且与所需的方差呈线性比例关系（在 $V_{\mathrm{dd}} \gg V_T$ 的极限下）。

【右栏】 (Right Column)

将先前拟合中发现的参数与方程 (10) 和 (11) 一起使用，可以发现 NEAT-RNs 可以作为概率计算系统中的高性能熵源。换句话说，取 $C \approx 1000$ aF，$I_0^p \approx 1$ nA，同时 $\Delta V = 5.5V_T$，我们计算得出 $E \approx 15$ aJ。在同一场景下，当 $V_p = 0$ 时将能实现 τ 的实际最小值，此时 $\tau \approx 1$ ns。

六、 总结与致谢

总而言之，我们已经证明，利用亚阈值晶体管网络可以构建出**可预测、可编程且高性能的 p 电路**。这些亚阈值网络现在可以很容易地与其他电路进行集成，从而使用先进的晶体管工艺来构建概率计算机。我们已经在文献 [29] 中提出了这样一种架构，并希望在未来的文章中报告它的具体实现。

此外，我们的结果也激励着人们对**概率集成电路设计**进行更深入的探索。这一蓬勃发展的模拟设计子领域大部分尚未被开拓，为创造新型、实用的电路拓扑和科学发现提供了一个肥沃的土壤。这些发现可以包括基于文献 [27] 的研究而取得的其它理论进展，或者是用于验证这些理论的进一步实验工作。

致谢 (ACKNOWLEDGMENTS)

T.M. 特此感谢艾萨克·庄（Isaac Chuang）对实验设计和手稿撰写提出的宝贵建议。

数据可用性 (DATA AVAILABILITY)

支持本文研究结果的数据是公开可用的 [51]。

七、 附件细节及理论支撑

（一） 附录 A：器件的制造、控制和测量 (APPENDIX A)

本工作中进行的实验利用了一个专门设计用来详细表征包含噪声的亚阈值电路的测试芯片。我们的芯片包含具有 $[0, 0.175\ \mathrm{V}]$ 动态范围的 8 位 DAC（数模转换器），用于操纵控制电压。每个实验中的输出信号皆使用高带宽和高输入阻抗的放大器（这些放大器也在同一裸片 (die) 上实现）来进行测量。这个放大链允许将模拟信号在芯片外进行布线，以便使用 $1\text{-}\mathrm{GHz}$ 示波器进行测量。

（二） 附录 B：散粒噪声模型及其扩散极限 (APPENDIX B)

我们考虑文献 [27] 中开发的非线性电子电路的随机描述，其中电路中的每个传导器件都表现出散粒噪声。电路的状态由自由节点（即非那些……）中的净基本电荷数来描述。

【左栏】 (Left Column)

……受电压源调节的节点），由一个向量 $n \in \mathbb{N}^d$ 给出，其中 d 是自由节点的数量。成对的自由节点可以通过由整数索引 $\rho > 0$ 标识的传导器件（二极管、隧道结、晶体管等）相连接。如果一个传导器件连接在两个自由节点之间，那么基本电荷可以在它们之间双向跳跃。对于每个器件 ρ，我们为正向传导事件 $n \to n + \Delta_\rho$ 分配一个跃迁速率（transition rate） $\lambda_{+\rho}(n)$，并为反向传导事件 $n \to n + \Delta_{-\rho}$ 分配一个跃迁速率 $\lambda_{-\rho}(n)$，其中 $\Delta_\rho = -\Delta_{-\rho}$。正向方向是任意设定的，而向量 Δ_ρ 编码了对应于每次跳跃或跃迁的状态 n 的变化。

对于任何状态 n，自由节点的电压均可计算为 $v = q_e C^{-1} n + v_r$，其中 C 是自由节点的麦克斯韦电容矩阵，q_e 是基本电荷的电量，而 v_r 是取决于受调节电压的常数向量。设 $P_t(v)$ 为在时间 t 观察到电压 v 的概率。鉴于先前的描述，$P_t(v)$ 的演化遵循 **主方程 (master equation)**：

$$\partial_t P_t(v) = \sum_\rho \lambda_\rho(v - q_e C^{-1}\Delta_\rho) P_t(v - q_e C^{-1}\Delta_\rho) - \sum_\rho \lambda_\rho(v) P_t(v), \quad (B1)$$

此处为了书写方便，我们滥用了记号，将速率 $\lambda_\rho(v)$ 视为了电压 v 的函数。该马尔可夫跳跃过程的 **扩散逼近 (diffusive approximation)** 可以通过对方程 (B1) 的克拉默斯-莫亚尔展开（Kramers-Moyal expansion）进行二阶截断来获得，这对应于大电容极限 $||C|| \gg C_T$。在这种情况下，方程 (B1) 简化为福克-普朗克方程（Fokker-Planck equation），这意味着系统的动力学可以由以下形式的 **伊藤随机微分方程 (SDE)** 来近似描述：

$$C \cdot dv = \mu(v) dt + \sqrt{2K(v)} \cdot dW, \quad (B2)$$

其中 W 是独立维纳过程（Wiener processes）的向量。该逼近是无量纲控制的，且无法捕捉大的涨落 [52,53]，但在大电容极限下能妥善描述 $P_t(v)$ 的一阶矩和二阶矩 [54]。漂移向量（drift vector） $\mu(v)$ 和扩散矩阵（diffusion matrix） $K(v)$ 可以从跃迁速率 $\lambda_\rho(v)$ 中获得。相应地，与传导器件 ρ 相关的两个跃迁速率 $\lambda_{\pm\rho}(v)$ 能够通过 **热力学一致性关系** [27] 与其唯象伏安（I-V）曲线 $I_\rho(\Delta v)$ 关联起来：

$$\lambda_{+\rho}(v) - \lambda_{-\rho}(v) = I_\rho(\Delta v_\rho)/q_e, \quad (B3)$$

$$\lambda_{+\rho}(v) + \lambda_{-\rho}(v) = \coth\left(\Delta v_\rho / 2V_T\right) I_\rho(\Delta v_\rho)/q_e.$$

【右栏】 (Right Column)

利用方程 (B3)，可以获得漂移向量 $\mu(v)$ 和扩散矩阵 $K(v)$ 的以下表达式：

$$\mu(v) \equiv \sum_\rho I_\rho(\Delta v_\rho)\Delta_\rho,$$

$$K(v) \equiv \frac{q_e}{2} \sum_\rho I_\rho(\Delta v_\rho) \coth\left(\Delta v_\rho / 2V_T\right) \Delta_\rho \cdot \Delta_\rho^T, \quad (B4)$$

其中 Δv_ρ 是器件 ρ 在状态 v 下的电压降。

对于具有确定性固定点吸引子 v^* 的电路，即满足 $\mu(v^*)=0$ 的电路，方程 (B2) 中的随机动力学可以被 **线性化** 为：

$$C\cdot dv=-G\cdot(v-v^*)dt+\sqrt{2k_bG\mathcal{T}}\cdot dW,\quad (B5)$$

其中我们定义了有效电导矩阵 G（元素为 $G_{jk}\equiv-\partial_{v_k}\mu_j(v^*)$）以及有效温度矩阵 $\mathcal{T}\equiv G^{-1}K(v^*)/k_b$。上述动力学的稳态分布由正文中的方程 (1) 和 (2) 给出。

最后，我们注意到对于一维情形，方程 (B5) 的线性化动力学具有以下 **稳态自相关函数**：

$$\mathbb{X}(\delta t)=\frac{k_b\mathcal{T}}{C}e^{-(G/C)|\delta t|},\quad (B6)$$

这导向了以下 **洛伦兹（Lorentzian）单边功率谱密度（PSD）**：

$$P(f)=\frac{P_0}{1+(f/f_0)^2},\quad (B7)$$

其中 $P_0=4k_b\mathcal{T}/G$，同时 $f_0=G/(2\pi C)$。

（三） 附录 C：基于 EKV 的反相器模型 (APPENDIX C)

我们现在考虑一个单独的反相器 [如图 1(a) 所示的左侧或右侧一对晶体管]。根据包含漏极引发势垒降低（DIBL）效应的 EKV 模型的扩展（如文献 [55] 所示），流过 NMOS 晶体管的电流由以下公式给出：

$$I_n=I_0^n\log^2\left(1+e^{(V_{gb}-V_{th}^n)/2n_n}e^{-V_{sb}/2}e^{\gamma_nV_{ds}/2}\right)-I_0^n\log^2\left(1+e^{(V_{gb}-V_{th}^n)/2n_n}e^{-V_{db}/2}e^{-\gamma_nV_{ds}/2}\right),\quad (C1)$$

其中 I_0^n、V_{th}^n、n_n 和 γ_n 是模型参数，在此电压 $V_{gb}=V_n$、$V_{sb}=0$、$V_{db}=V_{ds}=v$ 均以热电压 V_T 为单位进行表示。相同的表达式也给出了流过 PMOS 晶体管的电流 I_p，这次是对应参数 I_0^p、V_{th}^p、n_p 以及 γ_p，只需将 $I_p\to-I_n$ 进行替换，并使用电压 $V_{gb}=-(V_p-V_{\rm dd})$、$V_{sb}=0$、$V_{db}=V_{ds}=-(v-V_{\rm dd})$。

【左栏】 (Left Column)

为了在解析上取得进展，采用若干近似是有用的。尤其是，我们考虑满足 $e^{(V_{gb}-V_T)/2n_{n/p}}\ll1$ 的亚阈值状态，并忽略 DIBL 效应（即设定 $\gamma_n=\gamma_p=0$）。那么，电流 I_n 和 I_p 就化简为以下关于输出节点电压 v 的函数：

$$I_p(v)=\underbrace{I_0^pe^{-(V_p-V_{\rm dd})/n_p}}_{c_p}(1-e^{v-V_{\rm dd}}),$$

$$I_n(v)=\underbrace{I_0^ne^{V_n/n_n}}_{c_n}(1-e^{-v}),\quad (C2)$$

其中我们现在将因子 $e^{-V_{th}^{n/p}/n_{n/p}}$ 整合到了各自的常数 $I_0^{n/p}$ 之中。确定性输出电压 v^* 满足 $I_p(v^*)=I_n(v^*)$，在上述近似下，可以导出表达式：

$$e^{v^*}=\frac{e^{V_{\rm dd}}}{2}\left[\left(1-\frac{c_n}{c_p}\right)+\sqrt{\left(1-\frac{c_n}{c_p}\right)^2+4\frac{c_n}{c_p}e^{-V_{\rm dd}}}\right].\quad (C3)$$

使用该公式，我们得出 **有效电导** 由以下公式给出：

$$G=V_T^{-1}\sqrt{(c_p-c_n)^2+4c_pc_ne^{-V_{\rm dd}}}.\quad (C4)$$

此外，**有效温度** 由以下公式给出：

$$k_b\mathcal{T}=\frac{q_eI^*}{2G}\left[\coth((V_{\rm dd}-v^*)/2)+\coth(v^*/2)\right],\quad (C5)$$

其中 $I^*\equiv(c_p+c_n-V_TG)/2$ 为稳态电流。当 $c_n=c_p$ 时，即可达到正文中考虑的平衡条件。正文中的表达式还假设所有晶体管的亚阈值斜率（subthreshold slopes）均为 1（即对所有反相器有 $n_{n/p}=1$）。

（四） 附录 D：频谱分析 (APPENDIX D)

图 3(a) 展示了在不同工作电压下，从时间序列中数值计算得到的信号 v_1 的功率谱密度（PSD）。每个 PSD 上方的黑色虚线展示了使用以下模型对其进行拟合的结果：

$$P(f) = \frac{P_0}{1 + (f/f_0)^2} + \frac{L}{f^\alpha} + B. \quad (D1)$$

第一项对应于 **洛伦兹光谱**，这在之前的小节中已经由理论作出了预期。第二项旨在捕捉低频下占主导地位的 **粉红噪声（pink noise）**，而最后一项则考虑了可能与外部噪声源（例如放大级）相关的平坦频谱贡献。 *(接右栏)*

【右栏】 (Right Column)

> **插图/图注：--

正文文本

这种分解允许将信号的总功率或方差拆分成不同的贡献项，如图 3(b) 所示。

最后，我们注意到，可以通过参数 P_0 和 f_0 计算出**有效温度**为 $k_b\mathcal{T} = Cf_0P_0\pi/2$，其中 C 是所讨论反相器的总输出电容 [例如，对于左侧反相器，若用自电容 $C_{1/2}$ 和互电容 C_m 表示，则为 $C = C_1 + 1/(1/C_2 + 1/C_m)$]。

**

（五） 附录 E：数据分析与模型拟合 (APPENDIX E)

将实验数据与理论模型进行对比分为 **三个阶段**：

1. 确定每个单独反相器的固有参数。
2. 对 $1/f$ 噪声源进行有效建模。
3. 基于观察到的相关性确定全局电容矩阵。
   原始时间序列和用于分析的代码可以在文献 [51] 中找到。

在**第一阶段**，对于每个反相器，我们基于方程 (B4)、(B5) 和 (C1) 同时拟合平均输出电压 $\langle v \rangle$、频率 f_0 以及有效温度 $k_b\mathcal{T}$。结果在接下来的内容（通常是图 4）中展示。图板（Panels）(a) 和 (b) 显示，基于方程 (C1) 的模型能够很好地捕捉系统的动力学，而图板 (c) 则是……

【左栏】 (Left Column)

> **插图/图注：--

正文文本

……图 4(c) 的结果表明，导致方程 (B4) 中 $K(v)$ 的 **散粒噪声建模假设**（shot-noise modeling assumption）能够很好地描述所采用工作电压下的 **固有热涨落**。

在**第二阶段**，我们的目标是描述 **低频粉红噪声（pink-noise）方差** 的变异性 [见图 3(b)]，它是信号总方差中的第二大贡献。MOS 晶体管中的低频噪声通常被建模为门极氧化物中存在的涨落电荷陷阱引起的 **阈值电压 V_{th} 的随机涨落**，这些陷阱共同产生了一个类似于 $1/f$ 的频谱 [33–37]。基于方程 (C1) 对每个反相器的直流（dc）模型进行 **小信号分析**，提供了一种在理解 V_{th} 涨落如何映射到测量输出方面的简单方法。为此，我们只需要考虑增益 $g_{n/p} = |\partial v^* / \partial V_{th}^{n/p}|$，它指示了确定性输出电压 v^* 随两种阈值电压各自的微弱扰动如何变化。利用在前一阶段拟合的参数，可以很容易地从模型中计算出这些增益 [见图 5(a)]。接着，如果在对应于总观察窗口和采样率的频率范围内，阈值电压 $V_{th}^{n/p}$ 的涨落总功率为 $S_{n/p}$，那么…… *(接右栏)*

**

【右栏】 (Right Column)

> **插图/图注：--

正文文本

……同一频率范围内输出信号的低频涨落则由以下公式给出：

$$S_{1/f} = g_n^2 S_n + g_p^2 S_p + S_0, \quad (E1)$$

其中 S_0 计入了 **外部低频噪声源**，且假设所涉及的三个噪声源相互独立。图 5 比较了作为工作点函数的由低频噪声引起的总方差，以及使用方程 (E1) 模型的拟合结果。我们看到，尽管该方法十分简单，但却可以解释大部分的变异性。

在**最后一个阶段**，我们将通过求解正文中的方程 (2) 获得的协方差矩阵，与在不同工作点下实验观察到的协方差矩阵进行比较，从而得以 **估计反相器输出的自电容和互电容**。

具体操作如下：我们使用在第一阶段获得的模型参数，计算每个工作点下分属每个反相器的电导 G 和有效温度 $\mathcal{T}$。然后，给定一张由建议的 C_1、C_2 和 C_m 值构建的电容矩阵 C，我们求解方程 (2) 中的 **李雅普诺夫方程**，以获得预期的协方差矩阵 Σ。该协方差矩阵将与从实验数据估计出的协方差矩阵进行对比。实验估计协方差矩阵的对角元素为方差的洛伦兹分量，观察到的相关性 $\mathbb{X}_{1,2}(\delta t = 0)$ 则为……

**

【左栏】 (Left Column)

> **插图/图注：--

正文文本

……（实验估计协方差矩阵的非对角元素则是）观察到的相关性 $\mathbb{X}_{1,2}(\delta t = 0)$。该过程的结果如图 6 所示。

最后，正文中的图 1(d) 和 1(e) 展示了原始时间序列（即包含所有噪声贡献）的协方差矩阵的长宽比（aspect ratio）和夹角（angle）。相同图表中的虚线是通过考虑协方差矩阵 $\Sigma_T = \Sigma_{\mathrm{L}} + \Sigma_{1/f}$ 从拟合模型中计算得出的，其中 Σ_{L} 是通过求解方程 (2) 中的李雅普诺夫方程获得的，而 $\Sigma_{1/f}$ 是一个对角矩阵，其元素 $S_{1/f,1}$ 和 $S_{1/f,2}$ 则根据方程 (E1) 计算得出。

**

（六） 附录 F：环流系数 (APPENDIX F: GYRATION COEFFICIENT)

我们现在简述用于延迟相关的方程 (7) 的推导过程。我们首先注意到，在稳态条件下，延迟相关 $\mathbb{X}_{j,k}(\delta t)$ 可以写为：

$$\mathbb{X}_{j,k}(\delta t) = \int dv \int dv' (v'_k - v^*_k)(v_j - v^*_j) P(v', t+\delta t | v, t) P(v)$$

$$= \int dv (v_j - v^*_j) \left[e^{-\delta t C^{-1} G} \cdot (v - v^*) \right]_k P(v)$$

$$= \left[e^{-\delta t C^{-1} G} \Sigma \right]_{k,j} = \left[\Sigma\, e^{-\delta t G C^{-1}} \right]_{j,k}, \quad (F1)$$

其中我们利用了如下事实：对于方程 (B5) 中的线性过程，条件概率 $P(v', t+\delta t | v, t)$ 是一个具有以指数形式弛豫的平均值 $\langle v' \rangle = v^* + e^{-\delta t C^{-1} G} \cdot (v - v^*)$ 的高斯分布，并且稳态…… *(接右栏)*

【右栏】 (Right Column)

……并且稳态分布 $P(v)$ 由方程 (1) 给出。

只要对任意可逆矩阵 A 使用积分公式 $\int_0^{t_I} dt e^{-tA} = A^{-1}(1 - e^{-t_I A})$（此处 t 或为积分延迟变量），即可推导出方程 (7)。

八、 参考文献

(注：为保证准确，保留原作者及期刊名，括号内翻译论文标题)

- **[1]** R. Dennard, F. Gaensslen, H.-N. Yu, V. Rideout, E. Bassous, and A. LeBlanc, **Design of ion-implanted MOSFET’s with very small physical dimensions** (具有极小物理尺寸的离子注入 MOSFET 的设计), IEEE J. Solid-State Circuits **9**, 256 (1974).
- **[2]** H. Nyquist, **Thermal agitation of electric charge in conductors** (导体中电荷的热搅动), Phys. Rev. **32**, 110 (1928).
- **[3]** L. B. Kish, **End of Moore’s law: Thermal (noise) death of integration in micro and nano electronics** (摩尔定律的终结：微电子与纳米电子集成的热（噪声）散逸/死亡), Phys. Lett. A **305**, 144 (2002).

- **[4]** E. Rezaei, M. Donato, W. R. Patterson, A. Zaslavsky, and R. I. Bahar, **Fundamental thermal limits on data retention in low-voltage CMOS latches and SRAM** (低压 CMOS 锁存器和 SRAM 数据保持的根本热力学极限), IEEE Trans. Device Mater. Rel. **20**, 488 (2020).
- **[5]** B. R. Zink, Y. Lv, and J.-P. Wang, **Review of magnetic tunnel junctions for stochastic computing** (用于随机计算的磁性隧道结综述), IEEE J. Explor. Solid-State Comput. Devices Circuits **8**, 173 (2022).
- **[6]** S. Chowdhury, A. Grimaldi, N. A. Aadit, S. Niazi, M. Mohseni, S. Kanai, H. Ohno, S. Fukami, L. Theogarajan, G. Finocchio *et al.*, **A full-stack view of probabilistic computing with p-bits: Devices, architectures, and algorithms** (利用 p-bit 进行概率计算的全栈视角：器件、架构与算法), IEEE J. Explor. Solid-State Comput. Devices Circuits **9**, 1 (2023).
- **[7]** J. Kim, J.-K. Han, H.-Y. Maeng, J. Han, J. W. Jeon, Y. H. Jang, K. S. Woo, Y.-K. Choi, and C. S. Hwang, **Fully CMOS-based p-bits with a bistable resistor for probabilistic computing** (利用双稳态电阻实现的全 CMOS 概率计算 p-bit), Adv. Funct. Mater. **34**, 2307935 (2024).
- **[8]** I. Ahmed, P.-W. Chiu, W. Moy, and C. H. Kim, **A probabilistic compute fabric based on coupled ring oscillators for solving combinatorial optimization problems** (基于耦合环形振荡器的用于解决组合优化问题的概率计算构架), IEEE J. Solid-State Circuits **56**, 2870 (2021).
- **[9]** W. Lee, H. Kim, H. Jung, Y. Choi, J. Jeon, and C. Kim, **Correlation free large-scale probabilistic computing using a true-random chaotic oscillator p-bit** (使用真随机混沌振荡器 p-bit 的无相关大规模概率计算), Sci. Rep. **15**, 1 (2025).
- **[10]** J. Kim, S. S. Woo, and R. Sarpeshkar, **Fast and precise emulation of stochastic biochemical reaction networks with amplified thermal noise in silicon chips** (在硅芯片上利用放大的热噪声对随机生化反应网络进行快速而精确的仿真), IEEE Trans. Biomed. Circuits Syst. **12**, 379 (2018).
- **[11]** W. A. Borders, A. Z. Pervaiz, S. Fukami, K. Y. Camsari, H. Ohno, and S. Datta, **Integer factorization using stochastic magnetic tunnel junctions** (利用随机磁性隧道结实现整数因子分解), Nature **573**, 390 (2019).
- **[12]** N. S. Singh, K. Kobayashi, Q. Cao, K. Selcuk, T. Hu, S. Niazi, N. A. Aadit, S. Kanai, H. Ohno, S. Fukami *et al.*, **CMOS plus stochastic nanomagnets enabling heterogeneous computers for probabilistic inference and learning** (CMOS 结合随机纳米磁体使异构计算机能够进行概率推理和学习), Nat. Commun. **15**, 2685 (2024).
- **[13]** R. Faria, K. Y. Camsari, and S. Datta, **Low-barrier nanomagnets as p-bits for spin logic** (低势垒纳米磁体作为自旋逻辑的 p-bit), IEEE Magn. Lett. **8**, 1 (2017).
- **[14]** K. Y. Camsari, R. Faria, B. M. Sutton, and S. Datta, **Stochastic p-bits for invertible logic** (用于可逆逻辑的随机 p-bit), Phys. Rev. X **7**, 031014 (2017).
- **[15]** K. Y. Camsari, S. Salahuddin, and S. Datta, **Implementing p-bits with embedded MTJ** (利用嵌入式 MTJ 实现 p-bit), IEEE Electron. Device Lett. **38**, 1767 (2017).

(注：括号内为论文标题的中文参考翻译)

- **[16]** Y. Shao, C. Duffee, E. Raimondo, N. Davila, V. Lopez-Dominguez, J. A. Katine, G. Finocchio, and P. K. Amiri, **Probabilistic computing with voltage-controlled dynamics in magnetic tunnel junctions** (磁性隧道结中利用电压控制动力学进行概率计算), Nanotechnology **34**, 495203 (2023).
- **[17]** D. Vodenicarevic, N. Locatelli, A. Mizrahi, J. S. Friedman, A. F. Vincent, M. Romera, A. Fukushima, K. Yakushiji, H. Kubota, S. Yuasa *et al.*, **Low-energy truly random number generation with superparamagnetic tunnel junctions for unconventional computing** (利用超顺磁性隧道结为非传统计算生成低能耗真随机数), Phys. Rev. Appl. **8**, 054045 (2017).
- **[18]** K. Yang, Q. Dong, Z. Wang, Y.-C. Shih, Y.-D. Chih, J. Chang, D. Blaauw, and D. Sylvester, in *2018 IEEE Symposium on VLSI Circuits* (IEEE, Honolulu, HI, USA, 2018), pp. 171–172.
- **[19]** D. Edelstein, M. Rizzolo, D. Sil, A. Dutta, J. DeBrosse, M. Wordeman, A. Arceo, I. Chu, J. Demarest, E. R. Edwards *et al.*, in *2020 IEEE International Electron Devices Meeting (IEDM)* (IEEE, San Francisco, CA, USA, 2020), pp. 11.5.1–11.5.4.
- **[20]** J. Daniel, Z. Sun, X. Zhang, Y. Tan, N. Dilley, Z. Chen, and J. Appenzeller, **Experimental demonstration of an on-chip p-bit core based on stochastic magnetic tunnel junctions and 2D MoS2 transistors** (基于随机磁性隧道结和二维 MoS2 晶体管的片上 p-bit 核心的实验展示), Nat. Commun. **15**, 4098 (2024).
- **[21]** J. Kaiser, W. A. Borders, K. Y. Camsari, S. Fukami, H. Ohno, and S. Datta, **Hardware-aware in situ learning based on stochastic magnetic tunnel junctions** (基于随机磁性隧道结的硬件感知原位学习), Phys. Rev. Appl. **17**, 014016 (2022).
- **[22]** P. Korkmaz, B. E. Akgul, K. V. Palem, and L. N. Chakrapani, **Advocating noise as an agent for ultra-low energy computing: Probabilistic complementary metal-oxide-semiconductor devices and their characteristics** (提倡噪声作为超低能耗计算媒介：概率互补金属氧化物半导体器件及其特性), Jpn. J. Appl. Phys. **45**, 3307 (2006).
- **[23]** K. Palem and A. Lingamneni, **Ten years of building broken chips: The physics and engineering of inexact computing** (打造“残缺”芯片的十年：不精确计算的物理学与工程学), ACM Trans. Embed. Comput. Syst. (TECS) **12**, 1 (2013).
- **[24]** J. Holleman, S. Bridges, B. P. Otis, and C. Diorio, **3 μW CMOS true random number generator with adaptive floating-gate offset cancellation** (带有自适应浮栅失调消除功能的 3 微瓦 CMOS 真随机数发生器), IEEE J. Solid-State Circuits **43**, 1324 (2008).
- **[25]** J. Bae, J. Koo, C. Shim, and B. Kim, in *2024 IEEE International Solid-State Circuits Conference (ISSCC)* (IEEE, San Francisco, CA, USA, 2024), Vol. 67, pp. 284–286.
- **[26]** R. Sarpeshkar, T. Delbruck, and C. A. Mead, **White noise in MOS transistors and resistors** (MOS 晶体管和电阻器中的白噪声), IEEE Circuits Devices Mag. **9**, 23 (1993).

- **[27]** N. Freitas, J.-C. Delvenne, and M. Esposito, **Stochastic thermodynamics of nonlinear electronic circuits: A realistic framework for computing around kT** (非线性电子电路的随机热力学：一个用于围绕 kT 进行计算的现实框架), Phys. Rev. X **11**, 031064 (2021).
- **[28]** E. Morifuji, T. Yoshida, M. Kanda, S. Matsuda, S. Yamada, and F. Matsuoka, **Supply and threshold-voltage trends for scaled logic and SRAM MOSFETs** (按比例缩小的逻辑和 SRAM MOSFET 的电源和阈值电压趋势), IEEE Trans. Electron. Devices **53**, 1427 (2006).
- **[29]** A. Jelinčič, O. Lockwood, A. Garlapati, G. Verdon, and T. Mccourt, **An efficient probabilistic hardware architecture for diffusion-like models** (用于扩散类模型的高效概率硬件架构), arXiv arXiv:2510.23972, Submitted to npj Unconventional Computing.
- **[30]** G. Reimbold and P. Gentil, **White noise of MOS transistors operating in weak inversion** (在弱反型区工作的 MOS 晶体管的白噪声), IEEE Trans. Electron Devices **29**, 1722 (1982).
- **[31]** S. Tedja, H. H. Williams, J. Van der Spiegel, F. M. Newcomer, and R. Van Berg, **Noise spectral density measurements of a radiation hardened CMOS process in the weak and moderate inversion** (在弱反型和中等反型区抗辐射 CMOS 工艺的噪声谱密度测量), IEEE Trans. Nucl. Sci. **39**, 804 (1992).
- **[32]** H. Tian, B. A. Fowler, and A. El Gamal, in *Sensors, Cameras, and Systems for Scientific/Industrial Applications* (SPIE, San Jose, CA, United States, 1999), Vol. 3649, pp. 177–185.
- **[33]** A. G. Mahmutoglu, A. Demir, and J. Roychowdhury, in *2013 IEEE/ACM International Conference on Computer-Aided Design (ICCAD)* (IEEE, San Jose, CA, United States, 2013), pp. 500–507.
- **[34]** B. Stampfer, A. Grill, and M. Waltl, in *Noise in Nanoscale Semiconductor Devices* (Springer, 2020), pp. 229–257.
- **[35]** H. Tian and A. El Gamal, **Analysis of $1/f$ noise in switched MOSFET circuits** (开关 MOSFET 电路中 1/f 噪声的分析), IEEE Trans. Circuits Syst. II: Analog Digit. Signal Process. **48**, 151 (2001).
- **[36]** C. Jakobson, I. Bloom, and Y. Nemirovsky, **$1/f$ noise in CMOS transistors for analog applications from subthreshold to saturation** (用于模拟应用的 CMOS 晶体管中从亚阈值到饱和区的 1/f 噪声), Solid State Electron. **42**, 1807 (1998).
- **[37]** M. Kirton and M. Uren, **Noise in solid-state microstructures: A new perspective on individual defects, interface states and low-frequency ($1/f$) noise** (固态微结构中的噪声：关于单个缺陷、界面态和低频 (1/f) 噪声的新视角), Adv. Phys. **38**, 367 (1989).
- **[38]** S. Ciliberto, A. Imparato, A. Naert, and M. Tanase, **Statistical properties of the energy exchanged between two heat baths coupled by thermal fluctuations** (通过热涨落耦合的两个热库之间热交换的统计特性), J. Stat. Mech. **2013**, P12014 (2013).
- **[39]** M. Baiesi, S. Ciliberto, G. Falasco, and C. Yolcu, **Thermal response of nonequilibrium RC circuits** (非平衡 RC 电路的温度/热响应), Phys. Rev. E **94**, 022144 (2016).
- **[40]** N. Freitas, J.-C. Delvenne, and M. Esposito, **Stochastic and quantum thermodynamics of driven RLC networks** (受驱 RLC 网络的随机与量子热力学), Phys. Rev. X **10**, 031005 (2020).
- **[41]** C. C. Enz and E. A. Vittoz, *Charge-Based MOS Transistor Modeling* (基于电荷的 MOS 晶体管建模) (John Wiley & Sons, Ltd, 2006).
- **[42]** T. Sekigawa and Y. Hayashi, **Calculated threshold-voltage characteristics of an XMOS transistor having an additional bottom gate** (带有额外底栅的 XMOS 晶体管的计算阈值电压特性), Solid-State Electron. **27**, 827 (1984).
- **[43]** S.-Y. Wu, C.-H. Chang, M. Chiang, C. Lin, J. Liaw, J. Cheng, J. Yeh, H. Chen, S. Chang, K. Lai *et al.*, in *2022 International Electron Devices Meeting (IEDM)* (IEEE, San Francisco, CA, USA, 2022) pp. 27.5.1–27.5.4.
- **[44]** J. Liu, S. Mukhopadhyay, A. Kundu, S. Chen, H. Wang, D. Huang, J. Lee, M. Wang, R. Lu, S. Lin, Y. Chen, H. Shang, P. Wang, H. Lin, G. Yeap, and J. He, in *2020 IEEE International Electron Devices Meeting (IEDM)* (IEEE, San Francisco, CA, USA, 2020), pp. 9.2.1–9.2.4.
- **[45]** N. Ohga, S. Ito, and A. Kolchinsky, **Thermodynamic bound on the asymmetry of cross-correlations** (互相关不对称性的热力学界限), Phys. Rev. Lett. **131**, 077101 (2023).
- **[46]** S. Liang and S. Pigolotti, **Thermodynamic bounds on time-reversal asymmetry** (时间反演不对称性的热力学界限), Phys. Rev. E **108**, L062101 (2023).
- **[47]** J. Gu, **Thermodynamic bounds on the asymmetry of cross-correlations with dynamical activity and entropy production** (带有动力学活性和熵产生的互相关不对称性的热力学界限), Phys. Rev. E **109**, L042101 (2024).

(注：括号内为论文标题的中文参考翻译)

- **[48]** R. Filliger and P. Reimann, **Brownian gyrator: A minimal heat engine on the nanoscale** (布朗回转器：纳米级的极小热机), Phys. Rev. Lett. **99**, 230602 (2007).
- **[49]** K.-H. Chiang, C.-L. Lee, P.-Y. Lai, and Y.-F. Chen, **Electrical autonomous Brownian gyrator** (电控自主布朗回转器), Phys. Rev. E **96**, 032123 (2017).
- **[50]** S. Arrhenius, **Über die Dissociationswärme und den Einfluss der Temperatur auf den Dissociationsgrad der Elektrolyte** (关于解离热以及温度对电解质解离度的影响), Z. Phys. Chem. **4**, 96 (1889).
- **[51]** Extropic Corp., Dataset for **“Taming non-equilibrium thermal fluctuations in subthreshold CMOS circuits”** (数据集：“在亚阈值 CMOS 电路中驯服非平衡热涨落”), Zenodo (2026), https://doi.org/10.5281/zenodo.18636981
- **[52]** P. Hanggi, H. Grabert, P. Talkner, and H. Thomas, **Bistable systems: Master equation versus Fokker-Planck modeling** (双稳态系统：主方程与福克-普朗克建模的对比), Phys. Rev. A **29**, 371 (1984).
- **[53]** D. Roberts, T. McCourt, G. Massarelli, J. Rothschild, and N. Freitas, **Improved diffusive approximation of Markov jump processes close to equilibrium** (接近平衡状态的马尔可夫跳跃过程的改进扩散逼近), Phys. Rev. Res. **8**, 013161 (2026).
- **[54]** A. Gopal, M. Esposito, and N. Freitas, **Large deviations theory for noisy nonlinear electronics: CMOS inverter as a case study** (噪声非线性电子学的大偏差理论：以 CMOS 反相器为例), Phys. Rev. B **106**, 155303 (2022).

- **[55]** A. Low and P. Hasler, in *42nd Midwest Symposium on Circuits and Systems (Cat. No. 99CH36356)* (第 42 届中西部电路与系统学术研讨会) (IEEE, Las Cruces, NM, USA, 1999), Vol. 1, pp. 141–144.

nature communications

Article

https://doi.org/10.1038/s41467-025-67958-0

Nonlinear thermodynamic computing out of equilibrium

Received: 24 February 2025

Accepted: 12 December 2025

Published online: 10 January 2026

Check for updates

Stephen Whitelam [1] & Corneel Casert [1,2]

We present the design for a thermodynamic computer that can perform arbitrary nonlinear calculations in or out of equilibrium. Simple thermodynamic circuits, fluctuating degrees of freedom in contact with a thermal bath and confined by a quartic potential, display an activity that is a nonlinear function of their input. Such circuits can therefore be regarded as thermodynamic neurons, and can serve as the building blocks of networked structures that act as thermodynamic neural networks, universal function approximators whose operation is powered by thermal fluctuations. We simulate a digital model of a thermodynamic neural network, and show that its parameters can be adjusted by genetic algorithm to perform nonlinear calculations at specified observation times, regardless of whether the system has attained thermal equilibrium. This work expands the field of thermodynamic computing beyond the regime of thermal equilibrium, enabling fully nonlinear computations, analogous to those performed by classical neural networks, at specified observation times.

In classical forms of computing, thermal fluctuations are an obstacle to computation[1–3]; for thermodynamic computing, thermal fluctuations are the means of doing computation[4–10]. Fluctuations can drive state changes in devices, and can be used to encode information. For instance, consider a thermodynamic computer comprising scalar degrees of freedom x_i that interact via the bilinear couplings $J_{ij}x_ix_j$. If this computer is placed in contact with a thermal bath at temperature T, then its equilibrium two-point correlations $\langle x_ix_j\rangle_0 = k_BT(J^{-1})_{ij}$ encode the elements of the matrix inverse of J. Thus measuring such correlations in equilibrium can be used to do matrix inversion[11,12].

The current focus of thermodynamic computing is to arrange for the equilibrium properties of a thermodynamic computer, described by the Boltzmann distribution, to correspond to the output of a specified computation. This approach is powerful because the potential energy of a thermodynamic computer specifies the Boltzmann distribution, and so by designing the potential we can design the computer's equilibrium properties[11]. However, this approach comes with two challenges. One is that we need the computer to attain thermal equilibrium. In general, physical systems equilibrate on a broad range of timescales[13–16], and the equilibration times for even a simple thermodynamic computer can vary by orders of magnitude as its program is altered[17]. A second challenge is that not every calculation can be represented by the Boltzmann distribution in an obvious way. For example, the matrix inversion described above can only be done if the matrix J_{ij} is positive definite; if not, the system does not possess a well-defined equilibrium distribution.

We can sidestep these challenges by arranging for a thermodynamic computer to perform calculations *out* of equilibrium. Out of equilibrium we lose contact with the theoretical foundation provided by the Boltzmann distribution, and so we must find other ways of programming a thermodynamic computer in order to do specified calculations. Some exceptions to the equilibrium paradigm already exist. For instance, the matrix exponential e^{-Jt} can be calculated at observation time t[18], and nonequilibrium work measurements can be used to calculate the determinant of a matrix[11]. However, no design exists for a thermodynamic computer that operates at specified observation times and is programmable in a general sense, meaning that it is capable of approximating arbitrary continuous functions. Here, we provide such a design by introducing a thermodynamic computer that is analogous to a neural network. A thermodynamic computer of this nature is a nonlinear model that can serve as a universal function approximator, and can be programmed to perform

[1]Molecular Foundry, Lawrence Berkeley National Laboratory, Berkeley, CA, USA. [2]NERSC, Lawrence Berkeley National Laboratory, Berkeley, CA, USA. e-mail: swhitelam@lbl.gov; ccasert@lbl.gov

arbitrary nonlinear computations at specified observation times. This is true whether or not the computer has attained thermodynamic equilibrium at those observation times.

The equilibrium thermodynamic computers of refs. 11,12, which motivate this work, can be viewed as continuous-spin analogs of Hopfield networks[19] or Boltzmann machines[20,21], statistical mechanical models that represent probability distributions over binary variables. Since a Boltzmann machine encodes information in its equilibrium or Boltzmann distribution, one could refer to the models of refs. 11,12 as *Boltzmann computers*: they are designed to sample from the Boltzmann equilibrium corresponding to the system's potential energy function. In such models, the specific form of the dynamics, whether overdamped or underdamped, is less important than the fact that it is microscopically reversible and converges to the desired equilibrium.

Our contribution is to explore the computational capabilities of such systems when extended to include nonlinear neuron potentials and operated out of equilibrium. Specifically, we encode the outcome of a computation in the dynamical trajectories of the system, without appealing to the Boltzmann distribution. A computer operating in this mode, using Langevin trajectories to perform a computation, could be termed a *Langevin computer*.

The theoretical framework describing thermodynamic computing includes nonequilibrium statistical mechanics, stochastic thermodynamics, and information theory. These fields offer a set of tools for analyzing small, fluctuating systems, such as fluctuation theorems, thermodynamic speed limits, and uncertainty relations[22–24]. For example, the Jarzynski equality, combined with nonequilibrium work measurements, can be used to compute the determinant of a matrix[11]. Thermodynamic computers often use added noise to accelerate computation, and the energetic cost of this addition can be quantified within stochastic thermodynamics[17]. Learning rules can be linked to thermodynamic quantities: for instance, a generative thermodynamic computer trained by gradient descent minimizes heat dissipation during training[25].

Results

Thermodynamic neurons

In more detail, we introduce the thermodynamic circuit shown in Fig. 1a, a fluctuating classical degree of freedom placed in contact with a heat bath and confined by a quartic potential. This circuit represents a scalar degree of freedom x that experiences the potential energy

$$U_{\boldsymbol{J}}(x, I) = J_2 x^2 + J_3 x^3 + J_4 x^4 - Ix. \tag{1}$$

The parameters $\boldsymbol{J} = (J_2, J_3, J_4)$ are the intrinsic couplings of the circuit, and I is an input signal. We can consider the circuit to represent a thermodynamic neuron, whose activation function is the relation between the output x and the input I. The output must be a nonlinear function of the input in order for a network built from such neurons to be a universal approximator. In general, the confining potential need not be exactly quartic, but it must be higher-order than quadratic and thermodynamically stable (i.e., bounded from below). We can consider Eq. (1) to represent a Maclaurin expansion, in powers of x, of an arbitrary nonlinear thermodynamic circuit.

Let the neuron be put in contact with a thermal bath at temperature T. In thermal equilibrium, the output of the neuron has the mean value

$$\langle x \rangle_0 \equiv \frac{\int \mathrm{d}x\, x\, \mathrm{e}^{-\beta U_{\boldsymbol{J}}(x,I)}}{\int \mathrm{d}x\, \mathrm{e}^{-\beta U_{\boldsymbol{J}}(x,I)}}. \tag{2}$$

When the neuron potential is purely quadratic, i.e., $\boldsymbol{J} = (J_2, 0, 0)$, the integrals in (2) can be solved analytically, giving the linear form $\langle x \rangle_0 = I/(2J_2)$. This form is plotted, for $J_2 = 1$, as a gray line in Fig. 1(b); the horizontal dotted black line denotes the value zero. In this case the equilibrium activation function of the neuron is linear, meaning that networks of such neurons in equilibrium cannot serve as universal function approximators[26,27]. The simplest case that is thermodynamically stable (i.e., the potential is bounded from below) and admits a nonlinear equilibrium activation function is the purely quartic case, $\boldsymbol{J} = (0, 0, J_4)$, with $J_4 > 0$. This case is shown as a blue line in Fig. 1b, with $J_4 = 1$ (in the purely quartic case, the equilibrium activation function can be expressed analytically, in terms of the hypergeometric function). The equilibrium activation function is nonlinear: its gradient (shown inset) is largest near the origin, and decreases as $|I|$ becomes large.

An additional design consideration is the variance $\sigma^2 = \langle x^2 \rangle_0 - \langle x \rangle_0^2$ of the neuron's equilibrium fluctuations. We show in the Supplementary Material that adding a quadratic term to the quartic term suppresses the neuron's fluctuations in equilibrium. The larger the fluctuations of a thermodynamic neuron's output, the more samples will be required to compute a meaningful signal when observing a computer built from such neurons. For these reasons, we choose our default neuron parameters to be $\boldsymbol{J} = (1, 0, 1)$: the quartic coupling induces nonlinearity, while the quadratic coupling serves to suppress fluctuations near $I = 0$.

The *nonequilibrium* response of the quartic-potential thermodynamic neuron is also, in general, nonlinear with input.

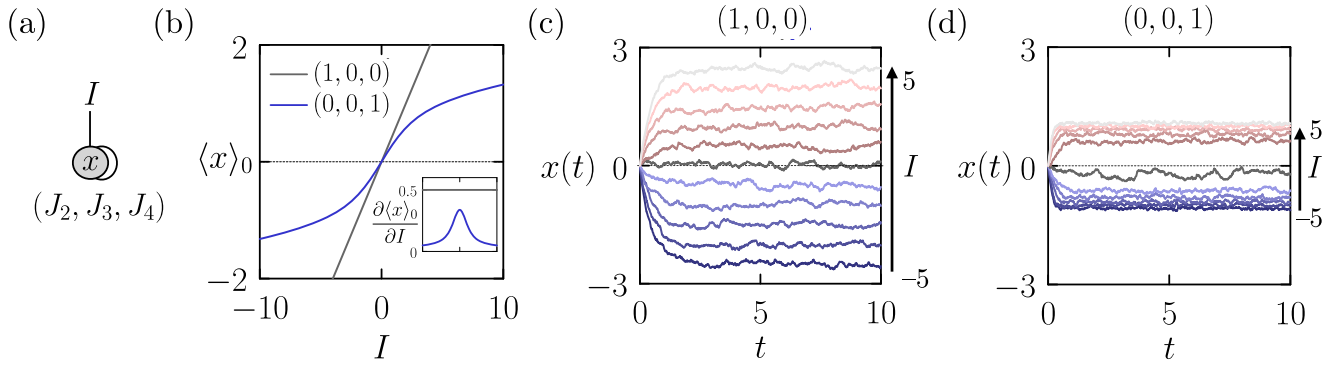

Fig. 1 | Thermodynamic neurons. a A thermodynamic circuit whose interaction energy is given by Eq. (1) can function as a thermodynamic neuron. The circle represents a scalar degree of freedom x. The curved line represents its intrinsic energy, the terms in $\boldsymbol{J} = (J_2, J_3, J_4)$ in Eq. (1). The straight line represent an input signal or bias, the term in I in Eq. (1). **b** Equilibrium activation function $\langle x \rangle_0$ of the neuron, Eq. (2), as a function of the neuron input I, for the case $\beta = 1$. The vector $\boldsymbol{J} = (J_2, J_3, J_4)$ sets the values of the intrinsic couplings of the neuron. The quadratic-potential activation function is linear, while the quartic-potential activation function is nonlinear. **c** Dynamical evolution (3) of the quadratic-potential neuron, for $\beta = 100$, for 11 evenly-spaced values of I. **d** The same for the quartic-potential neuron. For times longer than some short threshold, the finite-time response is a nonlinear function of I.

https://doi.org/10.1038/s41467-025-67958-0

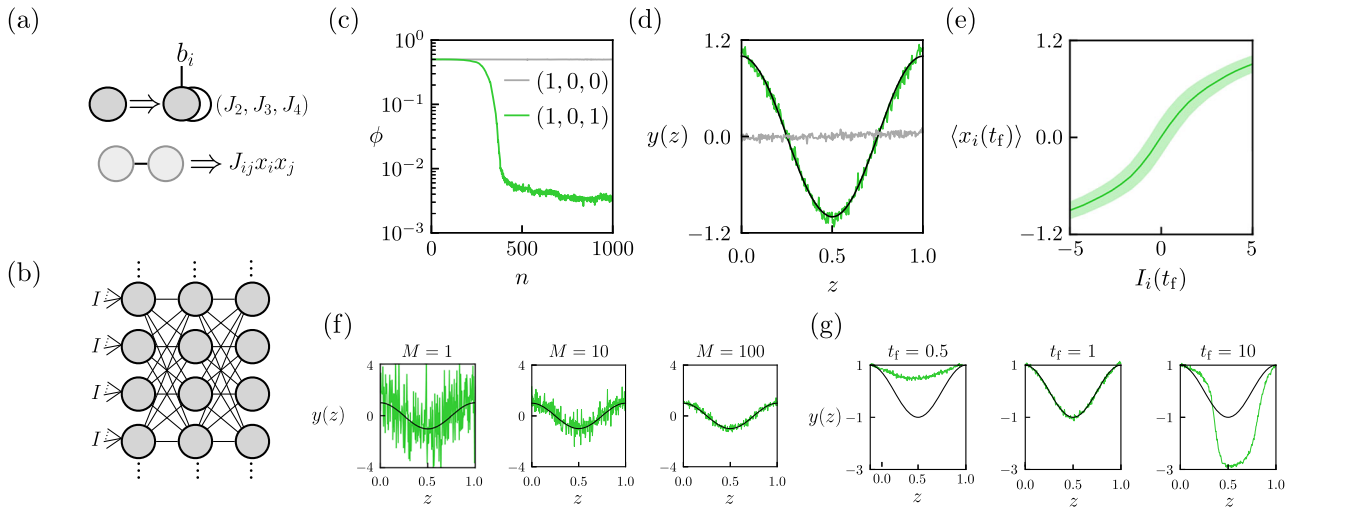

Fig. 2 | Elements of a thermodynamic computer analogous to a neural network. **a** The thermodynamic neurons described in Fig. 1 are connected by bilinear couplings. Top: a single circle implies a neuron x_i of the type described in Fig. 1, with an input (bias) $I = b_i$ and a nonlinear potential parameterized by $\boldsymbol{J} = (J_1, J_2, J_3)$. Bottom: lines between circles imply a bilinear coupling $J_{ij}x_ix_j$. **b** With the visual shorthand described in panel (**a**), we consider layered networks of such neurons, with adjacent layers coupled all-to-all, having total potential energy (4). **c** Training a simulation model of a thermodynamic computer to express a nonlinear function at a specified observation time. We show loss (8) as a function of evolutionary time n for a layered thermodynamic computer built from quadratic neurons (gray) or quadratic-quartic neurons (green). **d** Output (9) at observation time $t_f = 1$ of the linear computer (gray) and the nonlinear computer (green), as a function of the input z, averaged over $M = 10^3$ samples. The target function is shown as a black line. **e** Mean neuron activations measured at observation time t_f as a function of the neuron inputs at the same time, for the nonlinear model. The color band denotes ± one standard deviation. **f** Output (9) at time $t_f = 1$ of the trained nonlinear thermodynamic computer as a function of input z, computed using M samples. The target function is shown as a black line (training was done using $M = 10^3$ samples). **g** Output (9) at various observation times t_f of the trained nonlinear thermodynamic computer, as a function of input z, computed using $M = 10^3$ samples. The target function is shown as a black line. The computer is trained so that it reproduces the target function when observed at time $t_f = 1$.

Thermodynamic computers operate under Langevin dynamics[11,12], and here we consider the overdamped dynamics

$$\dot{x}_i = -\mu\frac{\partial V(\boldsymbol{x},\boldsymbol{I})}{\partial x_i} + \sqrt{2\mu k_B T}\,\eta_i(t), \tag{3}$$

where i labels the neuron; $V(\boldsymbol{x}, \boldsymbol{I})$ is the computer's potential given input $\boldsymbol{I}$; and the Gaussian white noise terms satisfy $\langle\eta_i(t)\rangle = 0$ and $\langle\eta_i(t)\eta_j(t')\rangle = \delta_{ij}\delta(t-t')$. The mobility parameter μ sets the basic time constant of the computer. For the thermodynamic computers of refs. 11,12, μ^{-1} ~ 1 microsecond. For damped oscillators made from mechanical elements[28] or Josephson junctions[29], μ^{-1} is of order a millisecond or a nanosecond, respectively.

In Fig. 1c, d, we show the dynamical evolution of a single neuron x in the potential $V(\boldsymbol{x}, \boldsymbol{I}) = U_{\boldsymbol{J}}(x, I)$, under the dynamics (3), starting from $x = 0$. Panel (c) shows the case of the quadratic potential $\boldsymbol{J} = (1, 0, 0)$, for various fixed values of the input I. The neuron is initially out of equilibrium, converging to equilibrium in about 2 time units (time is expressed in units of μ^{-1}). As described by Fig. 1b, the mean value of x in equilibrium is a linear function of I.

Panel (d) shows the case of a quartic potential $\boldsymbol{J} = (0, 0, 1)$. For observation times larger than some threshold, the neuron's output is a nonlinear function $x(I)$, and eventually converges to the equilibrium activation function $\langle x(I)\rangle_0$, which we have designed to be nonlinear. A network of such neurons, observed on similar timescales, can therefore function as a universal approximator. (In a related vein, nonlinear physical neural networks that operate on the energy scales of classical computing have recently been trained to do nonlinear computations[30].)

Thermodynamic neural network

To illustrate this statement, consider a thermodynamic computer consisting of a network of N thermodynamic neurons x_i, with potential energy function

$$V(\boldsymbol{x},\boldsymbol{I}) = \boldsymbol{V}_{\text{int}}(\boldsymbol{x}) + \boldsymbol{V}_{\text{ext}}(\boldsymbol{x},\boldsymbol{I}). \tag{4}$$

Here

$$V_{\text{int}}(\boldsymbol{x}) = \sum_{\boldsymbol{i=1}}^{\boldsymbol{N}} \boldsymbol{U_J}(\boldsymbol{x_i}, \boldsymbol{b_i}) + \sum_{\boldsymbol{\langle ij\rangle}} \boldsymbol{J_{ij}x_ix_j} \tag{5}$$

is the internal potential of the computer, accounting for neuron self-interactions and connections between neurons. The first sum in (5) runs over N single-neuron energy terms (1), while the second sum runs over all distinct pairs of connected neurons. We use the bilinear interaction of refs. 11,12. The computers described in those papers use an all-to-all coupling; here, to make contact with existing neural-network designs, we consider the layered structure shown in Fig. 2, with all-to-all connections between layers. This design mimics that of a conventional deep fully-connected neural network. However, unlike in a conventional deep neural network, in which information flows from the input layer to the output layer, the bilinear interaction $J_{ij}x_ix_j$ ensures that neuron i communicates with neuron j, and vice versa, and so information flows forward and backward between the layers of the thermodynamic computer.

To provide input to the thermodynamic computer, we introduce the external coupling

$$V_{\text{ext}}(\boldsymbol{x},\boldsymbol{I}) = \sum_{\text{inputs}(\boldsymbol{ij})} \boldsymbol{W_{ij}I_ix_j}, \tag{6}$$

where the sum runs over all connections between the external inputs I_i and the input neurons x_j (here the top-layer neurons), mediated by the parameters W_{ij}.

The computer evolves according to the Langevin dynamics (3). Because the computer is noisy, we wish to take M samples of its output

https://doi.org/10.1038/s41467-025-67958-0

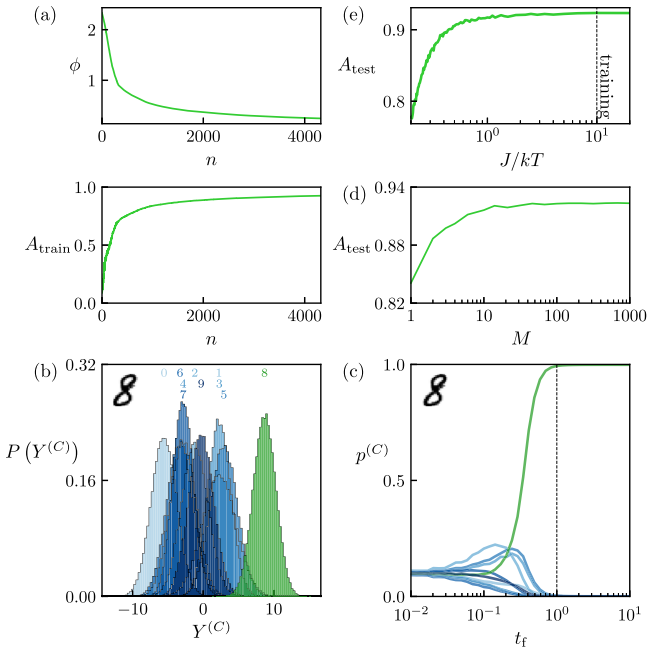

Fig. 3 | Machine learning with a simulated thermodynamic computer. The computer, which consists of a 3-layer network of quadratic-quartic (1, 0, 1) neurons, is trained to classify MNIST in reset-sampling mode, using $M = 10^3$ samples taken at observation time $t_f = 1$. **a** Loss (cross-entropy) and training-set classification accuracy as a function of evolutionary time n. **b** For a single digit, an 8, we show the probability distribution, taken over 10^5 samples, of the computer's per-sample class score. The mean value of each distribution, which is the value used for classification, is indicated at the top of the panel. The correct distribution is shown in green, the others in shades of blue. **c** The class probabilities of the computer, upon being shown the indicated digit, for various observation time t_f. The computer is trained to classify the digit at an observation time $t_f = 1$ (vertical dotted line). **d** Test-set classification accuracy of the trained computer, as a function of the number of samples M generated by the computer (each taken at observation time $t_f = 1$). **e** Test-set accuracy of the trained computer at a range of energy scales. The computer is trained at the energy scale $J = 10k_BT$.

and average over these samples. In the main text, we do this by reset-sampling: starting from zero neuron activation $\boldsymbol{x} = \boldsymbol{0}$, we run the computer for time t_f, observe the outcome, reset the neuron activations to zero, and repeat the procedure, gathering M samples in total (in the Supplementary Material we also consider the case of serial sampling). Reset sampling naturally lends itself to parallelization: the M samples can be computed independently, on distinct copies of the thermodynamic computer if such copies are available. Reset sampling can also be done using a single computer whose neurons are reset periodically.

We designate the final-layer neurons of the computer as its outputs, and calculate the reset-sampling averages

$$\langle x_i(\boldsymbol{I})\rangle_{\text{r}} = M^{-1}\sum_{\alpha=1}^{M} x_i^{(\alpha)}(\boldsymbol{I}, t_f), \tag{7}$$

where the subscript "r" indicates "reset-sampling", and the sum runs over M independent trajectories α of the dynamics (3). The only requirement on t_f is that it is long enough that the effective activation function of the neuron is nonlinear. We set $t_f = 1$, in units of μ^{-1}.

Programming a thermodynamic computer

A nonlinear thermodynamic computer can be programmed to perform arbitrary nonlinear computations at specified times. We first consider the task of expressing a nonlinear function of a single variable. In this case, the computer has one input, $I = z$. We define the target function $y_0(z) \equiv \cos(2\pi z)$, and the loss function

$$\phi \equiv K^{-1}\sum_{j=1}^{K}\left(y_0(z_j) - y(z_j)\right)^2, \tag{8}$$

where the sum runs over $K = 250$ evenly-spaced points $z_j = j/(K-1)$ on the interval $z \in [0, 1]$. The quantity

$$y(z) \equiv \sum_{i\in\text{outputs}} f_i\langle x_i(z)\rangle_{\text{r,s}} \tag{9}$$

is the output of the thermodynamic computer, given the input z, averaged over $M = 10^3$ samples. The subscript "r,s" indicates that averages are taken either in reset-sampling or in serial-sampling mode. If the former, each of the M samples is obtained from an independent trajectory. If the latter, all M samples are obtained from a single trajectory.

The adjustable parameters of the computer are $\boldsymbol{\theta} = \{W_{ij}\} \cup \{b_i\} \cup \{J_{ij}\} \cup \{f_i\}$. Here $\{W_{ij}\}$ is the set of input weights specified by Eq. (6); $\{b_i\}$ is the set of biases specified by Eq. (5); $\{J_{ij}\}$ is the set of connections specified by the same equation; and $\{f_i\}$ is a set of weights that couple to the output neurons. To program the computer we adjust the parameters $\boldsymbol{\theta}$ using a genetic algorithm instructed to minimize a loss function ϕ, using an efficient GPU implementation (see Supplementary Material).

Following training, the identity of the computer's parameters is fixed, and the computer can be run for any chosen input. The parameters of the digital model of the thermodynamic computer could, in principle, be implemented in hardware, resulting in a device designed to output a specified computation at a specified time, powered by thermal fluctuations. We note that if the hardware implementation is not an exact copy of the digital model, the genetic-algorithm training could be continued directly in hardware: the training procedure can be applied to an experimental system exactly as it is applied to a simulation model[31].

We choose a layered computer design of width 8 and depth 4. We consider two types of thermodynamic neuron: a quadratic-quartic thermodynamic neuron, $\boldsymbol{J} = (1, 0, 1)$, which gives rise to a nonlinear computer, and a quadratic thermodynamic neuron, $\boldsymbol{J} = (1, 0, 0)$, which gives rise to a linear computer. We take $\beta = 10$, so that the neuron energy scale is 10 times that of the thermal energy.

In Fig. 2c, we show the loss as a function of evolutionary time for the two models. The linear model fails to train—it cannot express a nonlinear function of the input variable—while the nonlinear model learns steadily, reaching a small value of the loss. Panel (d) shows the output functions learned by the two models: the nonlinear model has learned a good approximation of the target cosine function. The intrinsic noise of the computer is visible in the output, but for $M = 10^3$ samples, for each value of z, the mean output signal of the computer exceeds the scale of the noise by a considerable margin.

Panel (e) of Fig. 2 shows the sampled neuron outputs as a function of the neuron inputs (the inputs being all signals into the neuron, excepting the thermal noise) at the designated observation time. The nonlinear model possesses a nonlinear finite-time activation function, explaining the computer's ability to learn an arbitrary nonlinear function. By contrast, the quadratic-neuron computer is at all times a linear model and is unable to express a nonlinear function.

Training is done using $M = 10^3$ samples for each value of the input z, but the trained computer can be used with fewer samples if desired. In Fig. 2f, we show the output of the trained thermodynamic computer, as a function of the input z, for a range of values of M.

Training in reset-sampling mode results in a thermodynamic computer programmed to express the target function at a prescribed observation time $t_f = 1$. In Fig. 2g, we show the output of the computer at a range of observation times. The output of the computer varies as a

function of time and is equal to the target function only at the prescribed observation time. The output of the computer in equilibrium (corresponding to the long-time limit) is considerably different to the target function. In this example, therefore, the programmed thermodynamic computer operates far from equilibrium.

Machine learning with a thermodynamic computer

Having confirmed the ability of a network of nonlinear thermodynamic neurons to express an arbitrary nonlinear function, we now consider a standard benchmark in machine learning, classifying the MNIST data set[32]. MNIST consists of greyscale images of 70,000 handwritten digits on a grid of 28 × 28 pixels, each digit belonging to one of ten classes $C \in [0, 9]$.

We simulate a 3-layer thermodynamic computer with quadratic-quartic (1, 0, 1) neurons. Each layer has 32 neurons. Each neuron in the input layer couples to all the pixels I_i of an MNIST digit via Eq. (6). The output layer of 32 neurons is used to construct the computer's prediction for the class of MNIST digit $\boldsymbol{I}_j$, and we train the computer by genetic algorithm, instructing it to minimize the cross-entropy between the class probabilities predicted by the thermodynamic computer and the ground-truth labels (see Supplementary Material).

In Fig. 3a we show the loss as a function of evolutionary time n as the computer is trained to classify MNIST. The computer learns steadily under the action of the genetic algorithm. Panel (b) shows the corresponding training-set classification accuracy (which can be observed but is not used during training). The corresponding test-set accuracy after training is about 93%, which is not state-of-the-art—many other methods classify MNIST with greater accuracy[33]—but it is more accurate than a linear classifier, and confirms the ability of a thermodynamic computer to address standard machine-learning problems. As with conventional neural networks, better accuracy will be achieved using different computer designs and methods of training. Here, our aim is to show proof of principle: if implemented in hardware, this thermodynamic computer would be able, powered only by thermal fluctuations, to classify MNIST digits.

In Fig. 3b, we show the output of the trained computer when presented with a single digit, an 8, which it correctly classifies. We distinguish between the class *score* $Y^{(C)}$, the raw output of the thermodynamic computer prior to normalization, and the class probability $p^{(C)}$, which results from applying a softmax transformation to averaged score. We use the term *class prediction* to refer to the class with the highest score, i.e., the computer's predicted label for the digit. We plot the probability distribution, taken over 10^5 samples, of the computer's class score $Y^{(C)}$ for the digit. The mean value of each distribution (the value used for classification) is indicated at the top of the panel. The correct distribution is shown in green, with the others in shades of blue. In panel (c), we plot the value of the trained computer's 10 class probabilities upon being shown the indicated digit. The computer is trained to classify the digit at an observation time $t_f = 1$. In this case, the computer has attained a steady-state dynamics at the specified observation time, but this is not a general phenomenon: when presented with other digits, the computer's neurons are still evolving at $t_f = 1$, and so in general the computer operates out of equilibrium. Fig. 3d shows the test-set accuracy of the computer upon collecting M samples. Training was done with $M = 10^3$ samples, but similar accuracy can be obtained using only about 20 samples. Thus, if implemented in hardware, the thermodynamic computer could perform classification relatively efficiently.

The ability of a trained computer to operate at different noise scales depends on the nature of the problem it is trained for and its architecture. In Fig. 3e, we show the test-set accuracy of the trained thermodynamic computer at a range of energy scales, calculated by holding fixed the parameters of the thermodynamic computer and varying the noise strength (see Supplementary Material). The computer, trained at the energy scale $J = 10k_BT$, performs essentially as well when subjected to noise comparable to its own energy scale ($J = k_BT$). This result shows the ability of the computer to operate reliably throughout the regime characteristic of thermodynamic computing ($k_BT \lesssim J \ll 10^3 k_BT$), and shows its output to be robust to small changes in noise level (which might occur if a device becomes hot during computation). For sufficiently large noise levels, the computer's performance begins to decline.

Discussion

Classical computing aims to suppress thermal fluctuations, while thermodynamic computing uses them. Most existing thermodynamic computers focus on doing linear algebra in equilibrium, using the Boltzmann distribution to encode computations[11,12]. A thermodynamic computer used in this way could be described as a *Boltzmann computer*. However, equilibration can be slow, and not all problems can be encoded as a Boltzmann distribution. This paper presents an alternative approach, in which a nonlinear thermodynamic computer is trained to perform nonlinear calculations at specified times. A thermodynamic computer trained to perform computations using Langevin trajectories could be called a *Langevin computer*.

The core component of the design, a thermodynamic neuron, is a fluctuating degree of freedom confined by a non-quadratic potential, allowing networks of such neurons to act as universal approximators. A recent paper[34] presented the design for a thermodynamic neuron realized by qubits coupled to multiple thermal baths. The design presented here is based on a fully classical model of a nonlinear thermodynamic neuron, and requires only a single thermal bath. Our proposed design, sketched in Fig. 2, could be implemented using existing hardware elements: the neurons could be realized by RLC[12] circuits with nonlinear components, or by superconducting circuits with Josephson junctions[29]. A thermodynamic computer of this nature could be programmed to perform arbitrary nonlinear computations at specified times, powered by thermal fluctuations.

Methods

We simulated the overdamped Langevin equations described in the text using the Euler-Maruyama scheme with fixed step $\Delta t = 10^{-3}$ (times are reported in units of μ^{-1}). For reset sampling, computer outputs are read at a fixed observation time $t = t_f$ and averaged over M samples; serial sampling uses M samples, each spaced by t_f, within a single trajectory.

Our GPU workflow evaluates thousands of thermodynamic computer trajectories in parallel. For each input (or minibatch of inputs), kernels integrate all population members of the genetic algorithm and all M replicas concurrently.

Data availability

Data can be generated using the Jupyter Notebook tutorial at ref. 35. The specific data displayed in the figures is available from the authors upon reasonable request.

Code availability

Reference [35] contains a Jupyter Notebook tutorial on training the thermodynamic computers used in this paper.

References

1. Bennett, C. H. The thermodynamics of computation–a review. *Int. J. Theor. Phys.* **21**, 905–940 (1982).
2. Landauer, R. Information is physical. *Phys. Today* **44**, 23–29 (1991).
3. Ceruzzi, P. E. *A History of Modern Computing* (MIT Press, 2003).
4. Fry, R. L. Neural statics and dynamics. *Neurocomputing* **65**, 455–462 (2005).
5. Conte, T. et al. Thermodynamic computing. *arXiv preprint arXiv*:https://doi.org/10.48550/arXiv.1911.01968 (2019).
6. Hylton, T. Thermodynamic neural network. *Entropy* **22**, 256 (2020).

7. Frank, M. P. The future of computing depends on making it reversible. *IEEE Spectr.* **25**, 2017 (2017).
8. Wolpert, D. H. The stochastic thermodynamics of computation. *J. Phys. A Math. Theor.* **52**, 193001 (2019).
9. Fry, R. L. Physical intelligence and thermodynamic computing. *Entropy* **19**, 107 (2017).
10. Wimsatt, G. et al. Harnessing fluctuations in thermodynamic computing via time-reversal symmetries. *Phys. Rev. Res.* **3**, 033115 (2021).
11. Aifer, M. et al. Thermodynamic linear algebra. *npj Unconv. Comput.* **1**, 13 (2024).
12. Melanson, D. et al. Thermodynamic computing system for AI applications. *Nat. Commun.* **16**, 3757 (2025).
13. Arceri, F., Landes, F. P., Berthier, L. & Biroli, G. Glasses and aging, a statistical mechanics perspective on. in *Statistical and Nonlinear Physics* 229–296 (Springer, 2022).
14. Biroli, G. & Garrahan, J. P. Perspective: the glass transition. *J. Chem. Phys.* **138**, 12A301 (2013).
15. Hagan, M. F., Elrad, O. M. & Jack, R. L. Mechanisms of kinetic trapping in self-assembly and phase transformation. *J. Chem. Phys.* **135**, 104115 (2011).
16. Whitelam, S. & Jack, R. L. The statistical mechanics of dynamic pathways to self-assembly. *Annu. Rev. Phys. Chem.* **66**, 143–163 (2015).
17. Whitelam, S. Increasing the clock speed of a thermodynamic computer by adding noise. *npj Unconv. Comput.* **2**, 24 (2025).
18. Duffield, S., Aifer, M., Crooks, G., Ahle, T. & Coles, P. J. Thermodynamic matrix exponentials and thermodynamic parallelism. *Phys. Rev. Res.* **7**, 013147 (2025).
19. Hopfield, J. J. Neural networks and physical systems with emergent collective computational abilities. *Proc. Natl. Acad. Sci. USA* **79**, 2554–2558 (1982).
20. Hinton, G. Boltzmann machines, in *Encyclopedia of Machine Learning and Data Mining* 164–168 (Springer, 2017).
21. Salakhutdinov, R. and Hinton, G. Deep Boltzmann machines. in *Artificial Intelligence and Statistics* 448–455 (PMLR, 2009).
22. Seifert, U. Stochastic thermodynamics, fluctuation theorems and molecular machines. *Rep. Prog. Phys.* **75**, 126001 (2012).
23. Wolpert, D. H. et al. Is stochastic thermodynamics the key to understanding the energy costs of computation?. *Proc. Natl. Acad. Sci. USA* **121**, e2321112121 (2024).
24. Sagawa, T. Thermodynamic and logical reversibilities revisited. *J. Stat. Mech. Theory Exp.* **2014**, P03025 (2014).
25. Whitelam, S. Generative thermodynamic computing, *arXiv preprint arXiv* https://arxiv.org/abs/2506.15121 (2024b)
26. Cybenko, G. Approximation by superpositions of a sigmoidal function. *Math. Control Signals Syst.* **2**, 303–314 (1989).
27. Hornik, K., Stinchcombe, M. & White, H. Multilayer feedforward networks are universal approximators. *Neural Netw.* **2**, 359–366 (1989).
28. Dago, S., Pereda, J., Barros, N., Ciliberto, S. & Bellon, L. Information and thermodynamics: fast and precise approach to Landauer Os bound in an underdamped micromechanical oscillator. *Phys. Rev. Lett.* **126**, 170601 (2021).
29. Ray, K. J. & Crutchfield, J. P. Gigahertz sub-landauer momentum computing. *Phys. Rev. Appl.* **19**, 014049 (2023).
30. Dillavou, S. et al. Machine learning without a processor: emergent learning in a nonlinear analog network. *Proc. Natl. Acad. Sci. USA* **121**, e2319718121 (2024).
31. Sabattini, L. et al. Towards AI-driven autonomous growth of 2D materials based on a graphene case study. *Commun. Phys.* **8**, 180 (2024).
32. LeCun, Y., Bottou, L. éon, Bengio, Y. & Haffner, P. Gradient-based learning applied to document recognition. *Proc. IEEE* **86**, 2278–2324 (1998).
33. LeCun, Y., Cortes, C. & Burges, C. J.C. Mnist leaderboard, http://yann.lecun.com/exdb/mnist/ (1998b).
34. Lipka-Bartosik, P., Perarnau-Llobet, M. artí & Brunner, N. Thermodynamic computing via autonomous quantum thermal machines. *Sci. Adv.* **10**, eadm8792 (2024).
35. Software tutorial, https://doi.org/10.5281/zenodo.17783088 ccasert/thermodynamic-neural-network: v1.0, (2025).

Acknowledgements

S.W. perfomed work at the Molecular Foundry, supported by the Office of Science, Office of Basic Energy Sciences, of the U.S. Department of Energy under Contract No. DE-AC02-05CH11231. This research used resources of the National Energy Research Scientific Computing Center (NERSC), a U.S. Department of Energy Office of Science User Facility located at Lawrence Berkeley National Laboratory, operated under Contract No. DE-AC02-05CH11231. C.C. was supported by a Francqui Fellowship of the Belgian American Educational Foundation, and by the US DOE Office of Science Scientific User Facilities AI/ML project "A digital twin for spatiotemporally resolved experiments".

Author contributions

S.W. designed the thermodynamic neural network discussed in the text, and tested it using single-processor CPU simulations. C.C. designed and implemented the efficient parallel GPU simulations described in the text and the tutorial at ref. 35. S.W. wrote the paper with input from C.C.

Competing interests

The authors declare no competing interests.

Additional information

Supplementary information The online version contains supplementary material available at https://doi.org/10.1038/s41467-025-67958-0.

Correspondence and requests for materials should be addressed to Stephen Whitelam or Corneel Casert.

Peer review information *Nature Communications* thanks the anonymous reviewers for their contribution to the peer review of this work. A peer review file is available.

驯服非平衡热涨落 (Taming Nonequilibrium Thermal Fluctuations...)

本文档为论文《Taming Nonequilibrium Thermal Fluctuations in Subthreshold CMOS Circuits》的逐页对照翻译版。

驾驭亚阈值 CMOS 电路中的非平衡热涨落

一、 摘要

随着 CMOS 技术比例的缩小，热涨落越来越多地影响电路行为，对传统的电路设计提出了挑战。然而，在 **概率计算** 这一新兴领域，热噪声引入的固有随机性目前正在作为一种潜在的资源被探索。本工作展示了一个完全基于 CMOS 的实验平台，实现了对其内部热涨落的直接控制。这些装置起到了 **可编程的多变量高斯采样器** 的作用，为高能效的随机计算提供了一个硬件原语，并展示作为关于电子噪声和随机热力学的研究实验平台。

DOI: 10.1103/5l2z-3f1h

正文开始

【左栏】 (Left Column)

二、 正文背景与引言

CMOS 技术的激进微型化是一把双刃剑：随着晶体管电路在尺寸上的缩小，它变得更快且更节能 [1]，但也会变得噪声更大 [2]。随着器件尺寸和电源电压继续被推向其热力学极限，晶体管固有的噪声将开始扰乱传统的确定性计算机架构 [3,4]。

最近有一些提议提出，这种由噪声带来的显而易见的障碍可以通过在计算系统中构建有意设计的 **随机概率电路 (*p* 电路)** 来绕过 [5-11]。*P* 电路利用所有器件中存在的噪声来生成满足对计算有用的概率分布下的样本。

与纯粹的确定性方法相比，当运行严重依赖随机采样的特定算法时，概率计算机架构可以更具能效。随机采样在确定性计算机上是昂贵的：必须在计算机中采用包含数千个用于生成伪随机数的晶体管的复杂电路 [12]。这些大型电路耗费的能量，与那些实现类似加法这样计算内容更丰富的操作的电路消耗的能量不相上下。

【右栏】 (Right Column)

为了使 *p* 电路在计算中具实际实用价值，它必须是 **可预测的、可编程的并且是高性能的**。可预测性意味着 *p* 电路的随机动力学遵循某些可用于对其进行工程设计的简单物理模型。如果可以运行时调节它进行采样的分布，那么 *p* 电路就是具可编程性的。一个 *p* 电路的性能是由相关时间（correlation time）、能耗和物理尺寸来衡量的，这些共同量化了使用该电路进行随机采样的空间、时间和能量成本。

当前对 *p* 电路的实现，在这些关键领域至少有一项有所欠缺。利用磁隧道结构建的 *p* 电路是一个极佳的前景，具有充分描述的随机动力学模型 [13]，且易于编程 [14-16]。尽管这些器件在原则上与 CMOS 工艺兼容 [17]，但是关于集成的研究仍在进行中 [18,19]，这限制了短期的性能 [20,21]。为了避免这些集成问题，开发者也考虑过仅包含晶体管的 *p* 电路架构 [22,23]。然而，目前的方法通常依赖极其敏感的现象，诸如双稳态锁存器在加电时的随机性 [24,25]，或者是基于对噪声的粗略处理 [22]，使得编程和预测变得困难。

在深度亚阈值状态下运行的晶体管电路是构建实际 *p* 电路的自然候选者。在这些电路中，电荷传输主要是受热激活的，导向散粒噪声动力学 [26]。最近，散粒噪声模型已通过基于马尔可夫跳跃过程 (MJPs) 的技术从单晶体管水平推广到晶体管网络 [27]，表明亚阈值电路的随机动力学可以被严格预测。通过控制，亚阈值网络也易于编程... *(注：页面结束，接下页)*

页脚脚注 (Footnotes):

- * 联络作者：nfreitas@extropic.ai
- † 这些作者对本工作贡献均等
- ‡ 联络作者：trevor@extropic.ai

【左栏】 (Left Column)

此外，小型晶体管会泄露更多的电流，从而提升亚阈值电路的性能 [28]。

三、 NEAT-RN 电路架构与稳态电压控制

本文通过实验证明，使用亚阈值晶体管可以构建实用的 p **电路**。具体而言，我们介绍并表征了一类可以通过电压编程的、从多变量高斯分布中进行采样的电路。这些电路实现了在多个自由度之间控制相关性的能力，并且作为一种强大的原语（primitive），既可以单独用作为 p 电路，也可以作为在更大电路中执行非高斯采样操作的一部分（其中最具代表性且最直接的就是 p 比特 [11]）。我们的工作为利用 p 电路的近期、大规模计算机铺平了道路；我们已经将这里列出的原理应用到了一个运行类扩散模型（diffusionlike models）的概率计算系统的设计中 [29]。

除了我们的工作在概率计算方面的潜力外，通过验证文献 [27] 中提出的 MJP 模型，它也极大地推进了我们在物理层面上对亚阈值晶体管中散粒噪声（shot noise）的理解。虽然有很多研究单晶体管水平散粒噪声的工作 [26,30,31]，但在大型电路中研究噪声物理规律的工作仍然很有限，且通常是针对特定应用的 [32]。我们的工作通过实验数据，测试了一个简单且通用的亚阈值晶体管网络噪声模型，使得该模型可以在未来的工程实践中放心地使用。

本文的剩余部分将详细介绍我们的高斯采样电路，我们将其称为 **非平衡、可调温度电阻网络（NEAT-RNs）**。我们将首先介绍 NEAT-RNs，并解释（正如其名字所暗示的）如何使用电压控制来对其稳态电压分布进行编程。然后，我们将展示文献 [27] 中的 MJP 模型可以准确预测对一个简单的 2D NEAT-RN 的行为的实验测量结果。接下来，我们将表明，通过引入介导相互作用的额外自由度，可以显著增强 NEAT-RNs 的可编程性。最后，我们将讨论 NEAT-RNs 的速率和能效，并证明它们足以为现代概率计算系统的一部分提供所需的性能。

NEAT-RNs 由多个具有独立栅极控制的 CMOS 反相器组成，其中互电容耦合了不同反相器的输出。这一类中最简单的非平凡示例如 **图 1(a)** 所示。下文讨论的实验涉及到测量不同工作电压下信号 $v = (v_1, v_2)$ 的统计特性（关于时间序列的示例，请参见 **图 1(c)**）。这些信号的大部分变率可由两个噪声源来解释：(i) 与电荷通过单独晶体管传输相关的热涨落；以及 (ii) 每个晶体管整体电导率的低频涨落。虽然第一项贡献具有基础物理学本质，因为它具有…… *(接右栏)*

【右栏】 (Right Column)

……纯粹的热力学起源 [26,27]，第二项通常被认为是由材料缺陷引起的，这些缺陷起到波动电荷陷阱的作用 [33-37]。将这些获得的数据与一个能够整合两种噪声源的解析模型进行对比。然而，在接下来的内容中，我们仅将讨论局限在对 **热涨落** 的解析描述上，因为热涨落是占主导地位的，在由测量时长和采样率给定的频率范围内，它们贡献了总信号功率的约 70%（参见附录 D）。

在一个工作点附近线性化之后，NEAT-RNs 变得等效于一个含有噪声的 RC 网络 [38-40]，其中每个电阻的有效电导和有效温度都可以随意控制 [参见 **图 1(b)**]。当有效温度相等时，系统达到一个 **平衡稳态概率分布** $P(v)$，该分布完全由电容决定，而电容在纳米级电路中是无法控制的。然而，如果有效温度不同，系统将达到一个 **非平衡稳态分布**，该分布开始取决于有效温度和电导。通过这种方式，可以通过操纵电压 V^i_{dd} 和 $V^i_{\mathrm{n/p}}$ 来控制稳态分布 [参见 **图 1(f) 和 1(g)**]。

具体而言，将文献 [27] 的 MJP 形式与亚阈值晶体管的 Enz-Krummenacher-Vittoz (EKV) 模型 [41] 相结合，可以发现 NEAT-RN 的稳态涨落近似呈现高斯（Gaussian）分布：

$$P(v) \propto \exp\left(-\frac{1}{2}(v-v^*)^T\Sigma^{-1}(v-v^*)\right). \quad (1)$$

此处，v 是电路中每个节点的电压向量，v^* 是每个电压的直流（dc）电平，而 Σ 是稳态协方差矩阵。Σ 由 **李雅普诺夫方程（Lyapunov equation）** 的解给出：

$$G\Sigma C + C\Sigma G = 2k_b G^{1/2} T G^{1/2}, \quad (2)$$

其中 G 是与每个反相器关联的有效线性电导的对角矩阵，T 是有效温度的对角矩阵，而 C 是电路的麦克斯韦电容矩阵。T 和 G 的矩阵元素可以显式地用电路的控制电压来写出；参见附录 B 和 C。

在每个反相器皆处于平衡状态从而满足 $v_i^* = V_{\mathrm{dd}}/2$，且每个晶体管的亚阈值斜率参数接近 1 的极限下（参见附录 B），G 和 T 的矩阵表达式呈现为直观的形式：

$$G_{ii} = 2\frac{I_0^p}{V_T}\exp\left((V_{\mathrm{dd}}/2 - V_p^i)/V_T\right), \quad (3)$$

$$T_{ii} = T\frac{1+\exp\left(V_{\mathrm{dd}}/2V_T\right)}{2}. \quad (4)$$

此处，I_0^p 是每个晶体管的 EKV 模型电流参数。T 是系统的物理温度。

插图/图注：RN 的可预测且可编程的高斯采样。

- **(a)** 一个简单的 NEAT-RN：两个独立控制、电容耦合的 CMOS 反相器。
- **(b)** NEAT-RN 在直流（dc）工作点附近的涨落等效于一个具有可控有效电导和温度的线性 RC 电路的涨落。
- **(c)** 箭头指示的工作点处测得的电压 v_1 和 v_2 的时间序列快照。
- 对于正文中提到的沿电压扫描路径的不同点：
  - **(d)** 信号 v_1 和 v_2 的协方差矩阵的特征值长宽比（Aspect ratio α）。
  - **(e)** 该矩阵的主成分夹角（θ）。
  - 以及 **(f)** 归一化回转系数（gyration coefficient） I（积分时间 $t_I = 200$ ns）。
- **(g)** 延迟自相关（左）和互相关（右）函数的示例。
- **(h)** 两个工作点下信号 v_1 和 v_2 的中心化直方图示例。虚线表示主轴。

在所有情况下，我们固定电源电压 $V_{\mathrm{dd}}^{1} = 137 \pm 1\ \mathrm{mV}$，$V_{\mathrm{dd}}^{2} = 142 \pm 1\ \mathrm{mV}$，NMOS 栅极电压 $V_{\mathrm{n}}^{1} = V_{\mathrm{n}}^{2} = 76 \pm 1\ \mathrm{mV}$。PMOS 栅极电压满足 $V_{\mathrm{p}}^{1} + V_{\mathrm{p}}^{2} = 200 \pm 1\ \mathrm{mV}$。

**

正文文本

【左栏】 (Left Column)

……并且 $V_T = k_b T/q_e$ 为相关的热电压（q_e 为电子电荷）。我们选择利用平衡约束从该表达式中消除控制电压 V_{n}^{i}。该决定是任意的，表达式本可以同样轻易地以消除 V_{p}^{i} 的形式写出。

这种极限情况清楚地表明，**NEAT-RNs 具有极高的可编程性**：各支路的有效电导可以通过改变相对于 V_{dd} 的栅极控制电压来设定，而通过将 V_{dd} 提高到地电位以上，可以将有效温度相对于实际环境温度提高。G_{ii} 和 T_{ii} 能取得的潜在值受到**中等反型**（moderate inversion）发生的限制，一旦到达该点，用于推导方程 (2) 的散粒噪声模型假设就失效了。只要器件处于亚阈值（subthreshold）状态，就有可能独立控制 T 和 G，从而用广泛的协方差矩阵对 p 电路进行编程。

为了在经验上确立我们的 p 电路的可预测性和可编程性，我们使用先进的 **TSMC FinFET** [42-44] 工艺制造了图 1(a) 所示的电路，并将方程 (2) 拟合到其稳态电压分布上。具体而言，除了 PMOS 控制电压以外，我们固定了所有电压，并对 PMOS 控制电压进行扫描（sweep）以满足…… *(接右栏)*

【右栏】 (Right Column)

……满足 $V_{\mathrm{p}}^{1} + V_{\mathrm{p}}^{2} = 200 \pm 1\ \mathrm{mV}$。在每个工作点处测量了电压的时间序列，并据此估算出一个协方差矩阵（拟合过程的具体细节在附录 E 中概述）。

我们通过该矩阵的谱（spectrum）来表征所测量的协方差矩阵。具体而言，我们计算了特征值 λ_k 和特征向量 q_k，满足 $\Sigma q_k = \lambda_k q_k$ 且 $\lambda_0 \geq \lambda_1$。从 Σ 的特征值和特征向量出发，我们定义了特征值长宽比 α 和主成分夹角 θ：

$$\alpha \equiv \sqrt{\lambda_0/\lambda_1}, \quad \theta \equiv \arctan((q_0)_1/(q_0)_2). \quad (5)$$

观察到的稳态分布示例在图 1(h) 中展示（*注：原文写的是 1(f) 和 1(g)，应与插图结合看*）。

图 1(c) 和 1(d) 比较了 α 和 θ 对 V_{p}^{1} 的观测依赖关系与方程 (2) 的最佳拟合。这些结果表明，通过改变工作电压 $V_{\mathrm{n/p}}^{1/2}$ 可以可靠地控制信号 v_1 和 v_2 的涨落。此外，我们观察到基

于方程 (2) 的简单建模能有效地捕捉数据的主要特征。因此，产生的信号既是可控的也是可预测的。

【左栏】 (Left Column)

四、 随机动力学模型验证与环流系数

为了确立 MJP 模型能够预测 NEAT-RN 的动力学特性（而不仅仅是稳态分布），我们测量了电压状态的 **环流 (circulation)**，并将其与模型的预测进行对比。这种环流可以通过系数 $L(\delta t) \equiv \langle v \times \delta v \rangle$ 来量化，其中 $\delta v = v(t+\delta t) - v(t)$ 是时间 δt 内的位移。在稳态条件下，可以将 L 重写为：

$$L(\delta t) = \mathrm{X}_{1,2}(\delta t) - \mathrm{X}_{2,1}(\delta t), \quad (6)$$

其中 $\mathrm{X}_{j,k}(\delta t) \equiv \langle v_j(t) v_k(t+\delta t) \rangle - \langle v_j(t) \rangle \langle v_k(t+\delta t) \rangle$ 是延迟相关（delayed correlation），可以从时间序列中获取。先前的表达式被称为 **互相关不对称性**，是时间反演对称性破缺（time-reversal symmetry breaking）的一种衡量 [45-47]。例如，在大约图 1(g) 中，展示了特定工作点下归一化的延迟相关 $\chi_{j,k} \equiv \mathrm{X}_{j,k} / \sqrt{\mathrm{var}(v_j)\mathrm{var}(v_k)}$ 。观察到延迟相关确实是不对称的，这表明由于非平衡条件，时间反演不变性（time-reversal invariance）遭到了破坏。

通过分析描述 NEAT-RN 动力学的随机微分方程，可以推导出延迟相关的时间平均值的以下表达式（参见附录 F）：

$$\bar{\mathrm{X}}_{j,k} = \frac{1}{t_I} \int_0^{t_I} dt\, \mathrm{X}_{j,k}(\tau)$$

$$= \frac{1}{t_I} \left[\Sigma \left(1 - e^{-t_I G C^{-1}}\right) C G^{-1} \right]_{j,k}. \quad (7)$$

图 1(e) 展示了积分时间为 $t = 200$ ns 时的归一化 **环流系数**（原文称 circulation, 亦作 gyration） $l = (\bar{\mathrm{X}}_{1,2} - \bar{\mathrm{X}}_{2,1}) / \sqrt{\mathrm{var}(v_1)\mathrm{var}(v_2)}$ ，以及与模型最佳拟合的对比。与之前一样，这种一致性表明信号的统计特性可以得到可靠的控制和预测。

此外，这些结果表明，图 1(a) 中的装置可以被看作是使用 CMOS 电路对 **布朗回转器 (Brownian gyrator)**（一种基本的微观热机 [48]）的电子学实现。先前布朗回转器的实现主要通过加热或冷却电路来直接改变环境温度 [49]，这比我们的电子学实现要繁琐得多。

NEAT-RNs 节点拓展: 包含额外节点的 NEAT-RNs 允许比目前考虑的极小示例具有更丰富的可编程性。在这样的电路中，可以将节点分为 **可见节点 (visible nodes)** 和 **潜节点 (latent nodes)**。然后，可见节点之间的相关性可以通过它们与潜节点的共同相互作用来构建，这极其自然地扩大了可实现分布的范围。

为了在实验上确立这种增强的可编程性，我们构建了一个使用潜反相器的 **3 自由度 (3-DOF)** NEAT-RN，以覆盖更广泛的二维 (2D) 分布，如图 2(a) 所示。 *(接右栏)*

【右栏】 (Right Column)

插图/图注：RN 的可编程性。

- **(a)** 通过增加一个额外的自由度来扩展图 1(a) 中的电路。省略了每个自由节点的自电容。
- **(b)** 在控制空间探索（control space exploration）过程运行 8000 次迭代后，在 [夹角-长宽比] 平面上观察到的点，其中电源电压 $V_{\mathrm{dd}}^{1/2} \approx 5.5V_T$，$V_{\mathrm{dd}}^{0} \approx 7V_T$。
- **(c)** 应用于图 1(a) 中电路的类似协议的结果。

**

正文文本

……增加的自由度（DOF）介导了两个输出之间的耦合，从而允许对它们的相关性进行更丰富的控制。

我们通过探索控制空间中极端的协方差矩阵，研究了 NEAT-RNs 的可编程性。具体而言，在一组固定的电源电压 $V_{\mathrm{dd}}^{0/1/2}$ 条件下，我们通过一项旨在寻找具有极端长宽比（extreme aspect ratios）的配置的采样过程，生成了栅极电压 $V_{\mathrm{n/p}}^{i}$（范围在 $[0, 1.75\ \mathrm{V}]$ 之间）。结果如图 2 所示。

通过比较图 2(b) 和 2(c)，我们可以看到我们的 **3-DOF NEAT-RN 明显比 2-DOF 版本更具可编程性**。对于任何给定的 θ 值，3-DOF 电路允许将 α 控制在一个比 2-DOF 电路大得多的范围内。事实上，对于 θ 接近 $\pi/4$ 的值，2-DOF 电路的 α 几乎无法被控制，而 3-DOF 电路仍能提供完全的可编程性。

五、 稳态噪声放大与能效分析

为了使电路在概率计算机中充当高效的熵源（entropy source），它必须产生足以影响下游器件的涨落。对于利用热驱动的电子系统，这意味着噪声发生器必须……

【左栏】 (Left Column)

……产生与 V_T 相当的电压涨落。这种相互作用电压标度（interaction voltage scale）适用于广泛的一类物理现象，包括半导体和电化学反应 [50]。

然而，可实现的无源电路产生极其微弱的涨落，且在实际应用中并不高效。具体而言，在一维（1D）RC 电路中：

$$\frac{\mathrm{var}(V)^{RC}}{V_T^2} = \frac{C_T}{C}, \quad (8)$$

其中 $C_T = q_e^2/k_bT$ 是热力学电容标度，在室温下约为 6 aF（1 aF = 10^{-18} 法拉）。使用最新的晶体管工艺（如本文所用的工艺）制造的电路，其电容比这要大得多，$C \gtrsim 300$ aF。

因此，NEAT-RNs 提供的**噪声放大效果**，对于其在室温系统中的实用价值至关重要。对于运行在方程 (3) 和 (4) 平衡点处我们的 NEAT-RN 的 1D 情况而言，与无源 RC 电路相比，电压涨落的方差有所放大：

$$\mathrm{var}(V) = \frac{1 + \exp\left(V_{\mathrm{dd}}/2V_T\right)}{2}\mathrm{var}(V)^{RC} \quad (9)$$

放大因子以指数形式取决于 V_{dd}，对于 $V_{\mathrm{dd}} \approx 6V_T$，放大倍数约为 10。

由于这种放大效应是反相器固有的，且没有使用复杂的外部电路，因此它是以高效的方式实现的。具体而言，我们将每个随机样本消耗的能量定义为 $E = P\tau$，其中 τ 是输出信号的相关时间尺度（correlation timescale），而 P 是由直流电流 I^* 给定的直流功耗 $P = V_{\mathrm{dd}}I^*$。在平衡点处，τ 是：

$$\tau = \frac{C}{G}, \quad (10)$$

其中 G 由方程 (3) 给出。每个样本的能量随之呈现为：

$$E = \frac{V_{\mathrm{dd}}C^2}{q_e}\mathrm{var}(V)\tanh\left(\frac{V_{\mathrm{dd}}}{4V_T}\right), \quad (11)$$

其中 $\mathrm{var}(V)$ 如方程 (9) 所示。

方程 (9) 和 (10) 阐明了我们系统的一个极具实用价值的特性：我们的电路产生的噪声的**时间尺度和方差是独立可控的**。通过在相对于 V_{dd} 处适当操纵栅极控制电压，可以使 τ 变得任意大或任意小（在实际限度内）。相比之下，方差仅取决于电源电压。从方程 (11) 中，我

们可以看到，**每个样本消耗的能量并不取决于** τ，并且与所需的方差呈线性比例关系（在 $V_{\mathrm{dd}} \gg V_T$ 的极限下）。

【右栏】 (Right Column)

将先前拟合中发现的参数与方程 (10) 和 (11) 一起使用，可以发现 NEAT-RNs 可以作为概率计算系统中的高性能熵源。换句话说，取 $C \approx 1000\ \mathrm{aF}$，$I_0^p \approx 1\ \mathrm{nA}$，同时 $\Delta V = 5.5 V_T$，我们计算得出 $E \approx 15\ \mathrm{aJ}$。在同一场景下，当 $V_p = 0$ 时将能实现 τ 的实际最小值，此时 $\tau \approx 1\ \mathrm{ns}$。

六、 总结与致谢

总而言之，我们已经证明，利用亚阈值晶体管网络可以构建出**可预测、可编程且高性能的** p **电路**。这些亚阈值网络现在可以很容易地与其他电路进行集成，从而使用先进的晶体管工艺来构建概率计算机。我们已经在文献 [29] 中提出了这样一种架构，并希望在未来的文章中报告它的具体实现。

此外，我们的结果也激励着人们对**概率集成电路设计**进行更深入的探索。这一蓬勃发展的模拟设计子领域大部分尚未被开拓，为创造新型、实用的电路拓扑和科学发现提供了一个肥沃的土壤。这些发现可以包括基于文献 [27] 的研究而取得的其它理论进展，或者是用于验证这些理论的进一步实验工作。

致谢 (ACKNOWLEDGMENTS)

T.M. 特此感谢艾萨克·庄（Isaac Chuang）对实验设计和手稿撰写提出的宝贵建议。

数据可用性 (DATA AVAILABILITY)

支持本文研究结果的数据是公开可用的 [51]。

七、 附件细节及理论支撑

（一） 附录 A：器件的制造、控制和测量 (APPENDIX A)

本工作中进行的实验利用了一个专门设计用来详细表征包含噪声的亚阈值电路的测试芯片。我们的芯片包含具有 $[0, 0.175\ \mathrm{V}]$ 动态范围的 8 位 DAC（数模转换器），用于操纵控制电压。每个实验中的输出信号皆使用高带宽和高输入阻抗的放大器（这些放大器也在同一裸片 (die) 上实现）来进行测量。这个放大链允许将模拟信号在芯片外进行布线，以便使用 $1\text{-}\mathrm{GHz}$ 示波器进行测量。

（二） 附录 B：散粒噪声模型及其扩散极限 (APPENDIX B)

我们考虑文献 [27] 中开发的非线性电子电路的随机描述，其中电路中的每个传导器件都表现出散粒噪声。电路的状态由自由节点（即非那些……）中的净基本电荷数来描述。

【左栏】 (Left Column)

……受电压源调节的节点），由一个向量 $n \in \mathrm{N}^d$ 给出，其中 d 是自由节点的数量。成对的自由节点可以通过由整数索引 $\rho > 0$ 标识的传导器件（二极管、隧道结、晶体管等）相连接。如果一个传导器件连接在两个自由节点之间，那么基本电荷可以在它们之间双向跳跃。对于每个器件 ρ，我们为正向传导事件 $n \to n + \Delta_\rho$ 分配一个跃迁速率（transition rate） $\lambda_{+\rho}(n)$，并为反向传导事件 $n \to n + \Delta_{-\rho}$ 分配一个跃迁速率 $\lambda_{-\rho}(n)$，其中 $\Delta_\rho = -\Delta_{-\rho}$。正向方向是任意设定的，而向量 Δ_ρ 编码了对应于每次跳跃或跃迁的状态 n 的变化。

对于任何状态 n，自由节点的电压均可计算为 $v = q_e C^{-1} n + v_r$，其中 C 是自由节点的麦克斯韦电容矩阵，q_e 是基本电荷的电量，而 v_r 是取决于受调节电压的常数向量。设 $P_t(v)$ 为在时间 t 观察到电压 v 的概率。鉴于先前的描述，$P_t(v)$ 的演化遵循 **主方程 (master equation)**：

$$\partial_t P_t(v) = \sum_\rho \lambda_\rho(v - q_e C^{-1}\Delta_\rho) P_t(v - q_e C^{-1}\Delta_\rho) - \sum_\rho \lambda_\rho(v) P_t(v), \quad (B1)$$

此处为了书写方便，我们滥用了记号，将速率 $\lambda_\rho(v)$ 视为了电压 v 的函数。该马尔可夫跳跃过程的 **扩散逼近 (diffusive approximation)** 可以通过对方程 (B1) 的克拉默斯-莫亚尔展开（Kramers-Moyal expansion）进行二阶截断来获得，这对应于大电容极限 $||C|| \gg C_T$。在这种情况下，方程 (B1) 简化为福克-普朗克方程（Fokker-Planck equation），这意味着系统的动力学可以由以下形式的 **伊藤随机微分方程 (SDE)** 来近似描述：

$$C \cdot dv = \mu(v)dt + \sqrt{2K(v)} \cdot dW, \quad (B2)$$

其中 W 是独立维纳过程（Wiener processes）的向量。该逼近是无量纲控制的，且无法捕捉大的涨落 [52,53]，但在大电容极限下能妥善描述 $P_t(v)$ 的一阶矩和二阶矩 [54]。漂移向量（drift vector） $\mu(v)$ 和扩散矩阵（diffusion matrix） $K(v)$ 可以从跃迁速率 $\lambda_\rho(v)$ 中获得。相应地，与传导器件 ρ 相关的两个跃迁速率 $\lambda_{\pm\rho}(v)$ 能够通过 **热力学一致性关系** [27] 与其唯象伏安（I-V）曲线 $I_\rho(\Delta v)$ 关联起来：

$$\lambda_{+\rho}(v) - \lambda_{-\rho}(v) = I_\rho(\Delta v_\rho)/q_e, \quad (B3)$$

$$\lambda_{+\rho}(v) + \lambda_{-\rho}(v) = \coth\left(\Delta v_\rho / 2V_T\right) I_\rho(\Delta v_\rho)/q_e.$$

【右栏】 (Right Column)

利用方程 (B3)，可以获得漂移向量 $\mu(v)$ 和扩散矩阵 $K(v)$ 的以下表达式：

$$\mu(v) \equiv \sum_\rho I_\rho(\Delta v_\rho)\Delta_\rho,$$

$$K(v) \equiv \frac{q_e}{2}\sum_\rho I_\rho(\Delta v_\rho)\coth\left(\Delta v_\rho/2V_T\right)\Delta_\rho \cdot \Delta_\rho^T, \quad (B4)$$

其中 Δv_ρ 是器件 ρ 在状态 v 下的电压降。

对于具有确定性固定点吸引子 v^* 的电路，即满足 $\mu(v^*) = 0$ 的电路，方程 (B2) 中的随机动力学可以被 **线性化** 为：

$$C \cdot dv = -G \cdot (v - v^*)dt + \sqrt{2k_b G\mathrm{T}} \cdot dW, \quad (B5)$$

其中我们定义了有效电导矩阵 G（元素为 $G_{jk} \equiv -\partial_{v_k}\mu_j(v^*)$）以及有效温度矩阵 $\mathrm{T} \equiv G^{-1}K(v^*)/k_b$。上述动力学的稳态分布由正文中的方程 (1) 和 (2) 给出。

最后，我们注意到对于一维情形，方程 (B5) 的线性化动力学具有以下 **稳态自相关函数**：

$$\mathrm{X}(\delta t) = \frac{k_b\mathrm{T}}{C}e^{-(G/C)\,|\,\delta t\,|}, \quad (B6)$$

这导向了以下 **洛伦兹（Lorentzian）单边功率谱密度（PSD）**：

$$P(f) = \frac{P_0}{1 + (f/f_0)^2}, \quad (B7)$$

其中 $P_0 = 4k_b\mathrm{T}/G$，同时 $f_0 = G/(2\pi C)$。

（三） 附录 C：基于 EKV 的反相器模型 (APPENDIX C)

我们现在考虑一个单独的反相器 [如图 1(a) 所示的左侧或右侧一对晶体管]。根据包含漏极引发势垒降低（DIBL）效应的 EKV 模型的扩展（如文献 [55] 所示），流过 NMOS 晶体管

的电流由以下公式给出：

$$I_n = I_0^n \log^2\left(1 + e^{(V_{gb}-V_{th}^n)/2n_n} e^{-V_{sb}/2} e^{\gamma_n V_{ds}/2}\right) - I_0^n \log^2\left(1 + e^{(V_{gb}-V_{th}^n)/2n_n} e^{-V_{db}/2} e^{-\gamma_n V_{ds}/2}\right),$$

其中 I_0^n、V_{th}^n、n_n 和 γ_n 是模型参数，在此电压 $V_{gb} = V_n$、$V_{sb} = 0$、$V_{db} = V_{ds} = v$ 均以热电压 V_T 为单位进行表示。相同的表达式也给出了流过 PMOS 晶体管的电流 I_p，这次是对应参数 I_0^p、V_{th}^p、n_p 以及 γ_p，只需将 $I_p \to -I_n$ 进行替换，并使用电压 $V_{gb} = -(V_p - V_{\mathrm{dd}})$、$V_{sb} = 0$、$V_{db} = V_{ds} = -(v - V_{\mathrm{dd}})$。

【左栏】 (Left Column)

为了在解析上取得进展，采用若干近似是有用的。尤其是，我们考虑满足 $e^{(V_{gb}-V_T)/2n_{n/p}} \ll 1$ 的亚阈值状态，并忽略 DIBL 效应（即设定 $\gamma_n = \gamma_p = 0$）。那么，电流 I_n 和 I_p 就化简为以下关于输出节点电压 v 的函数：

$$I_p(v) = \underbrace{I_0^p e^{-(V_p - V_{\mathrm{dd}})/n_p}}_{c_p}\left(1 - e^{v - V_{\mathrm{dd}}}\right),$$

$$I_n(v) = \underbrace{I_0^n e^{V_n/n_n}}_{c_n}\left(1 - e^{-v}\right), \quad (C2)$$

其中我们现在将因子 $e^{-V_{th}^{n/p}/n_{n/p}}$ 整合到了各自的常数 $I_0^{n/p}$ 之中。确定性输出电压 v^* 满足 $I_p(v^*) = I_n(v^*)$，在上述近似下，可以导出表达式：

$$e^{v^*} = \frac{e^{V_{\mathrm{dd}}}}{2}\left[\left(1 - \frac{c_n}{c_p}\right) + \sqrt{\left(1 - \frac{c_n}{c_p}\right)^2 + 4\frac{c_n}{c_p}e^{-V_{\mathrm{dd}}}}\right]. \quad (C3)$$

使用该公式，我们得出 **有效电导** 由以下公式给出：

$$G = V_T^{-1}\sqrt{(c_p - c_n)^2 + 4c_p c_n e^{-V_{\mathrm{dd}}}}. \quad (C4)$$

此外，**有效温度** 由以下公式给出：

$$k_b\mathrm{T} = \frac{q_e I^*}{2G}\left[\coth((V_{\mathrm{dd}} - v^*)/2) + \coth(v^*/2)\right], \quad (C5)$$

其中 $I^* \equiv (c_p + c_n - V_T G)/2$ 为稳态电流。当 $c_n = c_p$ 时，即可达到正文中考虑的平衡条件。正文中的表达式还假设所有晶体管的亚阈值斜率（subthreshold slopes）均为 1（即对所有反相器有 $n_{n/p} = 1$）。

（四） 附录 D：频谱分析 (APPENDIX D)

图 3(a) 展示了在不同工作电压下，从时间序列中数值计算得到的信号 v_1 的功率谱密度（PSD）。每个 PSD 上方的黑色虚线展示了使用以下模型对其进行拟合的结果：

$$P(f) = \frac{P_0}{1 + (f/f_0)^2} + \frac{L}{f^\alpha} + B. \quad (D1)$$

第一项对应于 **洛伦兹光谱**，这在之前的小节中已经由理论作出了预期。第二项旨在捕捉低频下占主导地位的 **粉红噪声（pink noise）**，而最后一项则考虑了可能与外部噪声源（例如放大级）相关的平坦频谱贡献。 *(接右栏)*

【右栏】 (Right Column)

**插图/图注：--

正文文本

这种分解允许将信号的总功率或方差拆分成不同的贡献项，如图 3(b) 所示。

最后，我们注意到，可以通过参数 P_0 和 f_0 计算出**有效温度**为 $k_b\mathrm{T} = Cf_0P_0\pi/2$，其中 C 是所讨论反相器的总输出电容 [例如，对于左侧反相器，若用自电容 $C_{1/2}$ 和互电容 C_m 表示，则为 $C = C_1 + 1/(1/C_2 + 1/C_m)$]。

**

（五） 附录 E：数据分析与模型拟合 (APPENDIX E)

将实验数据与理论模型进行对比分为 **三个阶段**：

1. 确定每个单独反相器的固有参数。
2. 对 $1/f$ 噪声源进行有效建模。
3. 基于观察到的相关性确定全局电容矩阵。 原始时间序列和用于分析的代码可以在文献 [51] 中找到。

在**第一阶段**，对于每个反相器，我们基于方程 (B4)、(B5) 和 (C1) 同时拟合平均输出电压 $\langle v \rangle$、频率 f_0 以及有效温度 $k_b \mathrm{T}$ 。结果在接下来的内容（通常是图 4）中展示。图板（Panels）(a) 和 (b) 显示，基于方程 (C1) 的模型能够很好地捕捉系统的动力学，而图板 (c) 则是……

【左栏】 (Left Column)

**插图/图注：--

正文文本

……图 4(c) 的结果表明，导致方程 (B4) 中 $K(v)$ 的 **散粒噪声建模假设**（shot-noise modeling assumption）能够很好地描述所采用工作电压下的 **固有热涨落**。

在**第二阶段**，我们的目标是描述 **低频粉红噪声（pink-noise）方差** 的变异性 [见图 3(b)]，它是信号总方差中的第二大贡献。MOS 晶体管中的低频噪声通常被建模为门极氧化物中存在的涨落电荷陷阱引起的 **阈值电压 V_{th} 的随机涨落**，这些陷阱共同产生了一个类似于 $1/f$ 的频谱 [33–37]。基于方程 (C1) 对每个反相器的直流（dc）模型进行 **小信号分析**，提供了一种在理解 V_{th} 涨落如何映射到测量输出方面的简单方法。为此，我们只需要考虑增益 $g_{n/p} = \mid \partial v^* / \partial V_{th}^{n/p} \mid$，它指示了确定性输出电压 v^* 随两种阈值电压各自的微弱扰动如何变化。利用在前一阶段拟合的参数，可以很容易地从模型中计算出这些增益 [见图 5(a)]。接着，如果在对应于总观察窗口和采样率的频率范围内，阈值电压 $V_{th}^{n/p}$ 的涨落总功率为 $S_{n/p}$，那么…… *(接右栏)*

**

【右栏】 (Right Column)

**插图/图注：--

正文文本

……同一频率范围内输出信号的低频涨落则由以下公式给出：

$$S_{1/f} = g_n^2 S_n + g_p^2 S_p + S_0, \quad (E1)$$

其中 S_0 计入了 **外部低频噪声源**，且假设所涉及的三个噪声源相互独立。图 5 比较了作为工作点函数的由低频噪声引起的总方差，以及使用方程 (E1) 模型的拟合结果。我们看到，尽管该方法十分简单，但却可以解释大部分的变异性。

在**最后一个阶段**，我们将通过求解正文中的方程 (2) 获得的协方差矩阵，与在不同工作点下实验观察到的协方差矩阵进行比较，从而得以 **估计反相器输出的自电容和互电容**。

具体操作如下：我们使用在第一阶段获得的模型参数，计算每个工作点下分属每个反相器的电导 G 和有效温度 T 。然后，给定一张由建议的 C_1、 C_2 和 C_m 值构建的电容矩阵 C，我们求解方程 (2) 中的 **李雅普诺夫方程**，以获得预期的协方差矩阵 Σ。该协方差矩阵将与从实验数据估计出的协方差矩阵进行对比。实验估计协方差矩阵的对角元素为方差的洛伦兹分量，观察到的相关性 $\mathrm{X}_{1,2}(\delta t = 0)$ 则为……

**

【左栏】 (Left Column)

**插图/图注：--

正文文本

……（实验估计协方差矩阵的非对角元素则是）观察到的相关性 $\mathrm{X}_{1,2}(\delta t = 0)$。该过程的结果如图 6 所示。

最后，正文中的图 1(d) 和 1(e) 展示了原始时间序列（即包含所有噪声贡献）的协方差矩阵的长宽比（aspect ratio）和夹角（angle）。相同图表中的虚线是通过考虑协方差矩阵 $\Sigma_T = \Sigma_\mathrm{L} + \Sigma_{1/f}$ 从拟合模型中计算得出的，其中 Σ_L 是通过求解方程 (2) 中的李雅普诺夫方程获得的，而 $\Sigma_{1/f}$ 是一个对角矩阵，其元素 $S_{1/f,1}$ 和 $S_{1/f,2}$ 则根据方程 (E1) 计算得出。

**

（六） 附录 F：环流系数 (APPENDIX F: GYRATION COEFFICIENT)

我们现在简述用于延迟相关的方程 (7) 的推导过程。我们首先注意到，在稳态条件下，延迟相关 $\mathrm{X}_{j,k}(\delta t)$ 可以写为：

$$\mathrm{X}_{j,k}(\delta t) = \int dv \int dv' (v_k' - v_k^*)(v_j - v_j^*) P(v', t+\delta t \mid v, t) P(v)$$

$$= \int dv (v_j - v_j^*) \left[e^{-\delta t C^{-1} G} \cdot (v - v^*) \right]_k P(v)$$

$$= [e^{-\delta t C^{-1} G} \Sigma]_{k,j} = [\Sigma\, e^{-\delta t G C^{-1}}]_{j,k}, \quad (F1)$$

其中我们利用了如下事实：对于方程 (B5) 中的线性过程，条件概率 $P(v', t+\delta t \mid v, t)$ 是一个具有以指数形式弛豫的平均值 $\langle v' \rangle = v^* + e^{-\delta t C^{-1} G} \cdot (v - v^*)$ 的高斯分布，并且稳态…… *(接右栏)*

【右栏】 (Right Column)

……并且稳态分布 $P(v)$ 由方程 (1) 给出。

只要对任意可逆矩阵 A 使用积分公式 $\int_0^{t_I} dt e^{-tA} = A^{-1}(1 - e^{-t_I A})$（此处 t 或为积分延迟变量），即可推导出方程 (7)。

八、 参考文献

(注：为保证准确，保留原作者及期刊名，括号内翻译论文标题)

- **[1]** R. Dennard, F. Gaensslen, H.-N. Yu, V. Rideout, E. Bassous, and A. LeBlanc, **Design of ion-implanted MOSFET's with very small physical dimensions** (具有极小物理尺寸的离子注入 MOSFET 的设计), IEEE J. Solid-State Circuits **9**, 256 (1974).
- **[2]** H. Nyquist, **Thermal agitation of electric charge in conductors** (导体中电荷的热搅动), Phys. Rev. **32**, 110 (1928).
- **[3]** L. B. Kish, **End of Moore's law: Thermal (noise) death of integration in micro and nano electronics** (摩尔定律的终结：微电子与纳米电子集成的热（噪声）散逸/死亡), Phys. Lett. A **305**, 144 (2002).
- **[4]** E. Rezaei, M. Donato, W. R. Patterson, A. Zaslavsky, and R. I. Bahar, **Fundamental thermal limits on data retention in low-voltage CMOS latches and SRAM** (低压 CMOS 锁存器和 SRAM 数据保持的根本热力学极限), IEEE Trans. Device Mater. Rel. **20**, 488 (2020).
- **[5]** B. R. Zink, Y. Lv, and J.-P. Wang, **Review of magnetic tunnel junctions for stochastic computing** (用于随机计算的磁性隧道结综述), IEEE J. Explor. Solid-State Comput. Devices Circuits **8**, 173 (2022).
- **[6]** S. Chowdhury, A. Grimaldi, N. A. Aadit, S. Niazi, M. Mohseni, S. Kanai, H. Ohno, S. Fukami, L. Theogarajan, G. Finocchio *et al.*, **A full-stack view of probabilistic computing with p-bits: Devices, architectures, and algorithms** (利用 p-bit 进行概率计算的全栈视角：器件、架构与算法), IEEE J. Explor. Solid-State Comput. Devices Circuits **9**, 1 (2023).
- **[7]** J. Kim, J.-K. Han, H.-Y. Maeng, J. Han, J. W. Jeon, Y. H. Jang, K. S. Woo, Y.-K. Choi, and C. S. Hwang, **Fully CMOS-based p-bits with a bistable resistor for**

probabilistic computing (利用双稳态电阻实现的全 CMOS 概率计算 p-bit), Adv. Funct. Mater. **34**, 2307935 (2024).

- **[8]** I. Ahmed, P.-W. Chiu, W. Moy, and C. H. Kim, **A probabilistic compute fabric based on coupled ring oscillators for solving combinatorial optimization problems** (基于耦合环形振荡器的用于解决组合优化问题的概率计算构架), IEEE J. Solid-State Circuits **56**, 2870 (2021).
- **[9]** W. Lee, H. Kim, H. Jung, Y. Choi, J. Jeon, and C. Kim, **Correlation free large-scale probabilistic computing using a true-random chaotic oscillator p-bit** (使用真随机混沌振荡器 p-bit 的无相关大规模概率计算), Sci. Rep. **15**, 1 (2025).
- **[10]** J. Kim, S. S. Woo, and R. Sarpeshkar, **Fast and precise emulation of stochastic biochemical reaction networks with amplified thermal noise in silicon chips** (在硅芯片上利用放大的热噪声对随机生化反应网络进行快速而精确的仿真), IEEE Trans. Biomed. Circuits Syst. **12**, 379 (2018).
- **[11]** W. A. Borders, A. Z. Pervaiz, S. Fukami, K. Y. Camsari, H. Ohno, and S. Datta, **Integer factorization using stochastic magnetic tunnel junctions** (利用随机磁性隧道结实现整数因子分解), Nature **573**, 390 (2019).
- **[12]** N. S. Singh, K. Kobayashi, Q. Cao, K. Selcuk, T. Hu, S. Niazi, N. A. Aadit, S. Kanai, H. Ohno, S. Fukami *et al.*, **CMOS plus stochastic nanomagnets enabling heterogeneous computers for probabilistic inference and learning** (CMOS 结合随机纳米磁体使异构计算机能够进行概率推理和学习), Nat. Commun. **15**, 2685 (2024).
- **[13]** R. Faria, K. Y. Camsari, and S. Datta, **Low-barrier nanomagnets as p-bits for spin logic** (低势垒纳米磁体作为自旋逻辑的 p-bit), IEEE Magn. Lett. **8**, 1 (2017).
- **[14]** K. Y. Camsari, R. Faria, B. M. Sutton, and S. Datta, **Stochastic p-bits for invertible logic** (用于可逆逻辑的随机 p-bit), Phys. Rev. X **7**, 031014 (2017).
- **[15]** K. Y. Camsari, S. Salahuddin, and S. Datta, **Implementing p-bits with embedded MTJ** (利用嵌入式 MTJ 实现 p-bit), IEEE Electron. Device Lett. **38**, 1767 (2017).

(注：括号内为论文标题的中文参考翻译)

- **[16]** Y. Shao, C. Duffee, E. Raimondo, N. Davila, V. Lopez-Dominguez, J. A. Katine, G. Finocchio, and P. K. Amiri, **Probabilistic computing with voltage-controlled dynamics in magnetic tunnel junctions** (磁性隧道结中利用电压控制动力学进行概率计算), Nanotechnology **34**, 495203 (2023).
- **[17]** D. Vodenicarevic, N. Locatelli, A. Mizrahi, J. S. Friedman, A. F. Vincent, M. Romera, A. Fukushima, K. Yakushiji, H. Kubota, S. Yuasa *et al.*, **Low-energy truly random number generation with superparamagnetic tunnel junctions for unconventional computing** (利用超顺磁性隧道结为非传统计算生成低能耗真随机数), Phys. Rev. Appl. **8**, 054045 (2017).
- **[18]** K. Yang, Q. Dong, Z. Wang, Y.-C. Shih, Y.-D. Chih, J. Chang, D. Blaauw, and D. Sylvester, in *2018 IEEE Symposium on VLSI Circuits* (IEEE, Honolulu, HI, USA, 2018), pp. 171–172.

- **[19]** D. Edelstein, M. Rizzolo, D. Sil, A. Dutta, J. DeBrosse, M. Wordeman, A. Arceo, I. Chu, J. Demarest, E. R. Edwards *et al.*, in *2020 IEEE International Electron Devices Meeting (IEDM)* (IEEE, San Francisco, CA, USA, 2020), pp. 11.5.1–11.5.4.
- **[20]** J. Daniel, Z. Sun, X. Zhang, Y. Tan, N. Dilley, Z. Chen, and J. Appenzeller, **Experimental demonstration of an on-chip p-bit core based on stochastic magnetic tunnel junctions and 2D MoS2 transistors** (基于随机磁性隧道结和二维 MoS2 晶体管的片上 p-bit 核心的实验展示), Nat. Commun. **15**, 4098 (2024).
- **[21]** J. Kaiser, W. A. Borders, K. Y. Camsari, S. Fukami, H. Ohno, and S. Datta, **Hardware-aware in situ learning based on stochastic magnetic tunnel junctions** (基于随机磁性隧道结的硬件感知原位学习), Phys. Rev. Appl. **17**, 014016 (2022).
- **[22]** P. Korkmaz, B. E. Akgul, K. V. Palem, and L. N. Chakrapani, **Advocating noise as an agent for ultra-low energy computing: Probabilistic complementary metal-oxide-semiconductor devices and their characteristics** (提倡噪声作为超低能耗计算媒介：概率互补金属氧化物半导体器件及其特性), Jpn. J. Appl. Phys. **45**, 3307 (2006).
- **[23]** K. Palem and A. Lingamneni, **Ten years of building broken chips: The physics and engineering of inexact computing** (打造“残缺”芯片的十年：不精确计算的物理学与工程学), ACM Trans. Embed. Comput. Syst. (TECS) **12**, 1 (2013).
- **[24]** J. Holleman, S. Bridges, B. P. Otis, and C. Diorio, **3 μW CMOS true random number generator with adaptive floating-gate offset cancellation** (带有自适应浮栅失调消除功能的 3 微瓦 CMOS 真随机数发生器), IEEE J. Solid-State Circuits **43**, 1324 (2008).
- **[25]** J. Bae, J. Koo, C. Shim, and B. Kim, in *2024 IEEE International Solid-State Circuits Conference (ISSCC)* (IEEE, San Francisco, CA, USA, 2024), Vol. 67, pp. 284–286.
- **[26]** R. Sarpeshkar, T. Delbruck, and C. A. Mead, **White noise in MOS transistors and resistors** (MOS 晶体管和电阻器中的白噪声), IEEE Circuits Devices Mag. **9**, 23 (1993).
- **[27]** N. Freitas, J.-C. Delvenne, and M. Esposito, **Stochastic thermodynamics of nonlinear electronic circuits: A realistic framework for computing around kT** (非线性电子电路的随机热力学：一个用于围绕 kT 进行计算的现实框架), Phys. Rev. X **11**, 031064 (2021).
- **[28]** E. Morifuji, T. Yoshida, M. Kanda, S. Matsuda, S. Yamada, and F. Matsuoka, **Supply and threshold-voltage trends for scaled logic and SRAM MOSFETs** (按比例缩小的逻辑和 SRAM MOSFET 的电源和阈值电压趋势), IEEE Trans. Electron. Devices **53**, 1427 (2006).
- **[29]** A. Jelinčič, O. Lockwood, A. Garlapati, G. Verdon, and T. Mccourt, **An efficient probabilistic hardware architecture for diffusion-like models** (用于扩散类模型的高效概率硬件架构), arXiv arXiv:2510.23972, Submitted to npj Unconventional Computing.

- **[30]** G. Reimbold and P. Gentil, **White noise of MOS transistors operating in weak inversion** (在弱反型区工作的 MOS 晶体管的白噪声), IEEE Trans. Electron Devices **29**, 1722 (1982).
- **[31]** S. Tedja, H. H. Williams, J. Van der Spiegel, F. M. Newcomer, and R. Van Berg, **Noise spectral density measurements of a radiation hardened CMOS process in the weak and moderate inversion** (在弱反型和中等反型区抗辐射 CMOS 工艺的噪声谱密度测量), IEEE Trans. Nucl. Sci. **39**, 804 (1992).
- **[32]** H. Tian, B. A. Fowler, and A. El Gamal, in *Sensors, Cameras, and Systems for Scientific/Industrial Applications* (SPIE, San Jose, CA, United States, 1999), Vol. 3649, pp. 177–185.
- **[33]** A. G. Mahmutoglu, A. Demir, and J. Roychowdhury, in *2013 IEEE/ACM International Conference on Computer-Aided Design (ICCAD)* (IEEE, San Jose, CA, United States, 2013), pp. 500–507.
- **[34]** B. Stampfer, A. Grill, and M. Waltl, in *Noise in Nanoscale Semiconductor Devices* (Springer, 2020), pp. 229–257.
- **[35]** H. Tian and A. El Gamal, **Analysis of $1/f$ noise in switched MOSFET circuits** (开关 MOSFET 电路中 1/f 噪声的分析), IEEE Trans. Circuits Syst. II: Analog Digit. Signal Process. **48**, 151 (2001).
- **[36]** C. Jakobson, I. Bloom, and Y. Nemirovsky, $1/f$ **noise in CMOS transistors for analog applications from subthreshold to saturation** (用于模拟应用的 CMOS 晶体管中从亚阈值到饱和区的 1/f 噪声), Solid State Electron. **42**, 1807 (1998).
- **[37]** M. Kirton and M. Uren, **Noise in solid-state microstructures: A new perspective on individual defects, interface states and low-frequency ($1/f$) noise** (固态微结构中的噪声：关于单个缺陷、界面态和低频 (1/f) 噪声的新视角), Adv. Phys. **38**, 367 (1989).
- **[38]** S. Ciliberto, A. Imparato, A. Naert, and M. Tanase, **Statistical properties of the energy exchanged between two heat baths coupled by thermal fluctuations** (通过热涨落耦合的两个热库之间热交换的统计特性), J. Stat. Mech. **2013**, P12014 (2013).
- **[39]** M. Baiesi, S. Ciliberto, G. Falasco, and C. Yolcu, **Thermal response of nonequilibrium RC circuits** (非平衡 RC 电路的温度/热响应), Phys. Rev. E **94**, 022144 (2016).
- **[40]** N. Freitas, J.-C. Delvenne, and M. Esposito, **Stochastic and quantum thermodynamics of driven RLC networks** (受驱 RLC 网络的随机与量子热力学), Phys. Rev. X **10**, 031005 (2020).
- **[41]** C. C. Enz and E. A. Vittoz, *Charge-Based MOS Transistor Modeling* (基于电荷的 MOS 晶体管建模) (John Wiley & Sons, Ltd, 2006).
- **[42]** T. Sekigawa and Y. Hayashi, **Calculated threshold-voltage characteristics of an XMOS transistor having an additional bottom gate** (带有额外底栅的 XMOS 晶体管的计算阈值电压特性), Solid-State Electron. **27**, 827 (1984).

- **[43]** S.-Y. Wu, C.-H. Chang, M. Chiang, C. Lin, J. Liaw, J. Cheng, J. Yeh, H. Chen, S. Chang, K. Lai *et al.*, in *2022 International Electron Devices Meeting (IEDM)* (IEEE, San Francisco, CA, USA, 2022) pp. 27.5.1–27.5.4.
- **[44]** J. Liu, S. Mukhopadhyay, A. Kundu, S. Chen, H. Wang, D. Huang, J. Lee, M. Wang, R. Lu, S. Lin, Y. Chen, H. Shang, P. Wang, H. Lin, G. Yeap, and J. He, in *2020 IEEE International Electron Devices Meeting (IEDM)* (IEEE, San Francisco, CA, USA, 2020), pp. 9.2.1–9.2.4.
- **[45]** N. Ohga, S. Ito, and A. Kolchinsky, **Thermodynamic bound on the asymmetry of cross-correlations** (互相关不对称性的热力学界限), Phys. Rev. Lett. **131**, 077101 (2023).
- **[46]** S. Liang and S. Pigolotti, **Thermodynamic bounds on time-reversal asymmetry** (时间反演不对称性的热力学界限), Phys. Rev. E **108**, L062101 (2023).
- **[47]** J. Gu, **Thermodynamic bounds on the asymmetry of cross-correlations with dynamical activity and entropy production** (带有动力学活性和熵产生的互相关不对称性的热力学界限), Phys. Rev. E **109**, L042101 (2024).

(注：括号内为论文标题的中文参考翻译)

- **[48]** R. Filliger and P. Reimann, **Brownian gyrator: A minimal heat engine on the nanoscale** (布朗回转器：纳米级的极小热机), Phys. Rev. Lett. **99**, 230602 (2007).
- **[49]** K.-H. Chiang, C.-L. Lee, P.-Y. Lai, and Y.-F. Chen, **Electrical autonomous Brownian gyrator** (电控自主布朗回转器), Phys. Rev. E **96**, 032123 (2017).
- **[50]** S. Arrhenius, **Über die Dissociationswärme und den Einfluss der Temperatur auf den Dissociationsgrad der Elektrolyte** (关于解离热以及温度对电解质解离度的影响), Z. Phys. Chem. **4**, 96 (1889).
- **[51]** Extropic Corp., Dataset for **“Taming non-equilibrium thermal fluctuations in subthreshold CMOS circuits”** (数据集：“在亚阈值 CMOS 电路中驯服非平衡热涨落”), Zenodo (2026), https://doi.org/10.5281/zenodo.18636981
- **[52]** P. Hanggi, H. Grabert, P. Talkner, and H. Thomas, **Bistable systems: Master equation versus Fokker-Planck modeling** (双稳态系统：主方程与福克-普朗克建模的对比), Phys. Rev. A **29**, 371 (1984).
- **[53]** D. Roberts, T. McCourt, G. Massarelli, J. Rothschild, and N. Freitas, **Improved diffusive approximation of Markov jump processes close to equilibrium** (接近平衡状态的马尔可夫跳跃过程的改进扩散逼近), Phys. Rev. Res. **8**, 013161 (2026).
- **[54]** A. Gopal, M. Esposito, and N. Freitas, **Large deviations theory for noisy nonlinear electronics: CMOS inverter as a case study** (噪声非线性电子学的大偏差理论：以 CMOS 反相器为例), Phys. Rev. B **106**, 155303 (2022).
- **[55]** A. Low and P. Hasler, in *42nd Midwest Symposium on Circuits and Systems (Cat. No. 99CH36356)* (第 42 届中西部电路与系统学术研讨会) (IEEE, Las Cruces, NM, USA, 1999), Vol. 1, pp. 141–144.